5-2017

Investigations of Shallow Flows and Laboratory Raindrop Morphodynamics

Md Nasimul Hoque Chowdhury
Clemson University, chowdhu@g.clemson.edu

INVESTIGATIONS OF SHALLOW FLOWS AND LABORATORY RAINDROP MORPHODYNAMICS

A Dissertation
Presented to
the Graduate School of
Clemson University

In Partial Fulfillment
of the Requirements for the Degree
Doctor of Philosophy
Civil Engineering

by
Md Nasimul Hoque Chowdhury
May 2017

Accepted by:
Dr. Abdul A. Khan, Committee Chair
Dr. Nadarajah Ravichandran
Dr. Ashok Mishra
Dr. Kalyan Piratla

ABSTRACT

Shallow flows are one of the most intrigued and complicated to understand in the field of hydraulics. In this research, three separate researches (turbulent jets in shallow flows, rain drop laboratory simulations, and characterization of shallow flows) concentrating on shallow turbulent flows were investigated.

Knowledge of turbulent jets in shallow water depths is of utmost importance to adequately characterize the municipal and industrial discharges. Propagation and dilution of such discharges are influenced by the presence of channel bed and water surface at close proximity. In this study, the bed/water surface confinement effects on circular turbulent jets were numerically investigated by analyzing the key parameters such as decay of maximum velocity, velocity profiles, growth of jet, locus of maximum velocity, and turbulent properties. Results reveal that the confinement has profound impact on the entrainment and mixing characteristics of a jet. Entrainment is suppressed at the confining surface and as a consequence velocity decays at a lower rate. The locus of maximum velocity shifts toward the closest confining surface for asymmetrical cases, while it shifts toward the bed for symmetrical cases. Mixing of a jet both in the horizontal and the vertical planes are affected significantly by the confinement. Turbulence characteristics differ significantly in the vertical plane only. Findings from this study will be useful for characterizing properties of circular jets discharging in a confined ambient conditions.

Motivated by various meteorological and hydrological applications, this research investigates the free fall of water drops to provide guidance in laboratory simulations of natural rainfall and to elucidate drop morphodynamics. Drop fall velocity and shape

parameters such as axis ratio (ratio of the maximum vertical and horizontal chords of the drop), chord ratio (ratio of the shortest chord and longest chord of the drop), orientation angle (angle between the longest chord of the drop and the horizontal axis), and relative fluctuation of chords (difference between vertical and horizontal chord fluctuations) were investigated for three selected water drop sizes (2.6, 3.7, and 5.1 mm spherical volume equivalent diameter) using high speed imaging. Based upon experimental observations, three distinct fall zones were identified: Zone I, in which source induced oscillations and shape adjustment take place; Zone II, in which equilibrium-shaped drops accelerate to achieve terminal velocity; and Zone III, in which equilibrium-shaped drops fall at terminal velocity. Our results revealed that the fall distance values of approximately 6 m and 12 m can be used as conservative reference values for rainfall experiments with oscillation-free fall of drops (i.e. end of Zone I and onset of Zone II) and with equilibrium-shaped drops falling at terminal velocities (i.e. end of Zone II and onset of Zone III), respectively, for the entire raindrop size spectrum in natural rainfall. These required fall distance values are smaller than the distances discussed in the literature. Methodology and results presented here will facilitate optimum experimental laboratory simulations of natural rainfall.

The hydraulic characteristics of the very shallow flows in a coarse grain bed, such as velocity profiles, near bed velocity profile, bed shear stress, resistance coefficients, were investigated using numerical simulations. Characteristics such as velocity profiles, near bed velocity profile, bed shear stress, resistance coefficients were analyzed. Two different approaches are used to represent grains on the bed. The first approach uses undular bed

depicting grains topography with surface roughness $\left(k_{su}\right)$. In the second approach, the bed is considered flat with equivalent sand roughness height $\left(k_s\right)$ representing the total roughness effects. Results reveal that the undular bed model performs better than the flat bed model in representing the velocity profile, turbulence characteristics, shear stress, and uniform flow depth. Two flow regions are identified from the undular bed simulations. Bed shear stresses are represented more accurately using the turbulent shear stress profiles. Resistance coefficients (friction factor or Manning's roughness coefficient) varies with Froude number and submergence ratio (depth divided by roughness height). In addition, undular bed contribution to the total flow resistance increases with decrease in flow depth.

DEDICATION

To my beloved parents and my family for whom my whole life pertains.

ACKNOWLEDGMENTS

To enlist the entire number of persons to whom I am in debt for, might not be possible. Therefore, in a few words I would like to say thank you to those who have made a mark on me and this research in particular.

Without the support and encouragement of my family, and in particular my parents Md Azimul Hoque Chowdhury and Ayesha Akhter Chowdhury, this work would not have been possible. My beloved siblings have always been my motivation to push forward. I also would like to mention my friends back in Bangladesh, United States, and Clemson, without whom, this journey would have been difficult.

I would like to formally acknowledge the support, guidance, and direction that I have received from my committee chair, Dr. Abdul Khan. His insight and consultation have guided me to face the challenges throughout my graduate student life.

I would like to acknowledge Dr. Firat Testik, for his guidance and support in the rain drop research section of this dissertation. I would also like to acknowledge my committee members, Dr. Nadarajah Ravichandran, Dr. Ashok Mishra, and Dr. Kalyan Piratla for the support and time in reviewing the dissertation.

Lastly, I would like to conclude by acknowledging the South Carolina Department of Transportation and the Clemson University for their financial support during the entire research period.

TABLE OF CONTENTS

Page

LIST OF TABLES

Table Page

LIST OF FIGURES

Figure Page

CHAPTER 1

INTRODUCTION

Effluent discharge in shallow water depth and sheet flows represent extreme scenarios of open channel flow. As, water surface and channel bed are in close proximity, the combined effects of the water surface and bed make the shallow water depth and sheet flows more interesting as well as more complicated.

Industrial and municipal waste discharges into shallow ambient water are in the form of turbulent jets. Jets are produced as high velocity fluid is discharged into a stationary or dynamic ambient fluid. Knowledge of dilution, mixing, and spreading of these discharges is essential considering the environmental significance associated with it. Concentration of the effluent being discharged needs to be diluted within specific distance downstream from the source. Dilution is dependent upon the fluid properties, flow properties, discharging source geometry, and the environment and geometry of the ambient fluid. Existing dilution estimation assumes that the ambient fluid is of infinite extent in every direction, so that the pollutant discharge can be characterized as free jet. However, as the pollutants discharges into shallow water depth, water surface and channel bed can influence significantly. Therefore, adequate knowledge of the confinement effects on the dilution, mixing, and spreading of the jet under shallow water flow is of great importance. As microphysical characteristics of jet cannot be thoroughly understood with only analytical approach, physical and numerical investigation provides a key to more in-depth understanding of jets. Hence, one of the objectives of this research is to numerically

investigate the characteristics of circular turbulent non-buoyant jets discharging in shallow water depth ambient fluid.

The most common examples of shallow flows are the sheet flow over land surfaces and river flows over coarse grain surfaces. In both scenarios, roughness height at the surface becomes comparable to the depth of the flow, as a result, affects the behavior of shallow flows. Sheet flow or overland flow develops following a rainfall event as surface runoff. The significance of sheet flow cannot be understated as it is an integral component of the hydrologic cycle. As the surface runoff undergoes various stages of development, it picks up pollutant and erodes the soil surface. As a result, large amount of pollutants and sediments are transported by the sheet flow. Consequently, the pollutant and sediments are discharged in the river, streams, and lakes. The ability of the flow to erode and transport depends on the hydraulic characteristics of the flow. Existing knowledge of the behavior of shallow flows are not conclusive. There is still a need for characterizing the bed shear stress, velocity profile, and roughness coefficients of shallow flows accurately. Therefore, it is of utmost importance to properly understand the hydraulic characteristics of the shallow flow. Hence, one of the objective of the study is to numerically simulate shallow flows and characterize velocity profile, bed shear stress, and resistance coefficients.

Soil erosion during a rainfall event results from the combined effect of the bed shear stress of shallow flow and raindrop impact. As the water depth in sheet flow is small and can become comparable to the size of the raindrop, raindrops can intrude in the sheet flow and impact the surface beneath the raindrop, provided the raindrop possesses sufficient momentum. In addition, in dry surface conditions (prior to the development of sheet flow

and at the start of the rainfall event), raindrop can directly hit the surface and dislodge sediments. Therefore, it is also important to investigate the interaction of the raindrop with the sheet flow and the surface. Water drops corresponding to natural raindrops needs to be generated in order to investigate the interaction between the raindrop and the sheet flow in laboratory. However, the source induces artificial disturbances as the drops are generated in the laboratory. It is therefore important to know the effect and the extent of the source induced disturbances on generated drop. The experimental setup is an important consideration prior to any laboratory investigations and are limited by the space as well as the cost to build the experimental setups. Consequently, this leads to the second objective of this research, which is to provide guidelines to simulate rainfall using an optimum experimental setup based on drop physics.

In summary, this research focused on various applications relating to the shallow flows. It includes circular turbulent jets in shallow water, hydraulic characteristics of shallow flows, and optimum experimental setup for rainfall simulation in laboratory. The ultimate aim of this research is to contribute to the understanding of shallow flows under aforementioned different unique conditions by accomplishing corresponding objectives as discussed above.

CHAPTER 2*

NUMERICAL INVESTIGATION OF CIRCULAR TURBULENT JETS IN SHALLOW FLOWS

2.1 Introduction

Industrial and municipal waste discharges into shallow ambient water are in the form of turbulent jets. Knowledge of dilution, mixing, and spreading of these discharges is essential considering the environmental significance associated with it. Effluent discharges are required to meet the dilution standards as set by the environmental protection agency (Frick et al., 2000). Dilution is dependent upon the fluid properties, flow properties, discharging source geometry, and the environment and geometry of the ambient fluid. Free jet behavior, where the ambient fluid is considered to be of infinite extent, is well understood. However, the presence of the water surface and channel bed can significantly influence flow and dilution characteristics of effluent discharges. Therefore, adequate knowledge of the confinement effects on the dilution, mixing, and spreading of a jet under shallow water flow is of great importance. The primary objective of this research is to numerically investigate the characteristics of circular turbulent non-buoyant jets discharging in shallow stationary ambient fluid.

Turbulent jets have been investigated extensively in laboratory and numerically. For example, Hinze and Zijnen (1949), Albertson et al. (1950), Wygnanski and Fiedler (1969), Johnston (1985), Johnston and Halliwell (1986), Rajaratnam and Khan (1992),

* This chapter has been accepted for publication in the Journal of Hydraulic Engineering as a technical paper.

Hussein et al. (1994), Ead and Rajaratnam (2002), Xu and Antonia (2002), Raiford and Khan (2009), Bhuiyan et al. (2011), Lemanov et al. (2013), Mistry and Dawson (2014), and many others, have experimentally investigated jets under various conditions. While Aziz et al. (2008), Faghani et al. (2011), Islam and Zhu (2011), Ghahremanian and Moshfegh (2014), etc., studied the behavior of jets numerically.

Flow characteristics of turbulent jets are affected by the presence of boundaries surrounding the jet. Jets can be categorized as free jet, wall jet, surface jet, and jets in shallow water (Raiford and Khan, 2009). A free jet occurs when the boundaries have no influence on the jet, i.e., an infinite extent of ambient fluid. Jets are characterized as wall jets or surface jets when only the channel bed or the water surface influences the jet, respectively. Turbulent jets in shallow streams are usually influenced by both channel bed and water surface. As shown in Fig. 2.1, jets in shallow water are characterized using an offset depth, OD, and a submergence depth, SD, usually expressed in the form of submergence ratio ($\mathrm{s} = SD/d$) and offset ratio ($\mathrm{o} = OD/d$), where d is the nozzle diameter. This manuscript investigates the behavior of turbulent jets under different scenarios of submergence ratio and offset ratio through numerical simulation.

Raiford and Khan (2009) studied circular non-buoyant turbulent jets in shallow water with equal offset and submergence ratios of 2, 3, and 4. The growth rate in the vertical and horizontal plane along with decay of the maximum velocity were investigated. Turbulent jets in shallow water may either attach to the water surface or to the bed based upon the Froude number, submergence ratio, and offset ratio (Coates, 1976; Johnston and Halliwell, 1986). Jet attachment is defined as the shift of the point of maximum velocity

toward the channel bed or water surface. Johnston (1985) identified four attachment regimes based on Froude number, submergence ratio, and offset ratio for two-dimensional slot jets.

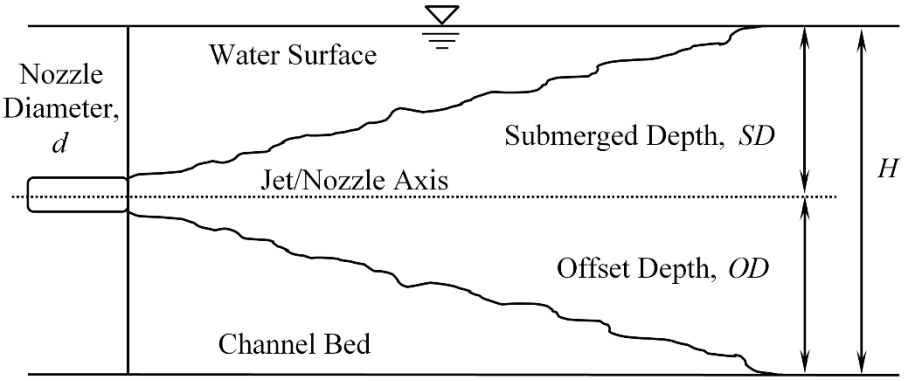

Fig. 2.1 Schematic of turbulent jet in shallow streams (Raiford and Khan, 2009).

Dracos et al. (1992) investigated shallow water plane turbulent jets (with a vertical slot across the ambient water depth) experimentally using laser-Doppler Anemometry (LDA). The study found that secondary currents develop within the jet in shallow water (also reported by Giger et al., 1991) at 2*H* from the nozzle and can influence the flow up to 10*H*. In a cross section normal to the jet axis, the jet experiences constriction in the middle and widening near the bounding surface. The study concluded that the secondary currents did not affect the growth of the jet significantly.

Shinneeb et al. (2011) examined the mean velocity field and turbulence characteristics of a circular turbulent jet in shallow water using Particle image Velocimetry (PIV) system for $H/d = 5, 10,$ and 15. The results revealed that the center line velocity

decayed at a lower rate after $x/d = 50$ and $x/d = 55$ for $H/d = 5$ and 10, respectively, also reported by Raiford and Khan (2009). As oppose to the vertical slot jets (Dracos et al., 1992), the study found that the secondary currents towards the boundaries from the center plane affect the growth rates in horizontal and vertical planes.

The existing studies on circular jets in shallow water lead to new areas to explore. In this study the following features of circular turbulent jet in shallow water are explored numerically. It is important to study the behavior of turbulent jets under asymmetric confinements (i.e., different offset and submergence ratios). In addition, it is necessary to understand the evolution of various jet characteristics (e.g., decay of maximum velocity, growth of jet, and turbulence characteristics) from a free to a confined jet as it propagates. A detailed study is essential that investigates the response of the jet when submergence depth, offset depth, or both are changed systematically. Attachment of jet under different cases of confinement is an important feature as well. Although Johnston (1985) presented a similar case for two-dimensional slot jets, behavior for circular jets under such conditions is yet to be investigated.

2.2 Numerical Simulation Setup

Numerical simulations were performed using commercial computational fluid dynamics software ANSYS Fluent. The ANSYS Fluent uses finite volume method to solve Reynolds-averaged Navier-Stokes (RANS) equations and the associated turbulent closure scheme. Multiphase flow (including air and water phase) were simulated using volume of fluid method. Several turbulent closure schemes are available in ANSYS Fluent, however; Aziz et al. (2008) evaluated the accuracy of different turbulent closure schemes for non-

buoyant, free jets and found that the $k-\varepsilon$ scheme with standard coefficients predicted some of the jet characteristics better than the RNG scheme. In this study, RANS equations along with standard $k-\varepsilon$ turbulent closure scheme are used to simulate circular turbulent jets in shallow water.

Numerical model used in this study was validated with experimental results of Raiford and Khan (2009) for shallow water jets (details are provided in the model validation section). The nozzle geometry and size were based on the experimental setup. Water from a 20 mm diameter pipe was discharged into the simulation tank through a 12.7 mm nozzle. The setup along with coordinates direction, time averaged velocity components ($u, v,$ and w), and turbulent velocity fluctuations ($u', v',$ and w') are shown in Fig. 2.2. The origin of the coordinate system is placed at the center of the nozzle exit. The vertical and horizontal planes are through the jet axis, which is along the locus of the maximum velocity. The simulation tank was 2 m long (*x*-direction), 1 m wide (*z*-direction), and 0.8 m high (*y*-direction). These dimensions were selected such that the side boundaries and the downstream boundary would have no influence on the jet. A uniform velocity profile was provided at the inlet (upstream of the approach pipe). To achieve the fully developed velocity profile, the pipe length was set to $62D$. Pressure boundary condition was imposed at the boundaries normal to the *z*-direction and the downstream boundary normal to the *x*-direction. Top boundary (located at the top of the air phase) was modelled as free-slip boundary with zero shear stress. All other boundaries were modelled as non-slip wall boundary with standard wall functions. The results presented below are mesh independent.

The maximum relative velocity differences are within 2% of the finest grid when the total number of elements was increased by 200%.

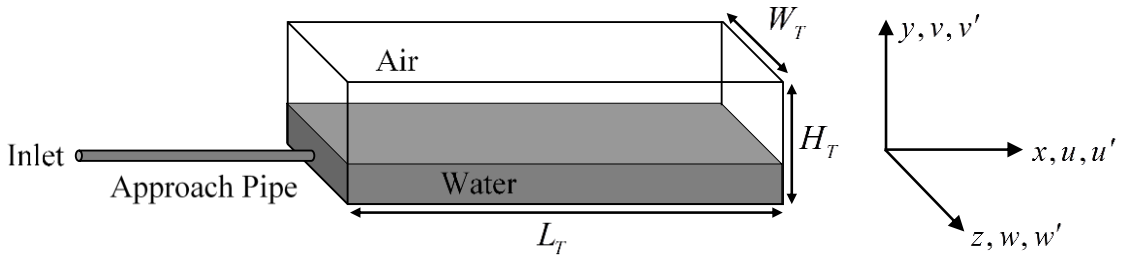

Fig. 2.2. Schematic of geometry setup used in numerical simulation.

2.3 Model Validation

The numerical model was first validated with the experimental results for a free circular turbulent jet using the setup shown in Fig. 2.2. Experimental data of Hussein et al. (1994) for centerline velocity decay, growth rate, and turbulent normal and shear stresses in the developed zone (up to $x/d = 50$) of the jet were used to validate the numerical model. The error between the measure and simulated results were assessed using Nash-Sutcliffe efficiency coefficient (NSE) (Nash and Sutcliffe, 1970). The NSE ranges from $-\infty$ to 1, with 1 being a perfect fit. The comparison showed that the model results were in good agreement with the experimental results for decay of maximum velocity (NSE=0.95). The model is able to simulate turbulent normal ($u_{rms} = \sqrt{\overline{u'u'}}$) and shear stresses ($\overline{u'v'}$) accurately with NSE values of 0.93 and 0.86, respectively. The model over predicts the growth rate by 10% and the turbulent normal stress in vertical direction by 27%. This over-prediction arises due to the use of $k-\varepsilon$ turbulent closure schemes with

standard coefficients (Pope, 1978). More accurate prediction of growth rate is possible by adjusting the coefficients; however, the aim is to use the model for shallow water jets as such standard coefficient are used throughout the study.

Confined jet simulation results were also verified. The experimental results of Raiford and Khan (2009) for offset and submergence ratios of 2 were used to verify growth rate (NSE=0.96), decay of maximum velocity (NSE=0.97), and locus of maximum velocity (NSE=0.78). The low NSE value for the locus of maximum velocity may be due to the difficulty in locating the maximum velocity in the laboratory as the profile becomes more uniform. Mean flow velocity profiles and turbulent flow characteristics at various sections were also verified using Shinneeb et al. (2011) experimental results. The results revealed that the model is capable of capturing salient mean and turbulent characteristics of circular confined jets.

2.4 Result and Discussion

The primary objective of this study is to quantify the effects of confinement corresponding to $x/d \leq 50$ for the turbulent circular jets in shallow water. According to Ball et al. (2012), the flow development spanning from near to intermediate field ($0 \leq x/d \leq 30$) plays the most important role in engineering application of the jets. Furthermore, the normalized maximum velocity falls to about 0.1 at $x/d = 50$. As such, the observation domain was limited to $x/d = 50$ in this study. The limit of confinement, which corresponds to the region in the vertical plane in which the presence of either the water surface or the channel bed influences the characteristics of the jet (for $x/d \leq 50$),

was also investigated. The turbulent jet can be characterized as a free jet for the zone of interest ($x/d \leq 50$) if the boundaries (i.e., the water surface and the channel bed) are located beyond that limit. Analysis from this study showed that, offset ratio and submergence ratio of 24 suffice the condition for a free jet within the zone of interest. Thus, the behavior of turbulent jets in shallow water for offset and submergence ratio as high as 24 to as low as 1 was investigated.

In order to evaluate the effect of submergence ratio and offset ratio on the jet, submergence ratio was gradually decreased starting from 24 to 14, 10, 6, 4, 3, 2, and 1 for different offset ratios (24, 14, 10, 6, 4, 3, 2, and 1). Several jet characteristics such as decay of maximum velocity, growth of jet in the horizontal plane, growth of jet in the vertical plane, locus of maximum velocity, axial turbulence profiles, and turbulent shear stress are used as the principal indicators for characterizing the extent and effect of confinement.

2.4.1 Decay of maximum velocity

Decay of maximum velocity is an important parameter for characterizing the dilution of a jet. Effect of symmetric confinement on decay of maximum velocity is presented in Fig. 2.3. The maximum distance up to which the maximum velocity decay follows the free jet profile depends on the submergence and offset ratios. For example, this distance is about $14d$ for o1s1 (i.e., offset ratio 1 and submergence ratio 1) case whereas it is about $28d$ for o2s2 case. The maximum velocity decays at a lower rate under higher degree of confinement. The confinement results in lower entrainment and lower decay of the maximum velocity. The maximum velocity decays as a free jet for o6s6 and higher ratios.

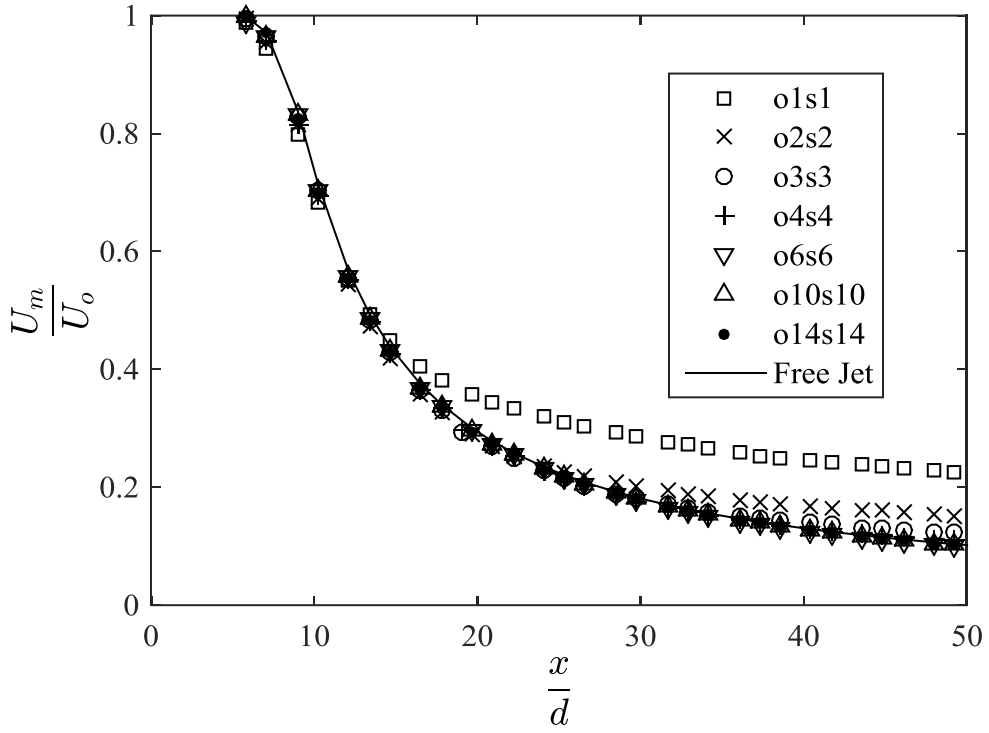

Fig. 2.3. Comparison of maximum velocity decay of jet for symmetric confinement

Effect of one sided confinement was studied by varying offset or submergence ratio for a fixed submergence or offset ratio, respectively. The fixed submergence and offset ratios were set to 24 to guarantee that the jet is unaffected by that boundary. Results reveal that the maximum velocity decay for fixed offset ratio and fixed submergence ratio is similar to that of a free jet up to a minimum distance of $x/d = 15.5$ and $x/d = 12.5$, respectively. The results for varying submergence and offset ratios for maximum velocity differences at $x/d = 50$ are presented in Table 2-I. The results clearly show that the maximum velocity decays at a lower rate for jets closer to the bed than for the jets closer to the surface. In the case of bed confinement, the presence of boundary layer enhances the confinement effect resulting in lower rate of decay of velocity in the confined zone which

in turn influences the maximum velocity in the jet (further explanation is provided in the following section).

Table 2-I. Comparison of results from decay of maximum velocity profiles under various scenarios of confinement. The differences corresponds to the value at $x/d = 50$.

Case	% Relative difference with respect to free jet						
o24	s1	s2	s3	s4	s6	s10	s14
	39.78 %	36.2%	24.3%	9.65%	0.2%	0.2%	0.2%
s24	o1	o2	o3	o4	o6	o10	o14
	49.6%	40.35 %	26.9%	11.87 %	0.9%	0.9%	0.9%

2.4.2 Analysis of velocity profiles

The velocity profiles in the horizontal and vertical planes through the jet axis are analyzed to investigate the confinement effect on the jet. Analysis reveals that the entrainment is suppressed in the vertical plane by the confining surface. As a consequence, velocity decays at a comparatively lower rate. This effect starts at the outermost edge of the jet boundary and progresses inward as the jet travels downstream. The development of velocity profiles in the vertical plane along the jet axis is shown in Fig. 2.4. The results show that the confinement does not have any effect up to $x/d = 6$ for all the cases. Farther downstream ($x/d = 20$), the effect starts to manifest and the velocities in the confined zones becomes higher than the free jet (due to suppressed entrainment). In addition, it is found that the point of maximum velocity shifts toward confining surface. The effects become more pronounced at the downstream sections ($x/d = 30$).

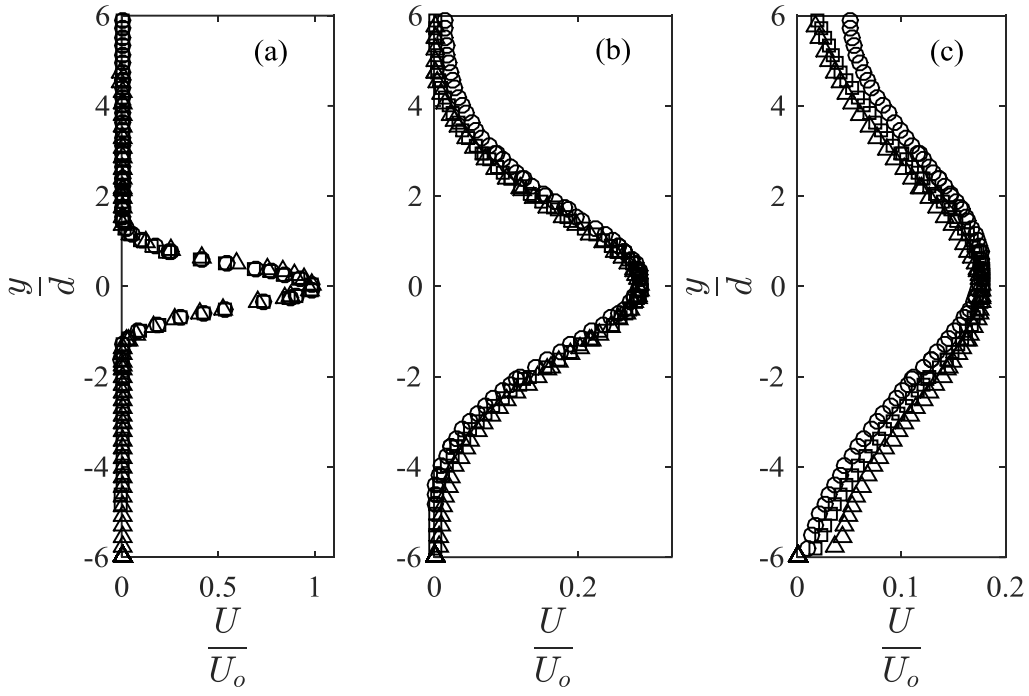

Fig. 2.4. Velocity profiles in the vertical plane for Free Jet (□), o6s24 (Δ), and o24s6 (○) at (a) $x/d = 6$, (b) $x/d = 20$, and (c) $x/d = 30$.

In addition, the velocity profile on the opposite side of the confined zone does not match the free jet as shown in Fig. 2.5(a). However, this deviation from the free jet is a result of the jet moving toward the confining surface as a whole. This is shown in Fig. 2.5(b) where the maximum velocity for the confined jets are adjusted to the location of the free jet. The results show that the velocity profiles opposite to the confining surface matches with the free jet for certain distance downstream of the nozzle. In the sections farther downstream, the effect of the confinement are observed in the whole jet. The surface confinement affects the velocity at the outer edge more than the bed confinement initially as shown in Fig. 2.5(b). The reason for this behavior may be related to the boundary layer

development near the bed and the fact the velocity at the bed must be zero. So the initial deviation from the free jet is limited at the outer edge of the velocity profile. However, farther downstream the boundary layer growth enhances the confinement effect and the velocity profile are impacted more than water surface confinement of equal order (see Fig. 2.6(c)).

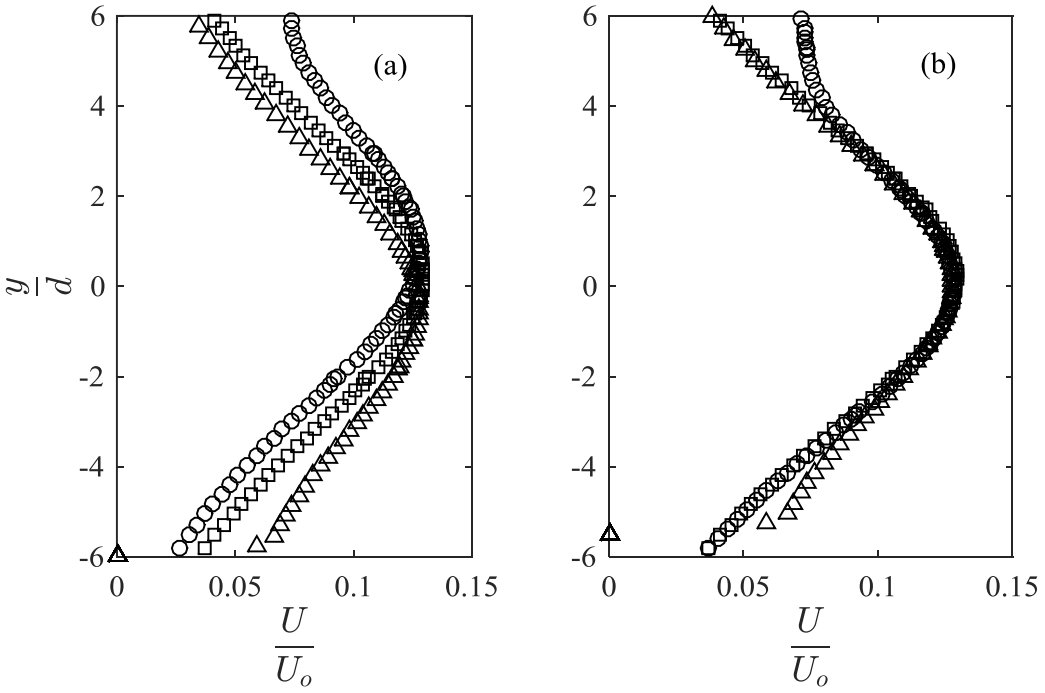

Fig. 2.5. Velocity profiles in the vertical plane for Free Jet (□), o6s24 (Δ), and o24s6 (○) at $x/d = 40$ for (a) original axis and (b) adjusted axis.

The velocity profiles were also analyzed to investigate extreme cases of confinement (o1s24 and o24s1). The development of velocity profiles in the vertical plane along the jet axis is shown in Fig. 2.6. Analysis reveals that the velocity at the outermost edge of the jet gets affected first and the effect progresses inward as the jet travels

downstream. In addition, due to severe confinement, the jet boundary interacts with the confining surface within a short distance of the nozzle. This interaction results in the change of velocities across the whole jet (as shown in Fig. 2.6). Fig. 2.6(b, c) clearly shows that velocity profiles opposite to the confining surface are affected as well. Due to suppressed entrainment, the velocities in the confined jets are higher than that in the free jet throughout. The same phenomena is observed but at a distance progressively farther from the nozzle at a lower degrees of confinement. Fig. 2.6(b, c) shows that the effect of the bed confinement is more pronounced compared to the water surface confinement. The boundary layer enhances the confinement effect and as a result velocities decay at a comparatively lower rate than the water surface confinement case. The o10s10 case is also shown in Fig. 2.6 to demonstrate that for lower degree of confinement the velocity profiles may not be affected for some distance downstream of the nozzle (in this case up to $x/d = 50$). It should be noted that the velocity profiles all along the lower or upper circumference of the jet (based on the confinement) are affected. The velocity profile at the center plane is affected first (in terms of distance from the nozzle) followed by the offset profiles (i.e., profiles away from the center plane).

Velocity profiles in the horizontal plane through the jet axis are analyzed as well. Fig. 2.7 shows the development of velocity profiles for extreme cases of confinement. As before, the confinement effect decreases the decay rate of velocity as such the velocities are higher than the free jet conditions. Results reveal that for extreme confinement, where the velocity at the jet axis is almost immediately impacted, the confinement effect starts at the jet axis and progresses outwards in the horizontal plane as the jet travels downstream.

In addition, the increase in velocity in the mid plane actually makes the velocity profile steeper than the free jet. This should have a significant effect on the growth rate in the horizontal plane (discussed later). In addition, this also shows that the confinement affects the velocity profiles in the vertical and horizontal in totally different manners.

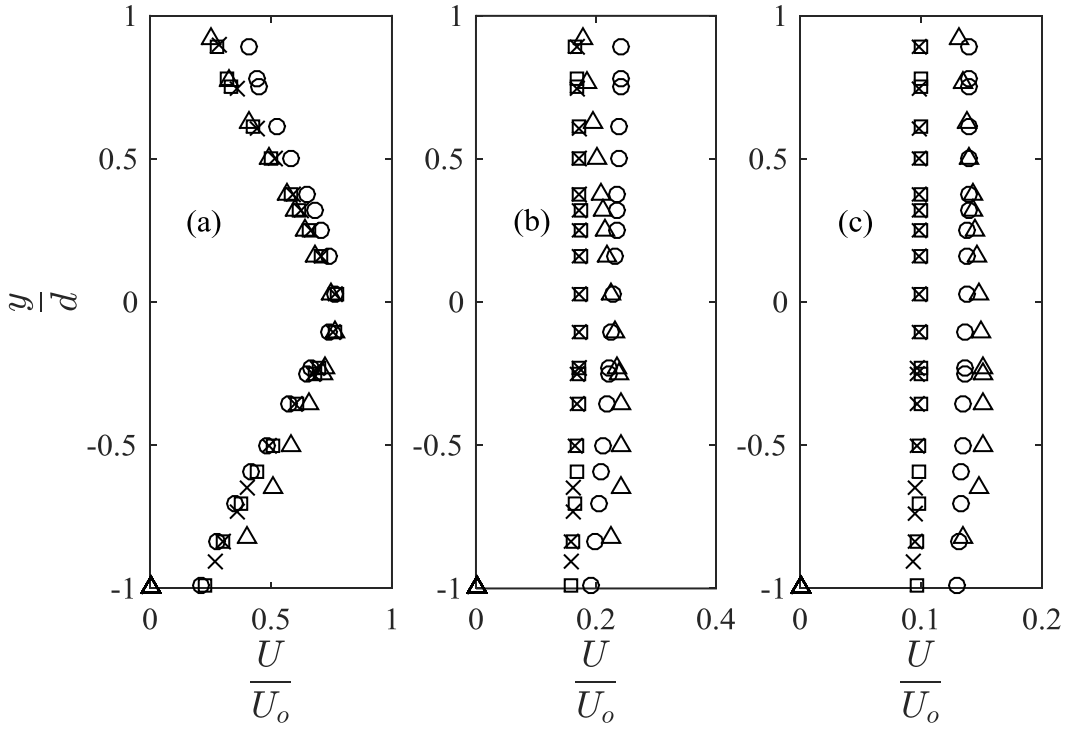

Fig. 2.6. Velocity profiles in the vertical plane for Free Jet (□), o10s10 (×), o1s24 (Δ), and o24s1 (○) at (a) $x/d = 10$, (b) $x/d = 30$, and (c) $x/d = 50$.

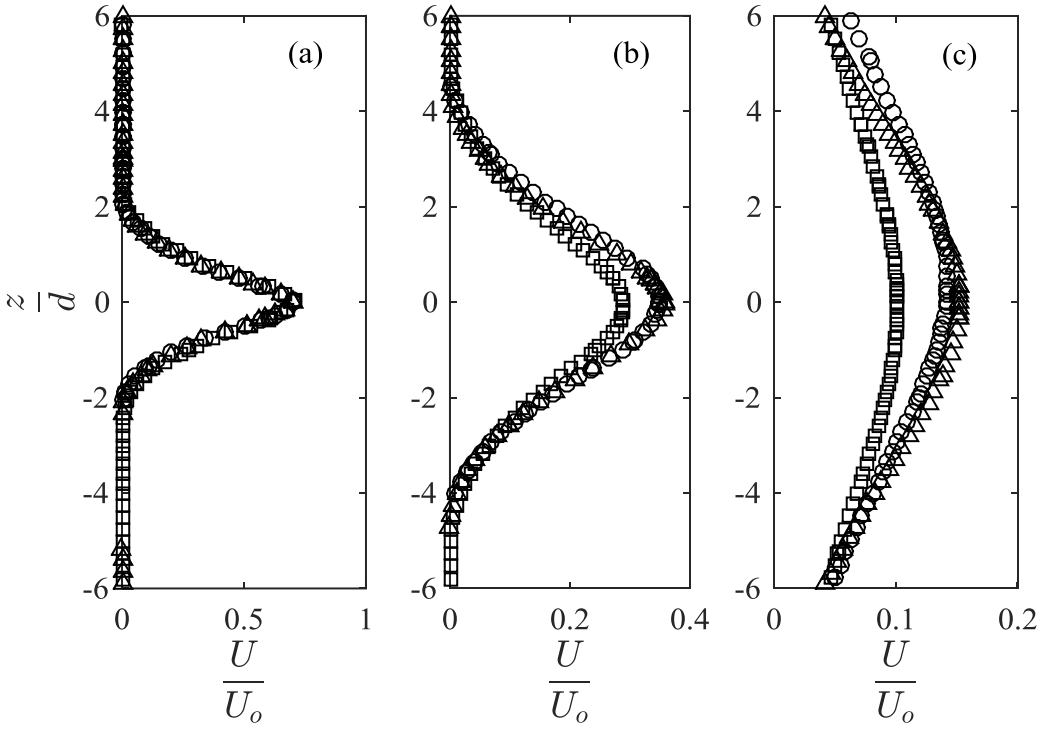

Fig. 2.7. Velocity profiles in the horizontal plane for Free Jet (□), o1s24 (Δ), and o24s1 (○) at (a) $x/d = 10$, (b) $x/d = 20$, and (c) $x/d = 50$.

2.4.3 Locus of maximum velocity

It was established in the preceding section that the point of maximum velocity shifts toward the confining surface and is defined as jet attachment. Jet attachment (which includes start of the maximum velocity shift and final attachment) is a function of the proximity of the confining surfaces. Previously, it was reported that the interaction between the vortices at the jet boundary and the confining surfaces generates secondary flows toward the boundary (Foss and Jones, 1968, Dracos et al., 1992, Shinneeb et al. 2011), which results in the modification of the velocity profiles in the vertical and horizontal planes. In this study, lower decay of velocity due to suppressed entrainment is identified

as the primary reason for jet attachment. In addition, it is found that the jet as a whole moves toward the confining surface and not just the locus of maximum velocity.

Jets in shallow water attach to the water surface for deep offset and shallow submergence ratios. The loci of the maximum velocity for various degrees of submergence are shown in Fig. 2.8. For very shallow submergence, surface waves of significant height are generated and as such the water surface may be higher than the still water surface. The loci of the maximum velocity are higher than the still water surface levels for o24s1 and o24s2. For submergence ratio up to 3, the jet attaches to the surface within $x/d = 50$. The decay of maximum velocity is unaffected for submergence ratio equal or greater than 6; however, the locus of the maximum velocity is affected for submergence ratios lower than 20.

In cases of deep submergence and shallow offset ratio, the confined jets attach to the channel bed (see Fig. 2.9). As oppose to shallow submergence cases, the maximum velocity does not reach the bed (due to boundary layer development) and stays approximately $0.5d$ above the bed. For offset ratio greater than 3, the jet attachment occurs after $x/d = 50$. In all cases, the maximum velocity shifts toward the bed in a linear manner.

Based on the observations of the one sided confinement effects on the turbulent jets, the following observations can be made. First, the maximum magnitude of the shift is comparatively higher for surface confinement cases than the bed confinement cases. For example, the maximum shift for o3s24 case is about $2.1d$ whereas it is $3d$ for o24s3 case. The obvious reason for such behavior is the presence of boundary layer at the vicinity of channel bed and as such the shift is limited for bed confinement cases. In addition, the shift

starts comparatively closer to the nozzle for surface confinement compared to the bed confinement cases. For example, the shift starts at around $15d$ for o24s3 case whereas it is starts at $20d$ for o3s24. This suggests that for an equal order of one sided confinement, the surface confinement effects manifest before the bed confinement. One possible reason for such behavior is that the flow in the upper portion can accelerate easily (zero shear at the water surface) compared to the flow in the lower portion which is restricted by the channel bed.

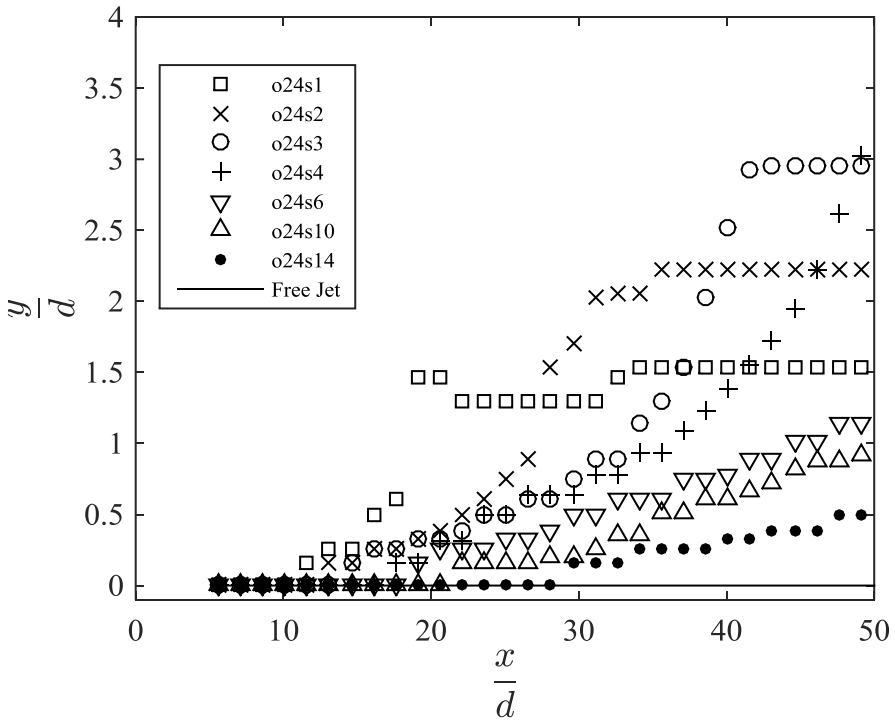

Fig. 2.8. Locus of maximum velocity in the vertical plane for variable submergence and fixed offset.

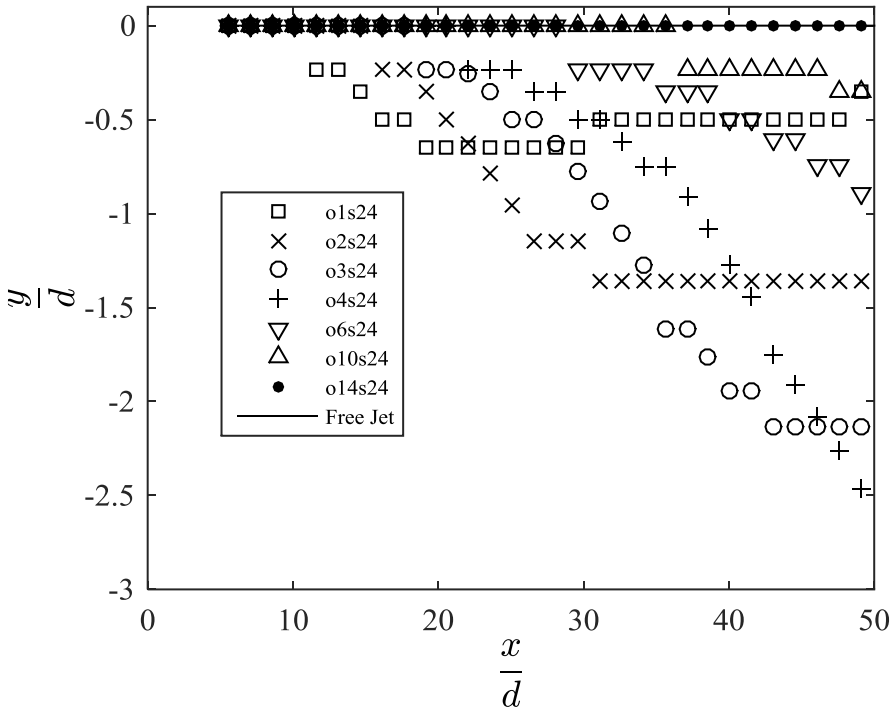

Fig. 2.9 Locus of maximum velocity in the vertical plane for variable offset and fixed submergence.

Under asymmetric conditions, where both water surface and channel bed influence the jet, jets shift toward the closest confining surface. For example, different submergence ratios for o3 and o4, and different offset ratios for s3 and s4 are shown in the Fig. 2.10. The figure clearly shows that turbulent jets attach to the nearest confining surface. In addition, for some cases where the offset ratio is lower than the submergence ratio, jet moves toward the surface initially and then ultimately deflects toward the bed (o3s4 and o4s6). As discussed in the one sided confinement cases and analysis of velocity profiles section, the surface confinement effects manifest before the channel bed; however, eventually the bed

confinement effects overtake due to enhanced confinement resulting from the boundary layer development.

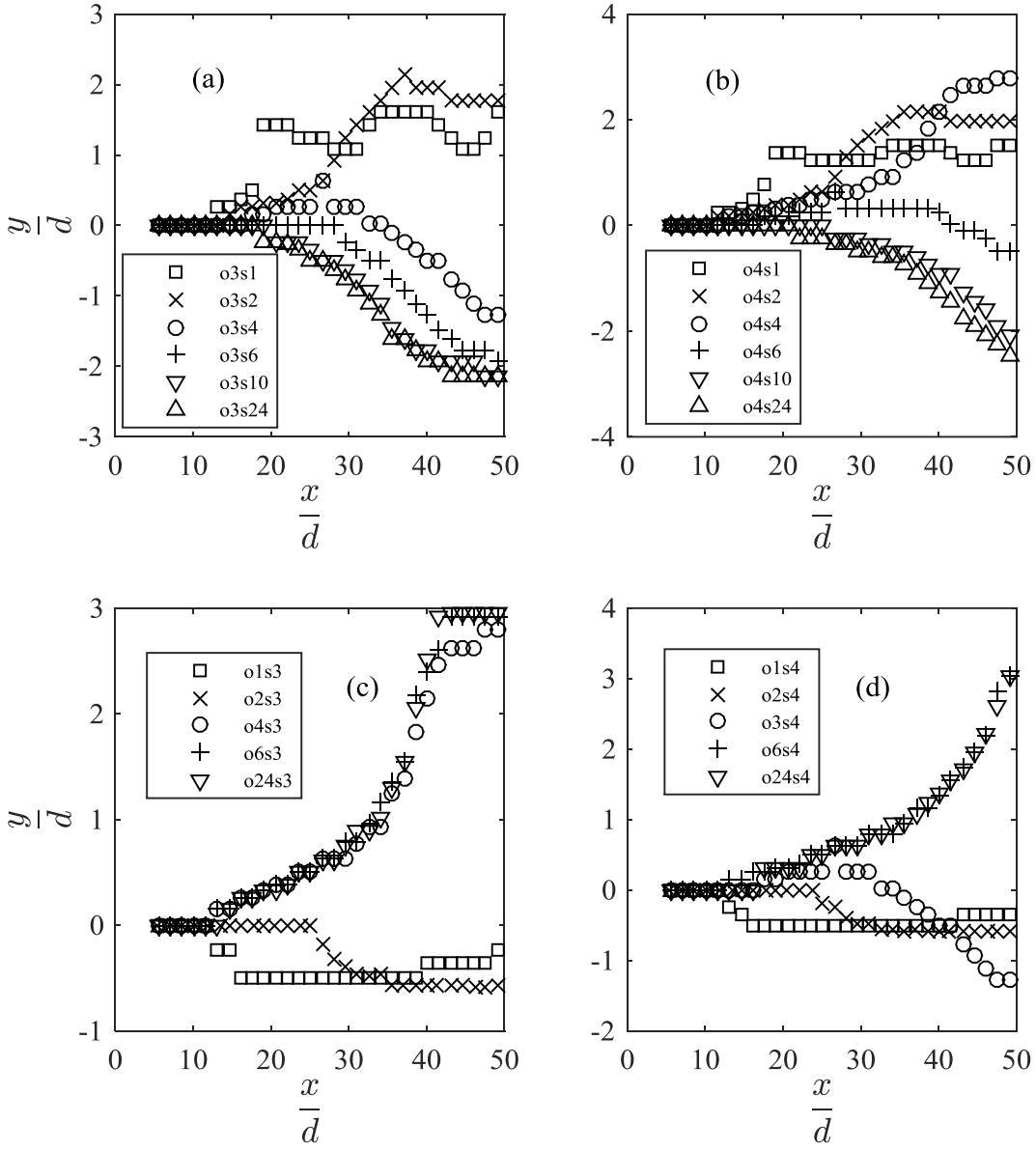

Fig. 2.10 Locus of maximum velocity in the vertical plane under asymmetric confinement for fixed a) o3, b) o4, c) s3, and d) s4.

Turbulent jet eventually attaches to the channel bed under symmetric confinement cases as shown in Fig. 2.11. Presence of boundary layer at the channel bed enhances the confinement effect on the offset side. Consequently, jet moves toward the channel bed for identical submergence and offset ratios. The results also show that the jet initially moves toward the water surface except for o1s1 where the jet is affected by the bed immediately. As discussed before, surface confinement effects manifest before the bed confinement effects; however the jet deflects toward the bed eventually. For o4s4 and higher ratios, the eventual movements toward the bed takes place beyond $x/d = 50$. For smaller ratio, such as o1s1, the figure shows that the maximum velocity and not the jet ultimately shifts toward the surface as a result of flow acceleration in the upper part. The same phenomenon is observed for o2s2 immediately after $x/d = 50$, and as the ratio increases the distance where the ultimate upward shift in the maximum occurs, moves farther downstream.

The results of the jet attachment for both symmetric and asymmetric cases are summarized in Table 2-II. For deep submergence, the jet always attaches to the bed while it attaches to the surface for shallow submergence. This may help identify pollutant accumulation zones and conditions under which bed scour may be of concern.

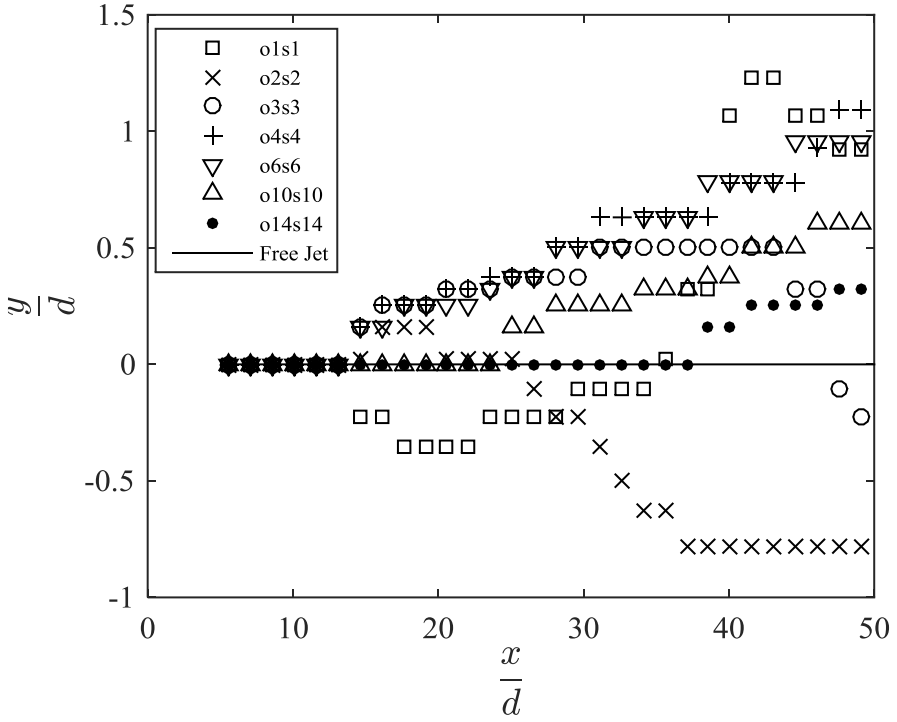

Fig. 2.11. Locus of maximum velocity in the vertical plane for symmetric confinement.

Table 2-II. Attachment regimes for turbulent jets in shallow water. In the table, bed and surface attachments are represented by B and S, respectively. C denotes that the locus of the maximum velocity stay around the center of the jet ($\leq \pm 0.5d$).

Offset Ratio, o	Submergence Ratio, s							
	1	2	3	4	6	10	14	24
1	B	B	B	B	B	B	B	B
2	S	B	B	B	B	B	B	B
3	S	S	B	B	B	B	B	B
4	S	S	S	S[a]	B	B	B	B
6	S	S	S	S	S[a]	B	B	B
10	S	S	S	S	S	S[a]	B	B
14	S	S	S	S	S	S	C	C
24	S	S	S	S	S	S	C	C

[a]Bed attachment does not manifest by $x/d \leq 50$. As such, they are governed by the initial deflection zone and labeled as surface attachment.

2.4.4 Growth of Jet

Growth of a jet is an indicator of mixing and entrainment characteristics of the jet. Growth of a jet is usually expressed in terms of jet half-width (b) and is defined as the distance from the point of maximum velocity (U_m) to where $U = 0.5U_m$. For confined jets, growths are analyzed in horizontal and vertical planes passing through the jet axis. In the case of a vertical plane, the growths are analyzed separately in the upper and lower parts of the jet with respect to jet axis. For symmetric confinement of o20s20 and above, the confinement has no effect on the growth of a jet up to $x/d = 50$ in both horizontal and vertical planes.

Jet growth (b/d) along downstream distance in the horizontal plane through the jet axis is shown in Fig. 2.12. For symmetric confinements (Fig. 2.12 (a)), the growths are lower than the free jet for all cases. This may be attributed to jet contraction in the horizontal plane due to the development of secondary flow as discussed earlier. Such behavior of confined turbulent jets in shallow water was also observed by Shinneeb et al. (2011), who reported that the growth of jet in the horizontal plane became lower while it became higher in the vertical plane.

For extreme cases of symmetric or one sided confinements of ratios 1 and 2, the growth is lower than that of a free jet and the growth rate decreases with the downstream distances. This is the results of lower decay of the maximum velocity impacted immediately downstream of the nozzle. As such the velocity profiles in the horizontal plane are steeper with lower growths. However, this behavior diminishes as the offset or

submergence ratios increase. In the case of one sided confinements, the bed affects the growth of the jet more than the water surface as shown in Fig. 2.12(b, c).

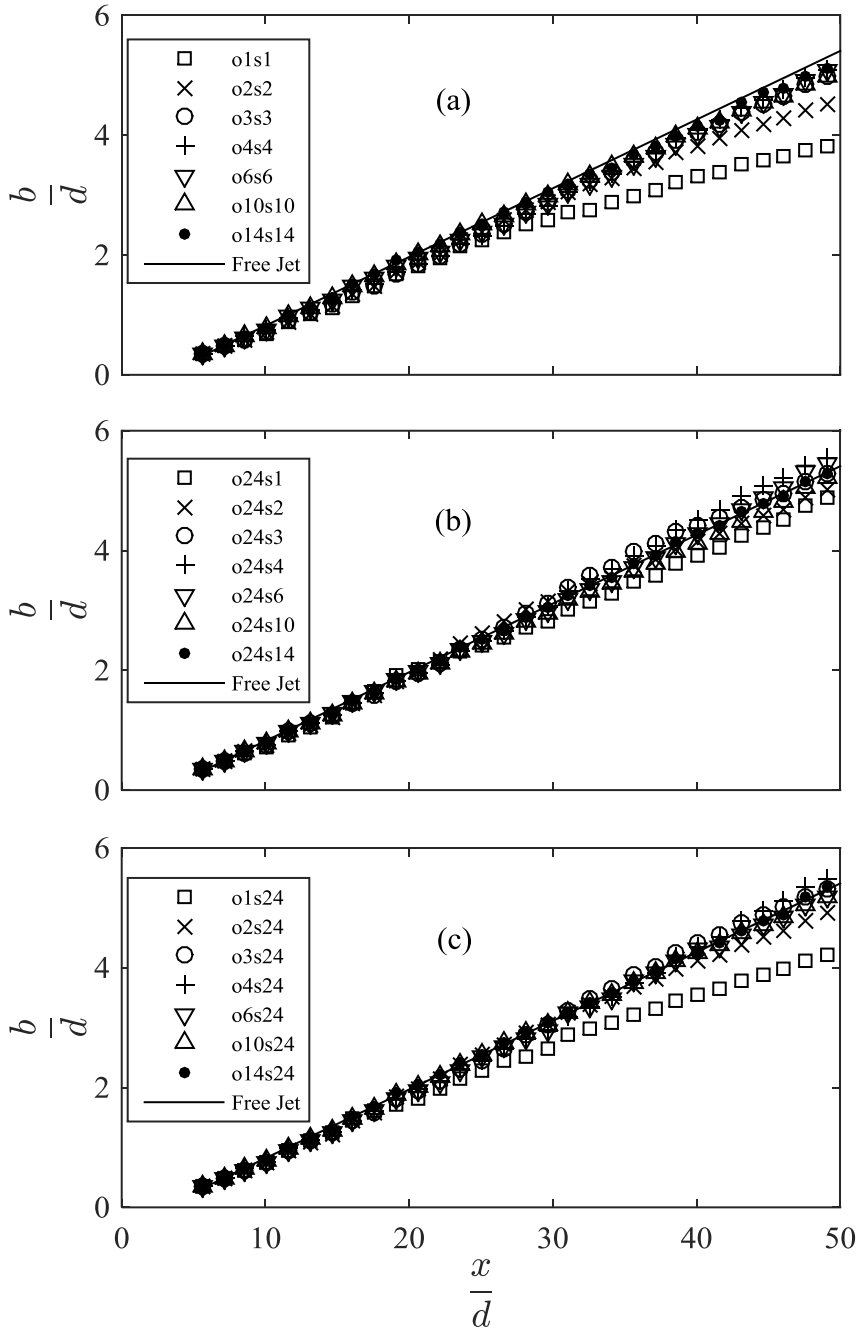

Fig. 2.12. Evolution of jet growth along downstream distance in the horizontal plane for (a) symmetric confinement, (b) varying submergence ratios, and (c) varying offset ratios.

For one sided confinement with submergence and offset ratios of 3 or 4, the growth of jet is higher initially; however the growth eventually becomes lower than the free jet. This behavior is related to the velocity profile development in the horizontal plane. The velocity profiles in the horizontal plane have two different zones. In the first zone, the velocities in the outer zone are higher resulting in a more uniform velocity profile and hence the higher growth. In the second, the lower decay of the maximum velocity is more pronounced, resulting in a steeper velocity profile and lower growth. For cases of submergence and offset ratios of 6 and higher, this phenomenon takes place beyond $x/d = 50$.

Evolution of jet growth in the upper portion of the vertical plane is shown in Fig. 2.13. Results reveal that the jet growth is higher than that of free jet for all cases of symmetric confinement (Fig. 2.13 (a)). As explained in the analysis of the velocity profile section, velocity decay is lower than that of free jet as a result of the suppression of entrainment at the water surface, causing the velocity profile to be more uniform. As such the growth rate is higher than the free jet. It should be noted that in some case the growth rate cannot be determined in the upper part due to maximum velocity reaching the surface and the velocity profile becoming more uniform.

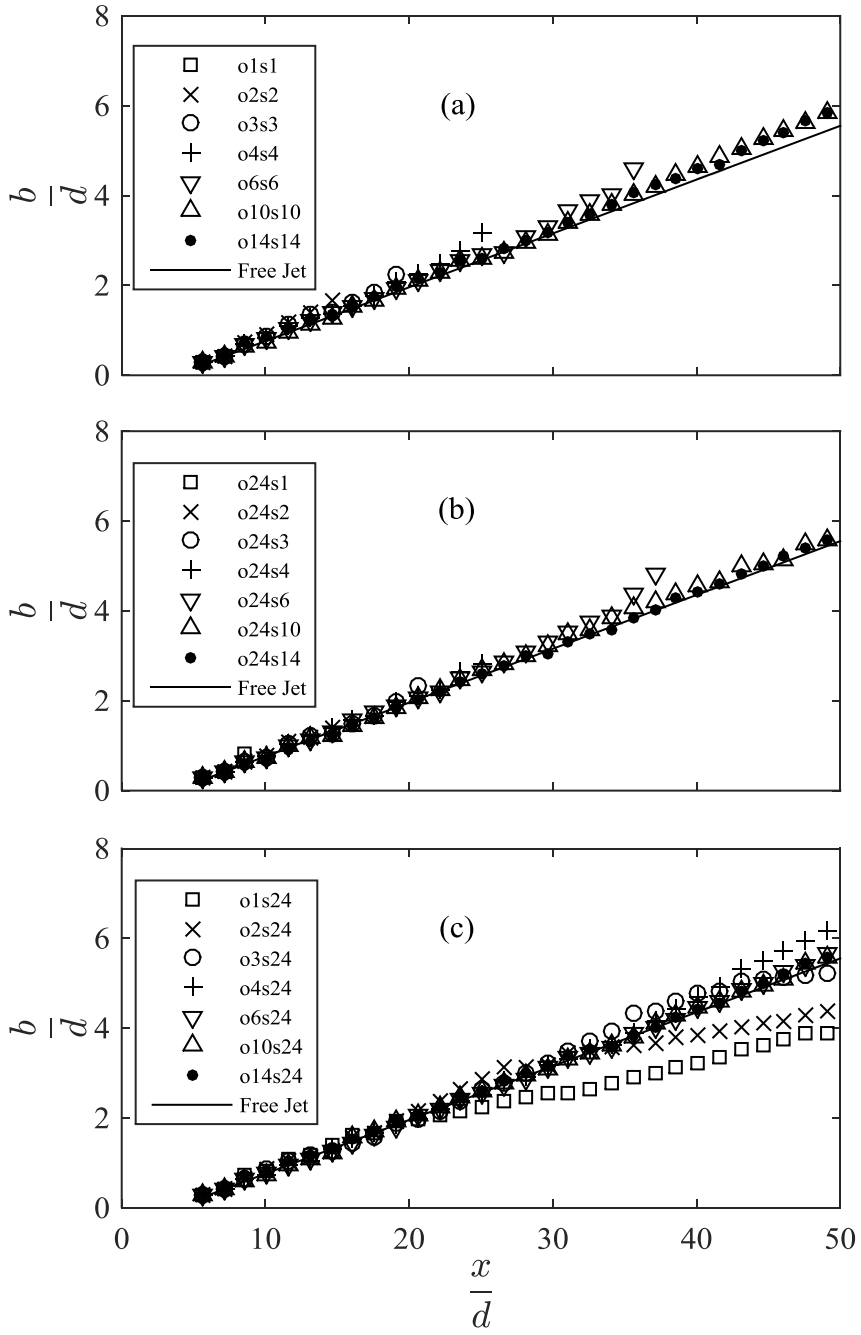

Fig. 2.13. Evolution of jet growth along downstream distance in the vertical plane (upper portion) for (a) symmetric confinement, (b) varying submergence ratios, and (c) varying offset ratios.

For one sided confinement cases, the jet growth is significantly affected for offset/submergence ratio lower than 10. For the water surface confinement (Fig. 2.13(b)), the locus of maximum velocity shifts toward the water surface. As such, the growth is always greater than that of a free jet for varying submergence ratios. The growth rate increases as the jet moves closer to the surface. In the case of varying offset ratios (Fig. 2.13(c)), the growth has three distinct regions. In the near region, the growth is the same as free jet. In the mid region, growth is higher than the free jet, whereas it is lower than the free jet in the far region. The mid region starts when the maximum velocity starts to deviate from the free jet profile, which causes the velocity profile to become more uniform resulting in a higher growth of the confined jet. The far region starts when the jet attaches to the bed. In this region, the growth rate continues to decrease due to shear and boundary layer development near the bed, which affects the velocity across the whole jet.

Evolution of the jet growth in the lower portion of the vertical plane is shown inFig. 2.14. Results show that for the symmetric confinement the jet growth is minimally affected for o10s10 and higher submergence/offset ratios (Fig. 2.14(a)), while the effect on growth increases with the degree of confinement. The jet growth is higher than that of a free jet for all the cases under symmetric confinement cases till the jet half-width starts to interact with the channel bed. Consequently, the jet growth is limited by the offset depth and presence of the boundary layer. The reason for higher jet growth is explained in the velocity profile section. The behavior for one sided bed confinement (Fig. 2.14(c)) is similar to the symmetric confinement cases.

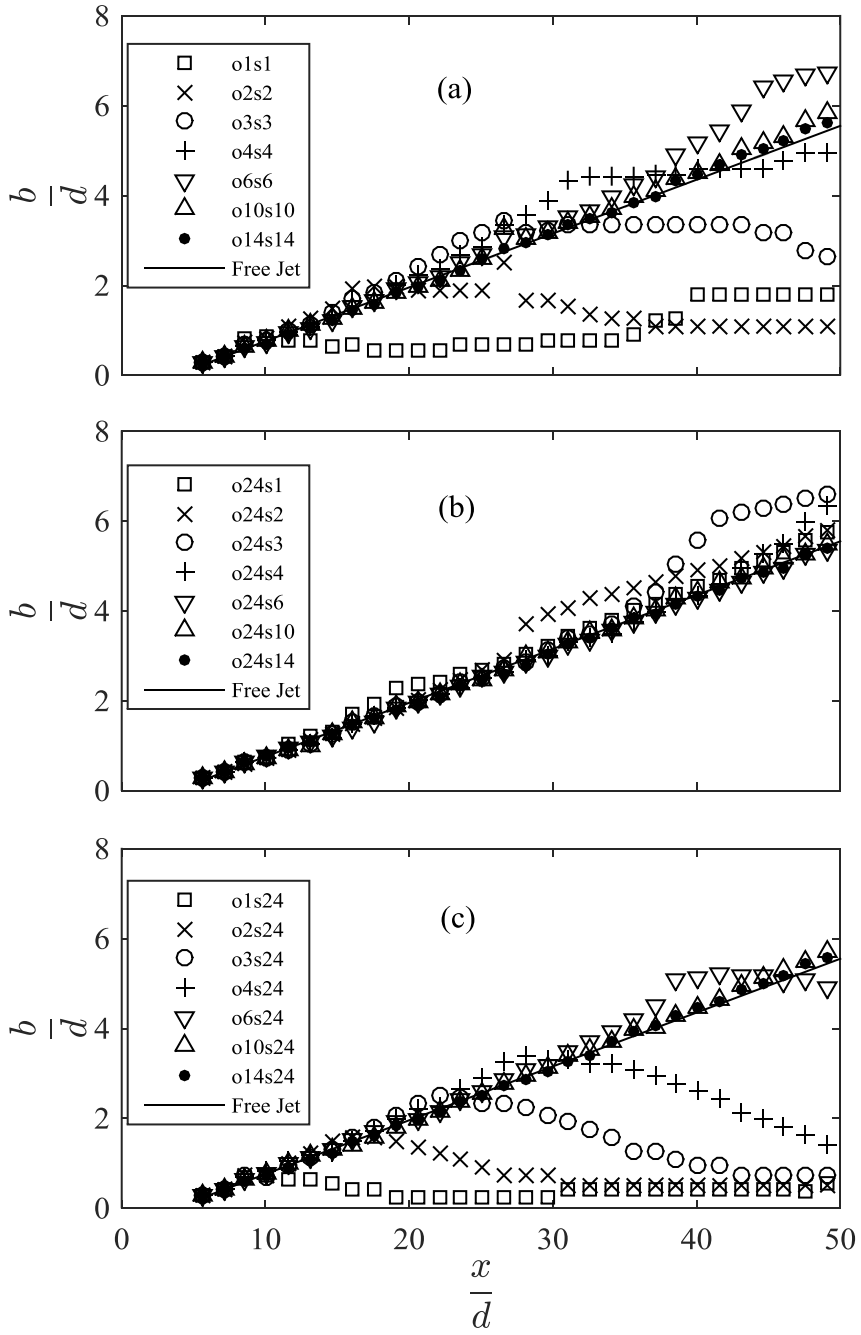

Fig. 2.14. Evolution of jet growth along downstream distance in the vertical plane (lower portion) for (a) symmetric confinement, (b) varying submergence ratios, and (c) varying offset ratios.

In case of varying submergence ratios, the growth is the same as the free jet initially. Farther downstream, the growth rate suddenly increases and is related to the maximum velocity reaching the surface, resulting in lower velocity decay and relatively uniform velocity profile throughout the jet. In this region, the growth rate slows down after relatively sharp increase and approach that of a free jet, although always higher than the free jet.

2.4.5 Turbulence profiles

Turbulence normal ($u_{rms} = \sqrt{\overline{u'u'}}$) and shear stresses ($\overline{u'v'}$) profiles for shallow water confined jets are analyzed and compared to understand the effect of confinement on the turbulence characteristics of a circular turbulent jet. Turbulent normal and shear stresses profiles in the horizontal and vertical planes passing through the jet axis were used to assess the confinement effect on the turbulence characteristics. Analysis reveal that the confinement have minimal effects on the turbulence characteristics up to $x/d = 50$ for offset/submergence ratios of 20 and higher.

In the case of symmetrical confinement, normalized turbulent normal stress profiles in the vertical plane at $x/d = 30$ and 50 are shown in Fig. 2.15. The bed effects the turbulent normal stress more than the water surface. In addition, the turbulent normal stress are lower near the bed and higher near the water surface, which may be related to boundary layer at the bed and waves at the water surface. The confinement effects grow as the jet travels downstream. The center of the jet is not affected significantly by the confinement, this is also reported by Shinneeb et al. (2011). Also, the turbulent normal stress gets affected at the outer edges of the jet and the effects moves inward toward the core. The

turbulent shear stress profiles in the vertical plane at $x/d = 30$ and 50 are shown in Fig. 2.16. The turbulent shear stress is affected equally by the bed and water surface confinement, except for the region very close to the bed (boundary layer) and water surface (surface waves).

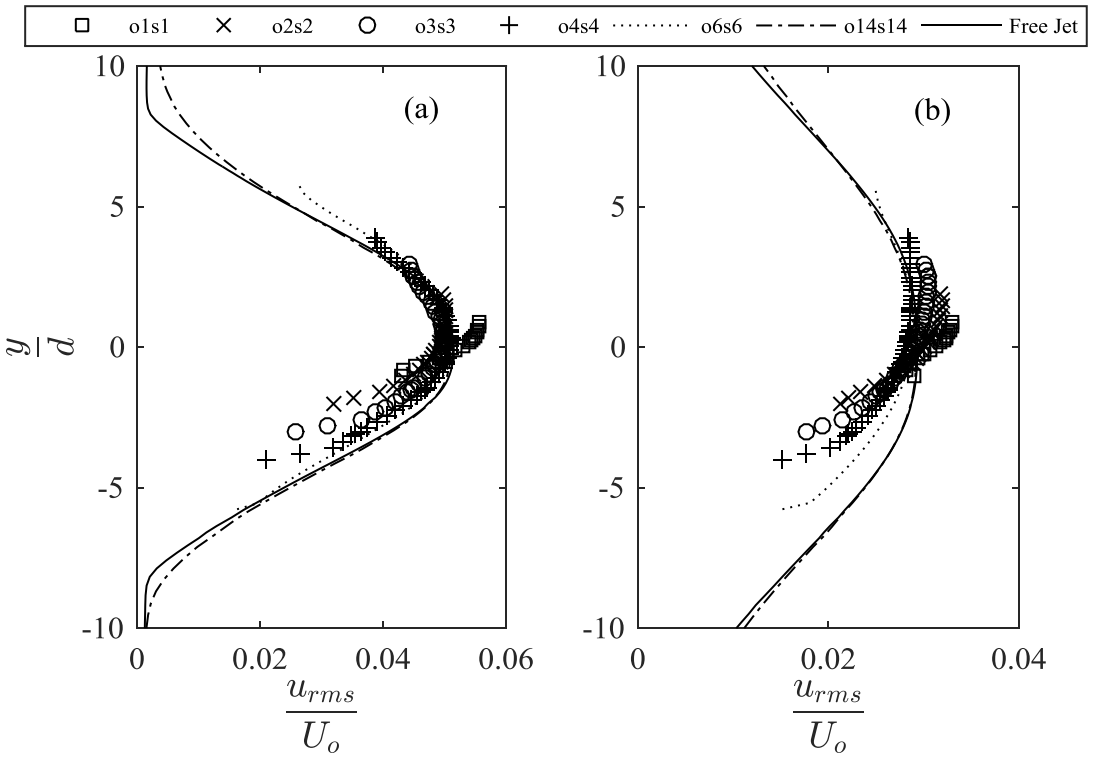

Fig. 2.15. Turbulent normal stress profiles for symmetric confinement at (a) $x/d = 30$, (b) $x/d = 50$.

For bed confinement cases, the turbulent normal stress is suppressed near the bed and the effect propagates inward as the jet travels downstream. Similar behavior is observed in the case of turbulent shear stress profiles. The turbulent normal and shear stresses are higher in the upper half of the jet close to the jet axis. This indicates higher

mixing in the upper half of the jet. For the water surface confinement, the turbulent normal stress is higher than that in the free jet. The effect starts at the outer edge in the upper half and propagates inward and to the lower half of the jet further downstream. The turbulent shear stress is lower in the upper half and higher in the lower half. The results indicate that bed confinement is related to lower mixing compared to water surface confinement.

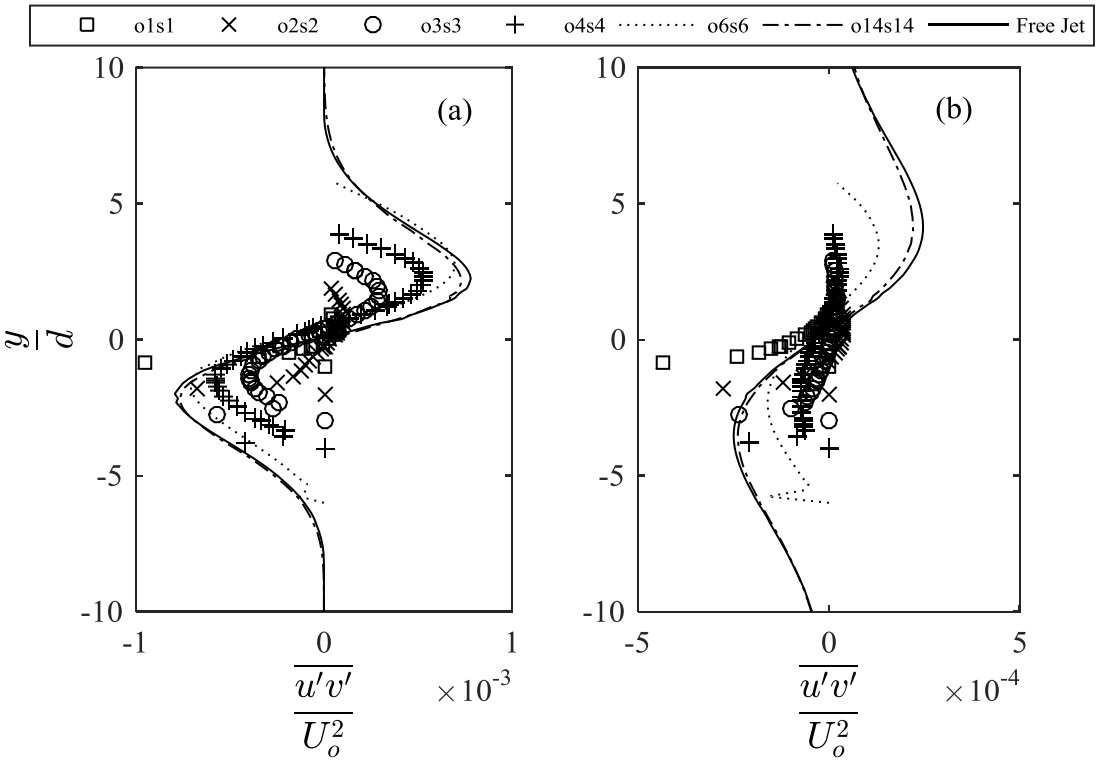

Fig. 2.16. Turbulent shear stress profiles for symmetric confinement at (a) $x/d = 30$, (b) $x/d = 50$.

Turbulent normal and shear stresses profiles in the horizontal plane through the jet axis are not significantly impacted except for the extreme case of symmetric confinement (o1s1), where the profile is distinctively narrower than the free jet. In the case of bed

confinement, both turbulent normal and shear stresses are inhibited because of the boundary layer as the jet moves toward the bed. For water surface confinement cases, turbulent normal stress are enhanced whereas the turbulent shear stress are inhibited as the jet moves toward the water surface.

2.5 Summary and Conclusions

Effect of confinement on the dilution/entrainment and mixing properties of circular turbulent jets in shallow water flow were numerically investigated in this study. Results reveal that the confinement have profound impact on the mixing and dilution characteristics of a jet in shallow water. In this study, entrainment suppression at the confining surface(s) and resulting lower decay of velocity are identified as the main causes of the modified jet behavior. Dilution/entrainment is restricted in a confined jet compared to a free jet and is more influenced by the channel bed than the water surface confinement. As a result, the maximum velocity decay at a lower rate than the free jet and the velocity profile becomes more uniform in the confined zone. The confinement does not affect the decay of the maximum velocity for offset/submergence ratio of 6 and higher. The jet attaches to the water surface for cases where the submergence depth is less than the offset depth, and it attaches to the bed for all other cases of confinement.

Turbulent shear stress is correlated with the velocity profiles. As the velocity become more uniform the turbulent shear stress reduces and vice versa. The turbulent normal stress is affected by the interaction of the jet with the bed and water surface. As soon as the jet boundary reaches the water surface the maximum value for the turbulent normal stress start to shift toward the water surface. In addition, the presence of the water

surface enhances the turbulent normal stress. The enhanced turbulent normal stress propagates downward from the water surface. The presence of the channel bed suppresses the turbulent normal stress and the effect propagates upward. In all cases, the turbulent stresses respond to the changes in the velocity profiles.

Mixing/growth properties of a jet is greatly influenced by the confinement. Usually, mixing in the horizontal plane of a confined jet is less than that of a free jet. In the vertical plane, mixing characteristics in the upper portion differ significantly from the lower portion of the jet. Mixing is enhanced (velocity profiles become more uniform) in the upper portion for symmetric and water surface confinement cases. However, for bed confinement cases the mixing is low in the upper portion of the jet. Mixing in the lower portion of the vertical plane is enhanced for all the cases of confinements. The results show that the pollutant may concentrate near the bed or surface depending on the submergence/offset ratio, which may have profound impact on the ecological system.

2.6 References

Albertson, M. L., Dai, Y. B., Jensen, R. A., & Rouse, H. (1950). "Diffusion of submerged jets." *Transactions of the American Society of Civil Engineers*, *115*(1), 639-664.

Aziz, T, Raiford, J., & Khan, A.-A. (2008). "Numerical simulation of turbulent jets." *Engineering Applications of Computational Fluid Dynamics, 2(2),* 234-243.

Bhuiyan, F., Habibzadeh, A., Rajaratnam, N., & Zhu, D. Z. (2011). "Reattached turbulent submerged offset jets on rough beds with shallow tailwater." *Journal of Hydraulic Engineering*, *137*(12), 1636-1648.

Coates, A. D. (1976). *The numerical and experimental studies on the dynamics of fluids*. PhD Thesis, Heriot-Watt University, U.K.

Dracos, T., Giger, M., & Jirka, G. H. (1992). "Plane turbulent jets in a bounded fluid layer." *Journal of Fluid Mechanics*, 241, 587-614.

Ead, S. A., & Rajaratnam, N. (2002). "Plane turbulent wall jets in shallow tailwater." *Journal of engineering mechanics*, *128*(2), 143-155.

Faghani, E., Saemi, S. D., Maddahian, R., & Farhanieh, B. (2011). "On the effect of inflow conditions in simulation of a turbulent round jet." *Archive of Applied Mechanics*, *81*(10), 1439-1453.

Foss, John F., and James Beverly Jones. "Secondary flow effects in a bounded rectangular jet." *Journal of Basic Engineering* 90.2 (1968): 241-248.

Frick, W. E., Roberts, P. J. W., Davis, L. R., Keyes, J., Baumgartner, D. J., and George, K. P. (2000). "Dilution Models for Effluent Discharges." *4th Ed. Visual Plumes.* U.S. Environmental Protection Agency, Environmental Research Division, NERL, Standards and Applied Science Division, Office of Science and Technology, Athens, Ga.

Ghahremanian, S., & Moshfegh, B. (2014). "Evaluation of RANS models in predicting low Reynolds, free, turbulent round jet." *Journal of Fluids Engineering*, 136(1), 011201.

Giger, M., Dracos, T., & Jirka, G. H. (1991). "Entrainment and mixing in plane turbulent jets in shallow water." *Journal of hydraulic research*, *29*(5), 615-642.

Hinze, J. O., & Zijnen, B. V. D. H. (1949). "Transfer of heart and matter in the turbulent mixing zone of an axially symmetrical jet." *Applied Scientific Research, 1(1),* 435-461.

Hussein, H. J., Capp, S. P., & George, W. K. (1994). "Velocity measurements in a high-Reynolds-number, momentum-conserving, axisymmetric, turbulent jet." *Journal of Fluid Mechanics, 258*, 31-75.

Islam, M. R., & Zhu, D. Z. (2011). "A numerical study of confined wall jets in a shallow basin." *Journal of Hydraulic Research*, 49(5), 595-600.

Johnston, A. J. (1985). "Aspects of buoyant and non-buoyant jets entering shallow tailwaters." In *Preprinted Proceedings: 21st Congress, International Association For Hydraulic Research, Melbourne, 19-23 August 1985. Volume 2. Theme B(Part 1): Fundamentals And Computation Of 2-D And 3-D Flows* (pp. 149-155).

Johnston, A. J., & Halliwell, A. R. (1986, December). "Jet Behaviour In Shallow Receiving Water." *In ICE Proceedings* (Vol. 81, No. 4, pp. 549-568).

Lemanov, V. V., Terekhov, V. I., Sharov, K. A., & Shumeiko, A. A. (2013). "An experimental study of submerged jets at low Reynolds numbers." *Technical Physics Letters*, 39(5), 421-423.

Mistry, D., & Dawson, J. R. (2014). "Experimental investigation of entrainment processes of a turbulent jet." *Bulletin of the American Physical Society*, 59.

Nash, J. Eamonn, and Jonh V. Sutcliffe. "River flow forecasting through conceptual models part I—A discussion of principles." *Journal of hydrology* 10.3 (1970): 282-290.

Pope, S. B. (1978). "An explanation of the turbulent round-jet/plane-jet anomaly." *AIAA journal*, *16*(3), 279-281.

Raiford, J. P., & Khan, A. A. (2009). "Investigation of circular jets in shallow water." *Journal of Hydraulic Research, 47*(5), 611-618.

Rajaratnam, N., & Khan, A. A. (1992). "Intersecting circular turbulent jets." *Journal of Hydraulic Research*, *30*(3), 373-387.

Shinneeb, A. M., Balachandar, R., & Bugg, J. D. (2011). "Confinement effects in shallow-water jets." *Journal of Hydraulic Engineering*, *137*(3), 300-314.

Wygnanski, I., and Fiedler, H., (1969). "Some measurements in the self-preserving jet." *Journal of Fluid Mechanics, 38*(03), 577-612.

Xu, G., & Antonia, R. (2002). "Effect of different initial conditions on a turbulent round free jet." *Experiments in Fluids*, *33*(5), 677-683.

CHAPTER 3*

FREE FALL OF WATER DROPS IN LABORATORY RAINFALL SIMULATIONS

3.1 Introduction

The goal of this research is to explore various fields of fluid mechanics through experimental and numerical investigations. The field of interests include raindrop dynamics, round turbulent jets in shallow water, and hydraulics characteristics of sheet flow.

3.2 Raindrop dynamics

In this section, the aim is to provide a guidance for adequate laboratory simulations of natural rainfall. Given its meteorological and hydrological significance, laboratory investigations of rainfall related research are in great demand. Applications such as the radar retrieval of rainfall rate (e.g. Cifelli and Chandrasekar, 2010) and soil erosion induced by raindrop impact (e.g. Kinnell, 2005) are just two of the many examples that necessitate rainfall microphysical investigations (see Testik and Barros, 2007).

There are two main types of laboratory experimental setups for studying raindrop morphodynamics: rain towers and vertical wind tunnels (see Testik and Barros, 2007). This study is related to the laboratory rain towers. Also referred to as fall shaft/column, rain

* This chapter is published in the Journal of Atmospheric Research as a technical paper.
Chowdhury, M. N., Testik, F. Y., Hornack, M. C., & Khan, A. A. (2016). Free fall of water drops in laboratory rainfall simulations. *Atmospheric Research*, *168*, 158-168.

towers are comprised of a drop generator and an adequate fall distance from the drop generator to the observation point. Rain towers have been used to study various rainfall microphysical processes such as raindrop shape, oscillations, terminal velocity, and collisions (e.g. Gunn and Kinzer, 1949; Wang and Pruppacher, 1977; Low and List, 1982a,b; Andsager et al., 1999; Testik, 2009; Testik et al., 2011). Vertical wind tunnels are used to keep the drops aloft at the observation area; hence, only raindrop microphysics at terminal velocities can be examined. Vertical wind tunnels have been used to study various raindrop characteristics, including raindrop shape, internal circulation, and drop growth through coalescence (e.g. Pruppacher and Beard, 1970; Vohl et al., 1999; Szakáll et al., 2009; Müller et al., 2013). It is important to point that rainfall towers are the means to study problems such as soil erosion and conveyance due to rainfall, and rainfall-flow interactions in sheet flows.

When the gravitational force balances both the drag and the small buoyancy forces acting on a raindrop, the raindrop falls at somewhat constant, or terminal, velocity. Terminal velocity is a function of the volume equivalent diameter of a raindrop. Several formulae have been proposed for describing terminal velocity of raindrops (see Appendix-A of Testik and Barros, 2007). Eq. (3.1) shows one such formula proposed by Atlas et al. (1973) that is applicable to 0.6-5.8 mm drops,

$$U_t = 965 - 1030e^{-(6d)} \tag{3.1}$$

where U_t is the terminal velocity of the raindrop in cm/s and d is the equivalent diameter in cm.

Raindrops may have an equilibrium shape or a shape that is characterized by oscillations (e.g. Pruppacher and Beard, 1970; Beard et al., 1991; Testik et al., 2006; Szakáll et al., 2009). Surface tension, hydrostatic pressure, aerodynamic pressure, internal circulation, and electric stress are the factors that most affect the raindrop shape (Beard and Chuang, 1987). Surface tension dominates over other factors for raindrops of diameter (equivalent diameter of a sphere having same volume as the raindrop) less than 1mm, keeping such raindrops approximately spherical. As the raindrop size increases, raindrops exhibit oblate spheroidal equilibrium shapes with flattened lower surfaces (see Testik and Barros, 2007 for detailed descriptions).

Several different models are available for describing the equilibrium shape of raindrops (e.g. Pruppacher and Pitter, 1971; Green, 1975; Beard and Chuang, 1987). The theoretical model of Beard and Chuang (1987) has been widely used for predicting the equilibrium raindrop shape. Beard and Chuang (1987) provided a cosine series fit (see Eq. 3.2) with appropriate coefficients to conveniently reproduce the predicted shapes by the model.

$$r = a[1+\sum_{\eta=0}^{10} c_\eta \cos(\eta\theta)] \tag{3.2}$$

where r is the radial position of the raindrop boundary and θ is the polar angle. The symbol η refers to the integers varying from 0 to 10, and C_η refers to the coeffcients.

The equilibrium shape of raindrops is typically described by their axis ratio (α), which is defined as the ratio of the maximum vertical and horizontal chords (Beard et al., 2010). This ratio decreases with increasing drop size as shown in Eq. (3.3), which is a

polynomial fit to the Beard and Chuang's (1987) model predictions (Andsager et al., 1999). Here, $\bar{\alpha}$ is the average axis ratio and d is the volume equivalent diameter in cm.

$$\bar{\alpha} = 1.0048 + 0.0057d - 2.628d^2 + 3.682d^3 - 1.677d^4 \tag{3.3}$$

Various agents may induce raindrop oscillations in natural rainfall as vortex shedding (Beard and Kubesh, 1991; Beard et al., 2010), raindrop collisions (Johnson and Beard, 1984), and wind shear and turbulence (Tokay and Beard, 1996). Small-amplitude raindrop oscillations are typically analyzed by spherical harmonic perturbations (Rayleigh, 1879). The oscillation frequencies of spherical harmonic perturbations are given by Eq. (3.4).

$$f_n = \left[\frac{2n(n-1)(n+2)\sigma}{\pi^2 \rho d^3} \right]^{\frac{1}{2}} \tag{3.4}$$

Here, n is the order, d is the equivalent volume diameter of the raindrop, σ and ρ are the surface tension and the density of water, respectively. Each oscillation frequency is associated with $m = n+1$ degenerate modes. Each combination of order and modes (n, m) has unique spatial orientation (Beard and Kubesh, 1991). Raindrop oscillations are generally considered to be governed by the three oscillation modes of the fundamental harmonic; i.e, (2, 0), (2, 1), (2, 2), which are referred to as the axisymmetric, transverse, and horizontal modes, respectively (Testik et al., 2006; Testik and Barros, 2007; Szakáll et al., 2010). The geometrical characteristics of these oscillation modes are illustrated in Fig.

3.1. Note that Testik et al. (2006) has shown the presence of multi-mode raindrop oscillations in natural rainfall events using high-speed imaging. Furthermore, it is important to note that raindrops that are larger than approximately 1 mm in diameter have pronounced oblate spheroidal shapes. Oscillation frequencies of such distorted drops differ from the oscillation frequencies of spherical drops that are calculated by Rayleigh's formulation (see Feng and Beard, 1991, and Müller et al. 2013).

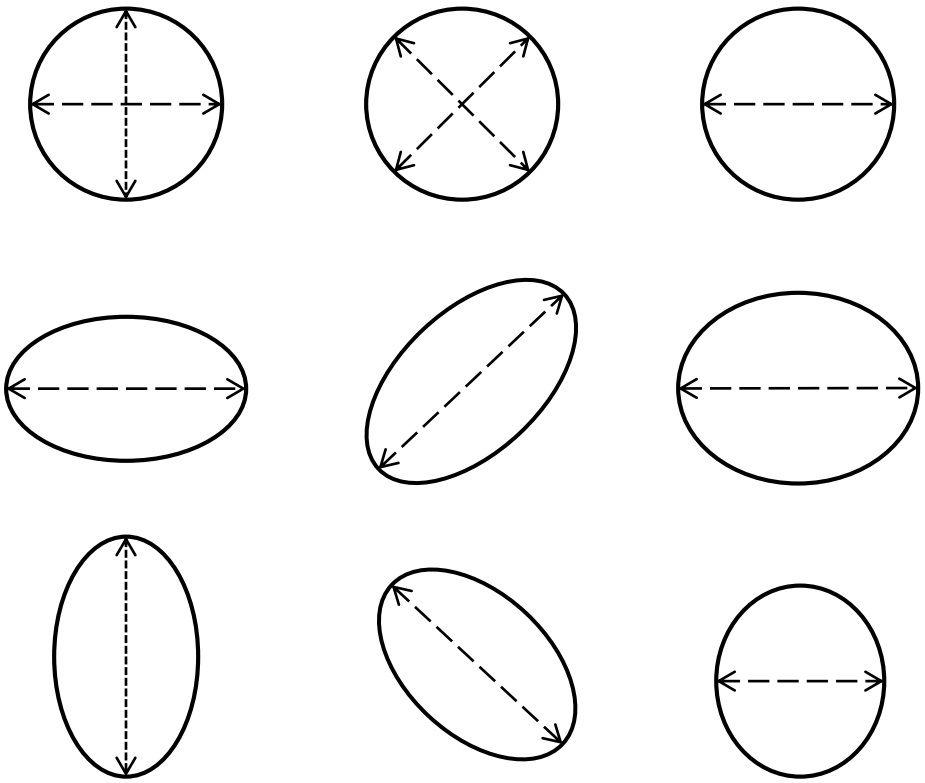

Fig. 3.1: Schematic of the three oscillation modes of the fundamental harmonic: Arrows indicate oscillation directions: (a) axisymmetric, (b) transverse, and (c) horizontal oscillation modes at different oscillation phases.

Laboratory drops typically undergo source-induced oscillations at their initial stages of fall. Viscous dissipation gradually damps out these oscillations and, after some fall distance, drops achieve equilibrium shapes. As the shape of the drop approaches equilibrium, the amplitude of the drop axis ratio (A) decays exponentially as given by Eq.(3.5) (Beard et al., 1991; Testik and Barros, 2007).

$$A = A_0 e^{-t/\tau} \tag{3.5}$$

Here, A_0 is the maximum amplitude of the oscillations, t is the elapsed time from the start of oscillations, and τ is the time constant, which is given by Eq.(3.6) as

$$\tau = \frac{d^2}{4(n-1)(2n+1)\upsilon} \tag{3.6}$$

where ν is the kinematic viscosity of the drop fluid (Pruppacher and Klett, 1997). Time constant, τ, provides an indication of the oscillation decay due to viscous damping and is a function of the oscillation order, n. As Eq. (3.6) indicates, oscillation modes of the fundamental harmonic ($n = 2$) are expected to prevail longer than the other modes.

While oscillating, drops also accelerate to achieve terminal velocities. The time required for a drop to reach β fraction of the terminal velocity t_β which was formulated by Wang and Pruppacher (1977), is expressed as:

$$t_\beta = -\tau \ln(1-\beta) \tag{3.7}$$

Andsager et al. (1999) noted that, based on the variation of drop axis ratio in their drop tower experiments, the source effects diminish within the first few meters of drop fall. Nevertheless, more specific quantitative information on the required fall distance for drops

to achieve equilibrium shape is necessary for developing adequate rainfall experiments in the laboratory rain towers. Thus, the objective of this study is to acquire comprehensive information regarding the source effects on the evolution of drops to equilibrium.

3.3 Experimental setup

Water drops from twelve stations at different elevations (h) were generated in an enclosed stairwell, which served as the laboratory space with a controlled-environment. This space was isolated from the building through doors, which were shut during the experiments. The air in the stairwells was stagnant, and the temperature was nearly constant (approximately 22 °C) during the experiments. A schematic of the experimental setup is shown Fig. 3.2. Drops of distilled water were generated using a needle attached to a constant-head tank through a tube valve system to control and regulate generated drops. An extended arm was used to support and position the needle. After forming a sessile drop at the needle tip, generated drops dripped from the needle under the action of their own weight without any additional external forcing agent. Three different sizes of needles were used to generate three different sizes of water drops. Average drop sizes produced by the needles were 2.6, 3.7, and 5.1 mm volume equivalent diameters with standard deviations of 0.16, 0.19, and 0.19mm, respectively. The results presented in this manuscript are based upon the analysis of total of 360 drops (10 drops per station per each drop size × 12 stations × 3 drop sizes).

A high-speed camera (Fastec-Troubleshooter) was used to capture the sequence of frames with a 1000 frames per second rate as the drops passed through the camera view

frame. The captured images were 640 pixels (92 mm) in the horizontal direction and 480 pixels (69 mm) in the vertical direction. Generated drops fell within a circle of 7 cm diameter at the focal plane, which ensured the image quality and measurement accuracy as it is discussed below. More than 1000 frames have been used for the analysis of each drop size. A halogen light bulb was used as the light source to illuminate the drop from behind (see Testik et al., 2006; Testik, 2009; Testik et al., 2011).

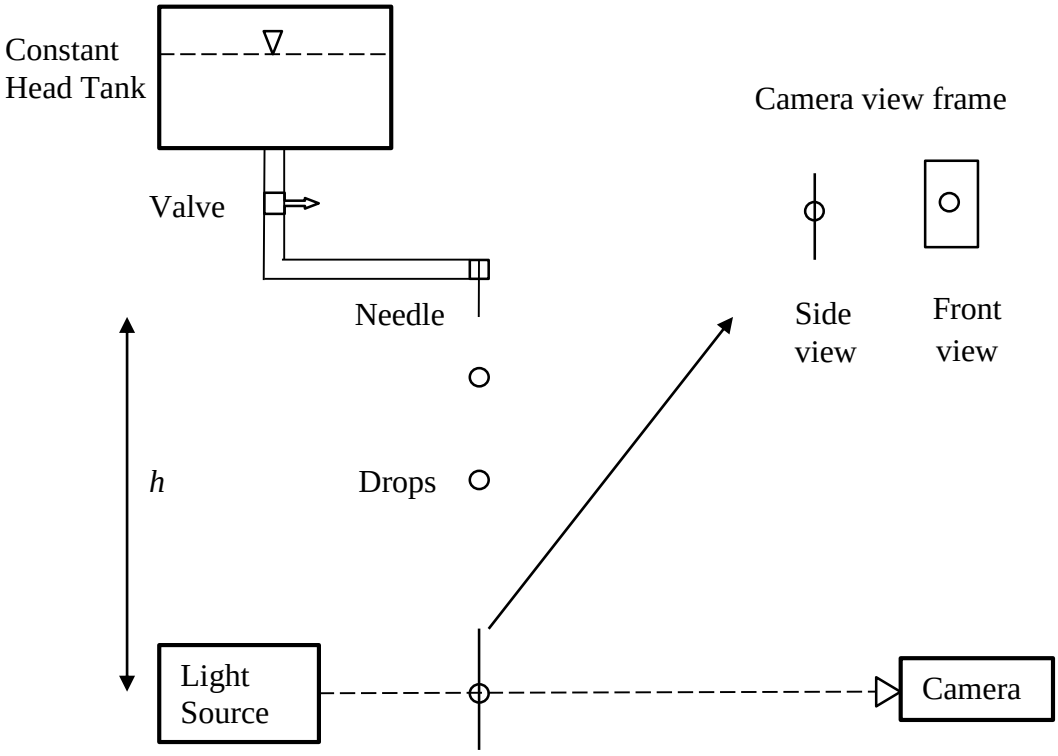

Fig. 3.2 Schematic of the experimental setup.

Typical drop images obtained using this technique are shown in Fig. 3.3. We used fixed thresholding to convert the gray-scale raw images to binary images, leading to the detection of the drop boundaries. Since only the images of drops within a short distance from the focal plane were captured, the drop images were sharp and fixed thresholding was sufficient to accurately detect the drop boundaries.

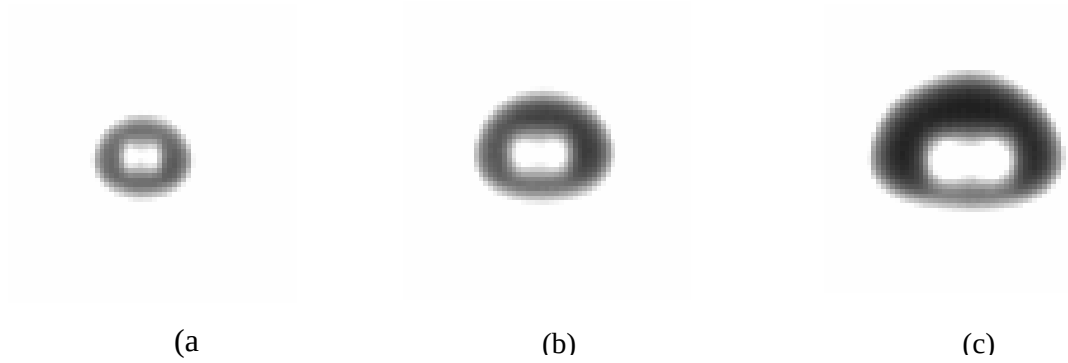

(a (b) (c)

Fig. 3.3 Typical backlit drop images for all three drop sizes studied.

Fig. 3.4 shows a representative raw image (Fig. 3.4a), the corresponding processed image after fixed thresholding (Fig. 3.4b), and the gray level histogram plot of the raw drop image (Fig. 3.4c). As can be seen in Fig. 3.4c, the gray level intensity histogram plots of raw images showed a distinct peak that corresponds to a steep gradient in gray level intensity at the drop boundary. Such a distinct peak indicates that a fixed threshold value can be selected for accurate processing of raw drop images to detect drop boundaries. The suitability of the selected threshold value (which is 235 for the gray level intensity range of 0–black to 255–white) was verified in three ways: (i) through experiments with the

spherical ball lenses that are discussed later in this section, (ii) through comparing the detected and visual boundaries of water drops, and (iii) through a sensitivity analysis for the axis ratio measurements with the selected threshold value. The experiments with the spherical lenses showed that the measured diameter values of the lenses were almost identical to the actual diameter values. Similarly, the experiments with water drops showed that the detected and visual boundaries of water drops were almost identical. These visual verifications for the drop boundaries were conducted by superimposing the raw drop images and the detected drop boundaries. The sensitivity analysis with different threshold values that are ±10 gray level intensities around the selected threshold value of 235 showed that measured axis ratio values vary only up to 6% from those that are obtained using the selected threshold value. Consequently, it was concluded that the selected fixed threshold value is suitable to extract accurate drop shape information. Note that the setup including the camera and background light remained unaltered for the entire experiments, ensuring consistency for the image processing purposes.

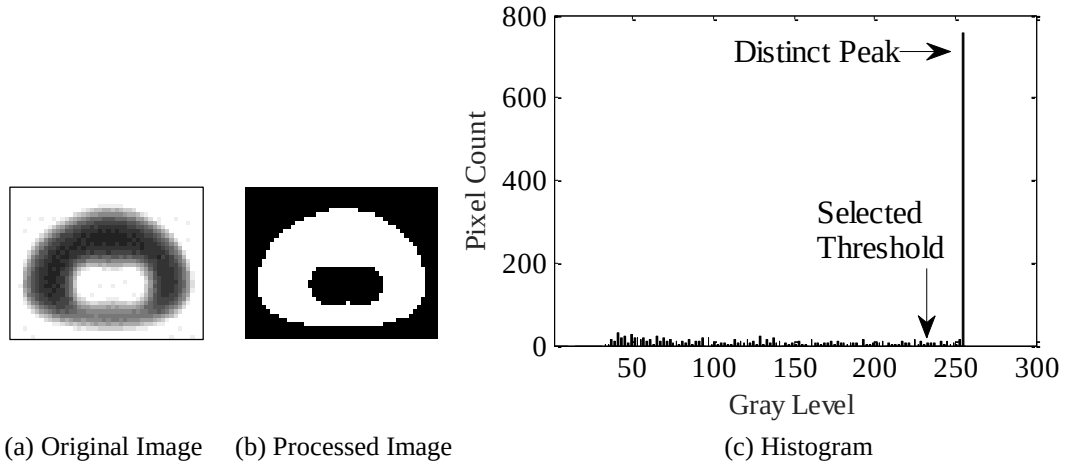

Fig. 3.4 Comparison of a typical (a) raw gray-scale image, (b) the corresponding processed binary image, and (c) the corresponding histogram of the raw gray-scale image.

The conversion to binary images was followed by an analysis to extract the necessary drop information on the shape characteristics and the fall velocity. Drop fall velocities were calculated by the displacement of the drop's centroid between two consecutive frames. For non-equilibrium shaped drops, the centroid location obtained from the captured drop images may shift, resulting in fall velocity calculation errors. The fall velocity of a given drop was calculated multiple times using the sequential high-speed images as the drop passes through the short vertical distance within the camera view frame. The differences between the calculated fall velocities for a given drop at consecutive instances were insignificant (with standard deviation values less than 0.5%, 0.9%, and 3.2% of the respective terminal velocities for 2.6 mm, 3.7 mm, and 5.1 mm drops at a given station). This indicates that fall velocity calculation errors were unimportant. Furthermore,

the calculated fall velocity values for a given drop at consecutive instances were averaged to minimize these errors. Volume equivalent drop diameters were obtained from the captured drop images by calculating the volume of the drop in each image frame with the assumption of rotational symmetry of the drops. Using sequential high-speed images of the same drop at a given measurement station, the frame-averaged drop diameters were calculated by averaging the volume equivalent diameters obtained from each of the frames. The frame-averaged volume equivalent diameters were used in calculations for the drop shape evolution analysis that is presented in Section 3.

To assess the impact of rotational symmetry assumption in the measurement accuracy, the following two different comparisons were made. For the first comparison, the frame-averaged drop diameter values were compared with the average drop diameter for a given needle, which was calculated by averaging the frame-averaged diameters of all the drops captured at a given measurement station. This comparison showed that frame-averaged drop diameter values were very close to the average drop diameter values (i.e. standard deviations less than 0.2 mm). For the second comparison, the average drop diameters at different measurement stations for a particular needle were compared. This comparison showed that the difference between the average drop diameters of equilibrium-shaped drops and oscillating drops was marginal (less than 3%). Based upon these comparisons, it was concluded that measurement errors for the volume equivalent diameter due to rotational symmetry assumption was insignificant for our purposes.

To estimate the measurement error bounds, tests with spherical ball lenses (refractive index of 1.46 and sphericity of ±2.5 μm) of 3 and 5 mm diameters were

performed at different distances from the focal plane and the test images were processed using the fixed thresholding technique. For spherical lenses located at 3 cm towards the camera from the focal plane, the measurement error in volume equivalent diameter was less than 10%. For spherical lenses located at 5 cm towards the light source from the focal plane, this error was less than 5%. Fig. 3.5 shows the captured images for both of these cases for the 5 mm and 3 mm spherical lenses. For improved measurement accuracy, an operator visually selected the drop images that corresponded more to Fig. 3.5b (than Fig. 3.5a) for analysis. Consequently, the measurement error of volume equivalent diameter was confined at less than 5%. To provide an insight on the measurement errors for a given quantity, the standard deviations of the measured quantities are shown in the relevant figures provided later in the manuscript.

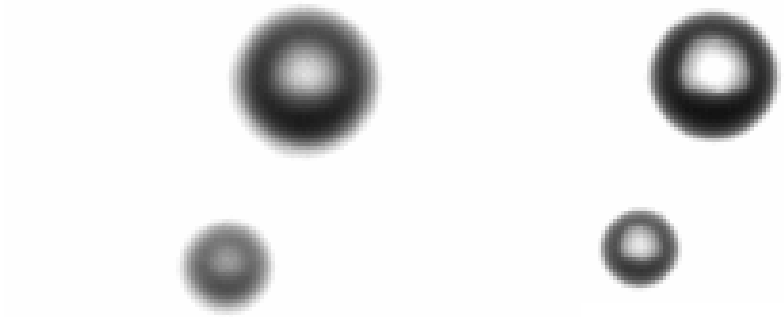

a) b)

Fig. 3.5 Images of calibrated spheres located at (a) 3 cm towards the camera from the focal plane and (b) 5 cm towards the light source from the focal plane.

3.4 Results and Discussion

Rainfall simulations in the laboratory require sufficient fall distances for the generated drops to achieve equilibrium raindrop shape and terminal velocity so that generated drops mimic the actual raindrops. Based upon our experimental observations, three distinct fall zones (hereafter, referred to as Zone I, Zone II, and Zone III) were identified for the free-fall of water drops. A schematic of different fall zones along with representative drop images is shown in Fig. 3.6. In Zone I, drops continuously adjusted shape due to source-induced oscillations, which were gradually dampened by viscous dissipation. By the end of Zone I, drops achieved an almost constant shape, referred to as the equilibrium shape. In Zone II, equilibrium-shaped drops had sub-terminal velocities and accelerated to achieve terminal velocities by the end of this zone. In Zone III, equilibrium-shaped drops fell at terminal velocities.

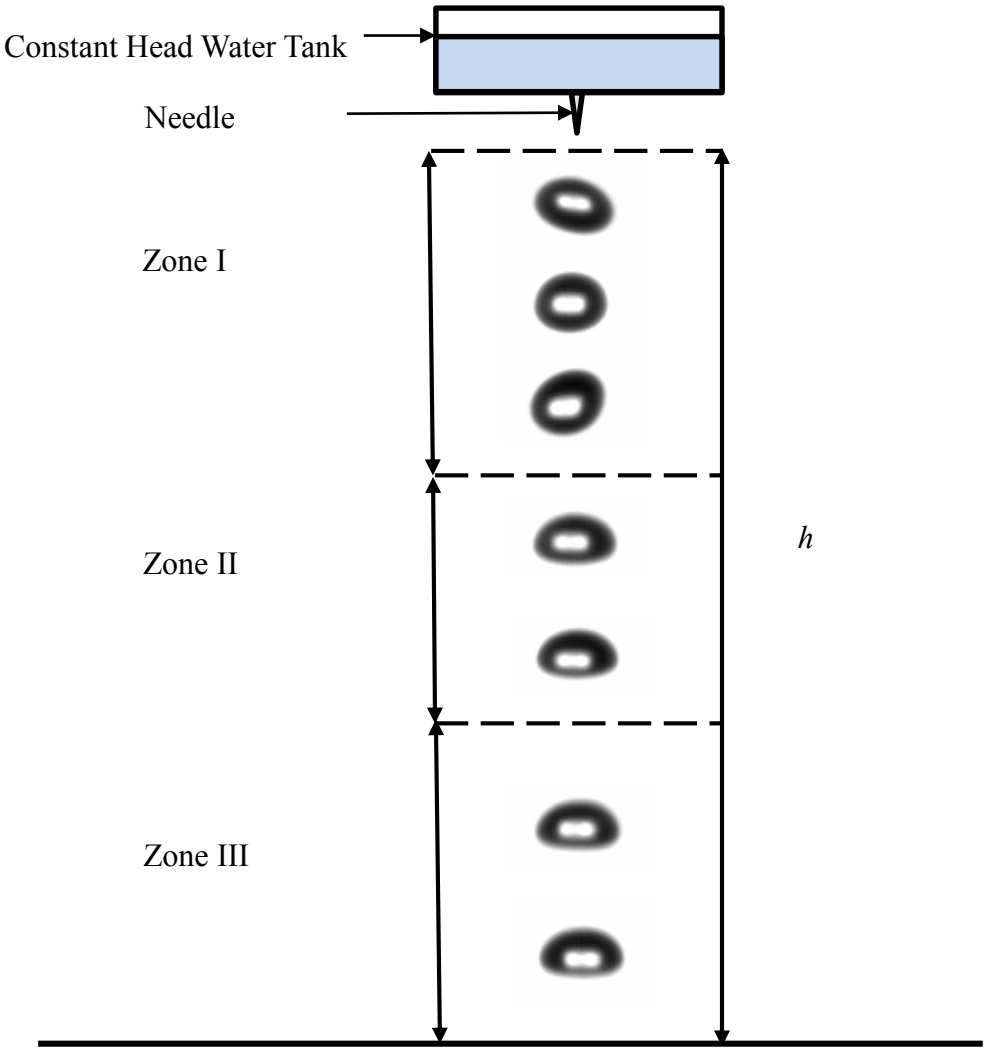

Fig. 3.6 Different fall zones for free-falling water drops. Typical drop images at different times and elevations were augmented to illustrate typical drop shapes at the relevant fall zone.

We used various criteria, based upon transient and equilibrium drop shape parameters and drop fall velocity, to determine the extent of each fall zone. Transient shape parameters involved drop axis ratio ($\overline{\alpha} = a_v / a_h$ – the ratio of the longest vertical chord and the longest horizontal chord), chord ratio (ratio of the two orthogonal chords where one

chord (c_l) is the longest chord in the drop and the other one (c_s) is the longest chord that is orthogonal to c_l ; $c = c_s / c_l$), canting angle (θ , the angle between the longest chord and the horizontal axis), and the drop averaged standard deviation of the maximum horizontal and vertical chord lengths at a given station for drops generated from a specific needle (ε) . In calculating ε , standard deviations of the maximum horizontal and vertical chord lengths for each of the drops were first obtained using sequential high-speed images. The calculated standard deviations were then averaged for all of the drops generated from a given needle at a particular station. An illustrative schematic for the shape parameters is provided in Fig. 3.7.

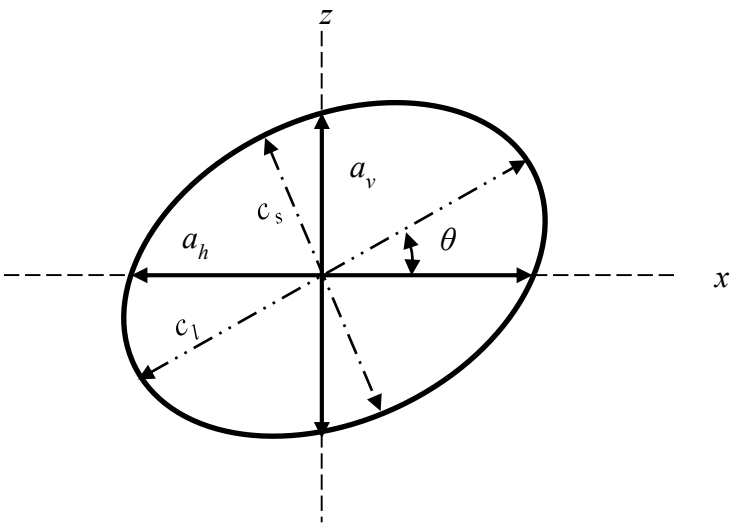

Fig. 3.7 An illustrative schematic of the drop shape parameter definitions

Observed equilibrium drop shapes were compared with the equilibrium raindrop shapes using Beard and Chuang's (1987) theoretical analysis. Furthermore, drop fall

velocities at a given fall distance were compared using the predicted terminal velocities of Eq. (3.1) developed by Atlas et al. (1973). The following subsections describe our quantitative efforts to delineate these fall zones based upon the transient shape (for the extent of Zone I), the equilibrium shape (for the onset of Zone II), and the terminal velocity (for the onset of Zone III) criteria.

3.4.1 Drop Shape Evolution

Generated drops were expected to exhibit multimode oscillations that are governed by the axisymmetric, transverse, and horizontal oscillation modes of the fundamental harmonic (see Fig. 3.1). To determine the presence/absence of large-amplitude drop oscillations generated by detachment from the source (hence, the extent of Zone I), the evolution of the aforementioned shape parameters with fall distance was analyzed, the results of which are presented in Fig. 3.8–Fig. 3.11. Moreover, observed shapes of generated drops were compared to the equilibrium raindrop shapes as predicted by Beard and Chuang (1987) to determine the fall distance required for the generated drops to achieve equilibrium shapes (see Fig. 3.12, later). In all of these figures (Fig. 3.8–Fig. 3.12, and later Fig. 3.14), each presented data point corresponds to the averaged data for all the drops with a given size and all the images of a given drop at a particular fall distance (i.e. measurement station). Vertical bars in these figures represent the standard deviation of the corresponding data and provide an indication of the measurement errors.

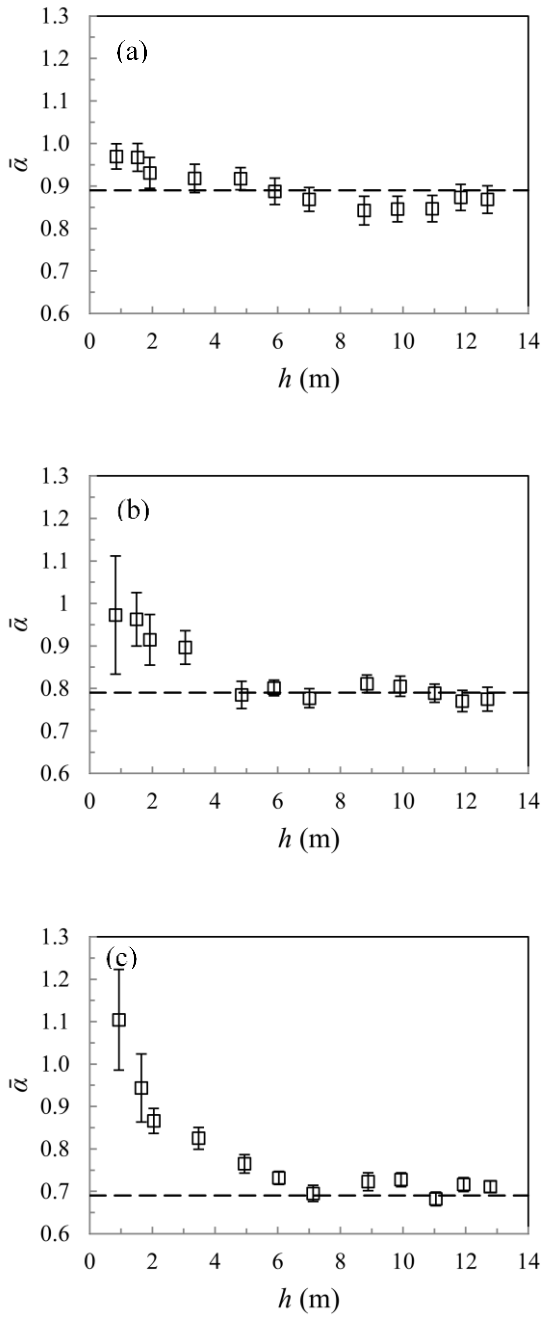

Fig. 3.8 Evolution of the averaged axis ratio (symbols) of (a) 2.6 mm (b) 3.7 mm and (c) 5.1 mm drop. The vertical bars indicate the standard deviation of measured data at a given fall distance. Dashed lines indicate the predicted equilibrium axis ratio values as obtained from Eq. (3.3).

Our first criterion involved the drop axis ratio evolution with fall distance. Fig. 3.8 shows the axis ratio evolution for 2.6, 3.7, and 5.1 mm diameter drops with fall distance (*h*). It can be seen in this figure that, after some fall distance, generated drops approached an approximately constant drop axis ratio value with small standard deviations for each of the drop sizes. These constant axis ratio values were approximately 0.88, 0.79, and 0.71 for 2.6, 3.7, and 5.1 mm diameter drops, respectively. These constant axis ratio values were in good agreement with equilibrium axis ratio values of 0.89, 0.79, and 0.69 for 2.6, 3.7, and 5.1 mm drops, respectively as predicted by Eq. (3.3). Generated drops reached to within 5% of the predicted equilibrium axis ratio values after falling freely 3.4 m for 2.6 mm drops, 4.8m for 3.7 mm drops, and 6 m for 5.1 mm drops. These results are consistent with the viscous decay of drop oscillations, in which the time required for the oscillation decay is directly proportional to the drop size as shown by Eq. (3.6). Moreover, the drops generated in our experiments achieved fall velocities that are approximately 82% for d = 2.6 mm, 89% for d = 3.7 mm, and 90% for d = 5.1 mm of terminal velocity by the onset of Zone II. Eqs. (3.5) and (3.7) predict that, by this time, the amplitudes of the drop oscillations reduce to 18% for d = 2.6 mm, 11% for d = 3.7 mm, and 10% for d=5.1 mm of the associated maximum oscillation amplitudes $\left(A_o\right)$ due to viscous damping. These predictions are consistent with our observations of equilibrium-shaped drops by the onset of Zone II. It is important to mention that 18% of A_o for 2.6 mm drops does not correspond to notable oscillations as smaller drops have smaller A_o values.

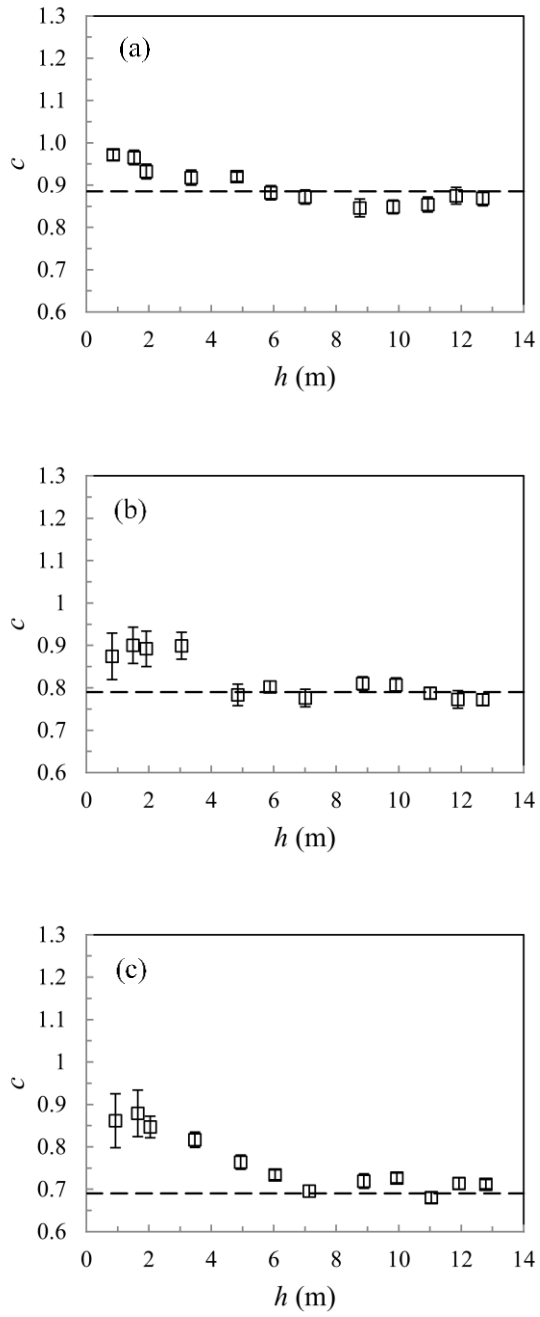

Fig. 3.9 Evolution of the averaged chord ratio values (symbols) for (a) 2.6 mm, (b) 3.7 mm, (c) 5.1 mm drops. Vertical bars indicate the standard deviation of measured data at a given fall distance. Dashed lines indicate the predicted equilibrium axis ratio values as obtained from Eq. (3.3).

Though constant axis ratio and small standard deviation values observed in Fig. 3.8 imply that all modes of source-induced drop oscillations have died out, the drop canting may be present. To investigate drop canting, a second criterion that involved drop chord ratio was used. The chord ratio evolution with fall distance for all the drop sizes studied is provided in Fig. 3.9. These graphs show that the chord ratio values achieve constant values with small standard deviations, which are almost identical to the observed equilibrium axis ratio values. In virtue of the definition of the axis (ratio of the maximum vertical and horizontal chord lengths) and chord ratios $c = c_s / c_l$, identical axis and chord ratio values indicate the absence of drop canting. Chord ratio values of the generated drops were within 5% of the predicted equilibrium axis ratio values by 3.4, 4.8, and 6 m fall distances for 2.6, 3.7, and 5.1 mm drops, respectively. This observation indicates the absence of drop canting beyond the respective fall distance. These graphs in Fig. 3.9 should not be interpreted as an indication of the presence of canted drops until attainment of the aforementioned respective fall distance. Because the deviations of the chord ratio and axis ratio values may be related to the drop oscillations.

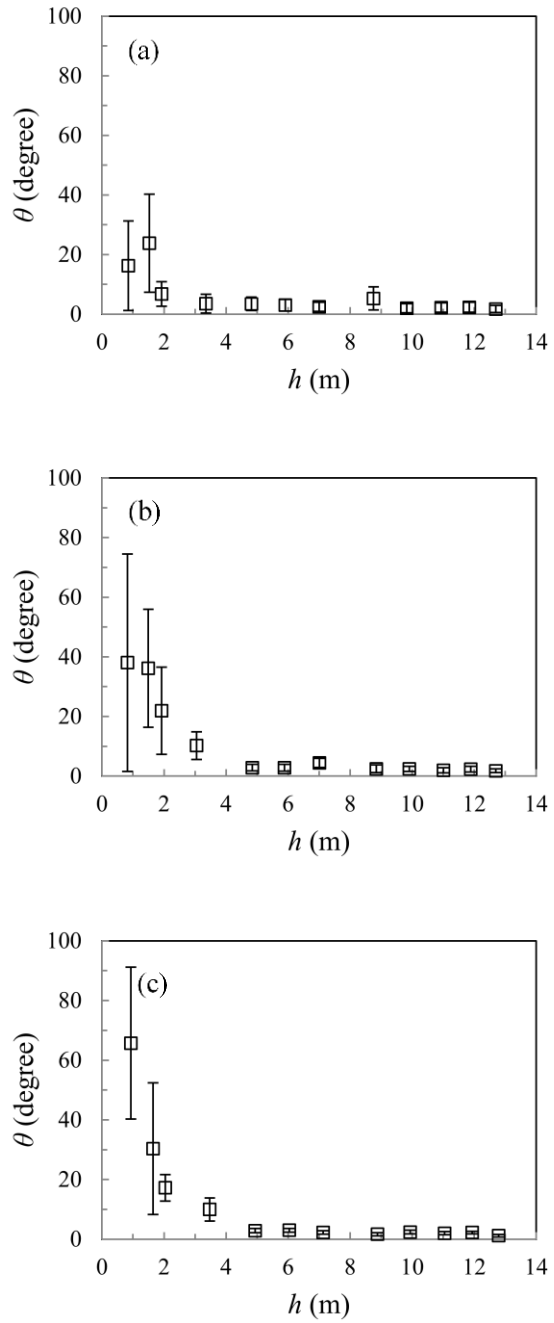

Fig. 3.10 Evolution of averaged orientation angle values (symbols) of (a) 2.6 mm, (b) 3.7 mm, and (c) 5.1 mm drops. Vertical bars indicate the standard deviation of measured data at a given fall distance.

To confirm the absence of drop canting, a third criterion that involved the canting angle, θ, was implemented. Fig. 3.10 shows the evolution of the canting angle with fall distance for 2.6, 3.7, and 5.1 mm diameter drops. Here, high canting angles with high standard deviations observed during the initial few meters of the drop fall indicate the presence of axisymmetric and transverse oscillation modes (see Fig. 3.1). The near-source canting angle values are comparatively higher for larger drops. Because the surface tension force, which resists the distortion of the drops and favors drop sphericity, is weaker for larger drops. When the drop canting angle values reach to near 0° after some fall distance as seen in Fig. 3.10, it can be concluded that drops are not canted, and the source-induced axisymmetric and transverse oscillation modes have been dampened. The horizontal oscillation mode, however, may still be present as the expected theoretical canting angle value for this oscillation mode, the longest chord being along the horizontal axis, is 0°. Based upon Fig. 3.10, the required fall distances for near 0° canting angles were found to be 3.4 m (for 2.6 mm drops), 4.8 m (for 3.7 mm drops), and 5 m (for 5.1 mm drops). In this analysis, the maximum measurement error for the canting angle was 6°. Consequently, in determining the required fall distances for near 6° canting angle values, we used 6° as a threshold value.

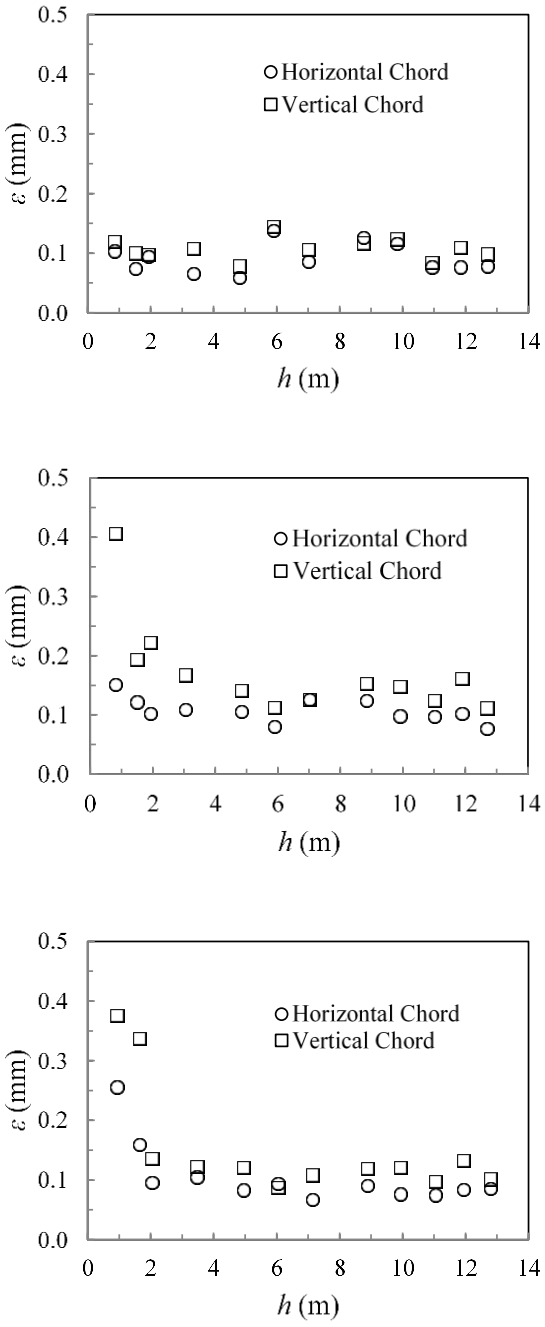

Fig. 3.11 Comparison of averaged horizontal and vertical chord lengths with fall distance of (a) 2.6 mm, (b) 3.7 mm, and (c) 5.1 mm drops.

To determine the absence of horizontal oscillation mode, our criterion involved the standard deviations (ε) of the horizontal (a_h) and vertical (a_v) chord lengths. For the presence of horizontal oscillation mode, the standard deviations of the horizontal chord length should be much larger than those of the vertical chord. Indeed, pure horizontal oscillations would dictate a theoretical value of zero for the standard deviations of the vertical chord. Note that Müller et al. (2013) identified and characterized the horizontal oscillation mode in their vertical wind tunnel observations using the area method, which uses FFT analysis of the periodic change of the calculated volume equivalent diameter. This method could not be used for our oscillation observations of falling drops as they were not sufficiently long for such an analysis. Fig. 3.11 shows the change of the standard deviations of a_h and a_v with the fall distance for all drop sizes studied. As it is apparent in this figure, the magnitudes of the standard deviations of a_h and a_v were of the same order after a few meters of fall for all generated drops, indicating the absence of the horizontal oscillation mode.

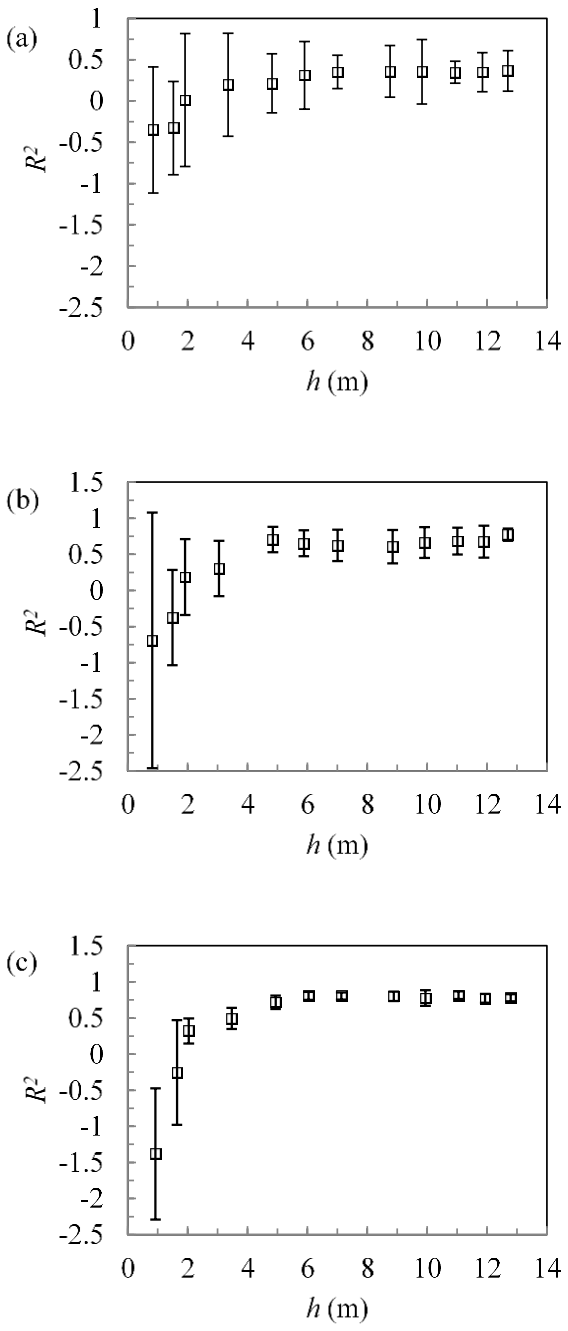

Fig. 3.12 Evolution of drop-averaged R^2 values from observed drop shape and predicted equilibrium raindrop shape comparisons with fall distance for (a) 2.6 (b) 3.7 and (c) 5.1 mm drops. Vertical error bars represents the standard deviation of the measured data at a given fall distance.

The extent of Zone I was determined from these four criteria (see Table 3-I, later). To determine the onset of Zone II, observed drop shapes were compared with the predicted equilibrium raindrop shapes by Beard and Chuang (1987). The coefficient of determination $\left(R^2\right)$ and the ratio of the root mean square error to the standard deviation of observed data (RSR) were used to analyze the correlation between the observed and predicted drop shapes during the fall. The ranges of R^2 and RSR values are from $-\infty$ to 1.0 and $+\infty$ to 0, respectively. Acceptable values of R^2 and RSR are from 0 to 1.0 and close to 0, respectively (see Moriasi et al., 2007). Beard and Chuang's equilibrium shapes were calculated using a frame-averaged volume equivalent diameter for each observed drop at a particular fall distance. The observed drop shape captured in each frame was then compared with the predicted shape. Fig. 3.12 shows the evolution of drop-averaged R^2 values from these comparisons for 2.6, 3.7, and 5.1 mm diameter drops. Here, a plateau is observed for all three drop sizes studied after some fall distance. This plateau indicates the establishment of an equilibrium drop shape and is used to determine the onset of Zone II, which coincides with the end of Zone I. The R^2 values when the generated drops established equilibrium shapes were 0.80, 0.65, and 0.35 for 5.1, 3.7, and 2.6 mm diameter drops, respectively. These values are in an acceptable range for correlation and an R^2 value of 0.35 for the 2.6 mm drops should not be interpreted as a weak correlation. The R^2 formulation incorporates normalization of the comparison between the model and observed data with the variance of the observed data [i.e. $R^2 = 1 - \left[\sum_{i=1}^{\delta} \left(O_i - f_i\right)^2 / \sum_{i=1}^{\delta} \left(O_i - \overline{O}\right)^2 \right]$, here $i - \text{index}$, $O - \text{observerd data}$, $\overline{O} - \text{mean of the observed data}$, and f model data]. In our

analysis, we used polar coordinate system (i.e. radial and polar angle coordinates) for points at the drop boundary to calculate the R^2 values. The mean value of the observed data can be considered as the radius of a circle that represents the side-view boundary (i.e. 2D shape) of a virtual spherical drop. Since 2D shapes of larger drops deviate more from a circular shape than those of smaller drops, the variance of the observed data (i.e. the term in the denominator of the R^2 relationship) is greater for larger drops. Consequently, it is reasonable to expect R^2 values of larger drops to be greater than those of smaller drops. While the smaller drops had a comparatively lower R^2 values, they had a good shape correlation. In Fig. 3.13, predicted and observed equilibrium shapes of drops with *d*=2.6 mm and 5.1 mm are compared. In these comparisons, predicted equilibrium shapes were obtained using both Beard and Chuang's (1987) theoretical model and Thurai et al.'s (2007) empirical fit to the shapes of drops that fell 80 m from their generation source of a fire hose on a bridge. In this figure, observed drop shapes were from measurements after fall distances of 11.8 m for d = 2.6 mm and 12.0 m for d = 5.1 mm. As can be seen from this figure, observed drop shapes were in good agreement with the shape predictions by both of the models, Thurai et al.'s empirical fit providing a better fit to the larger drop in (b) than Beard and Chuang's model. Here it is important to note that evolution of the drop-averaged R^2 values using Thurai et al.'s empirical fit indicate the same fall distances for the establishment of equilibrium drop shapes that were obtained using Beard and Chuang's model. Given that it is a widely used theoretical model for equilibrium raindrop shapes, we used Beard and Chuang's model in our analysis (i.e. calculations of R^2 and RSR values). In Fig. 3.13, although the R^2 values are 0.35 and 0.8 for the 2.6 mm and 5.1 mm drops,

respectively, the resemblance between the predicted and observed shape looks better for the 2.6 mm drop than the 5.1 mm drop. The RSR comparisons showed consistent results with the R^2 comparisons. The RSR values for 2.6, 3.7 and 5.1 mm drops with equilibrium shapes are 0.44, 0.55, and 0.82, respectively.

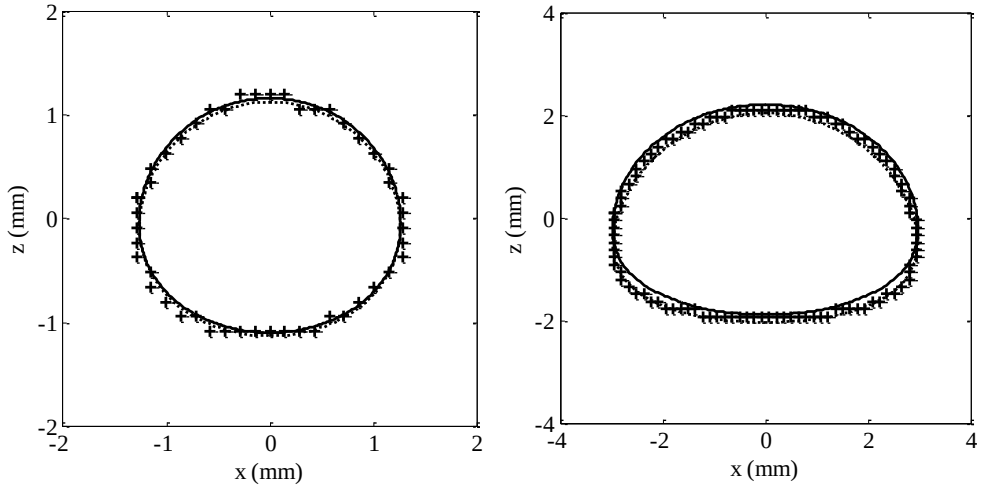

Fig. 3.13 Comparison of the equilibrium drop shapes as observed (+ marker) in our experiments and predicted by Beard and Chuang's (1987) (solid line) model along with the mathematical formulation by Thurai et al., (2007) (dotted line) for (a) 2.6 mm and (b) 5.1 mm drops.

3.4.2 Drop Fall Velocity Evolution

The generated drops accelerated continuously from the source of generation until achieving terminal velocity, U_t. Fig. 3.14 shows the evolution of the fall velocity, U, with fall distance for 2.6, 3.7, and 5.1 mm diameter drops. By the end of Zone I (i.e. at the onset of Zone II), drops achieved 80–90% of U_t. The onset of Zone III was considered when the

drop fall velocity exceeded 99% of U_t as predicted by Eq. (1). Using this criterion, the required fall distances for the onset of Zone III was determined as approximately 8.8, 11, and 12mfor 2.6, 3.7, and 5.1mmdiameter drops, respectively. These fall distances are less than the distances required to achieve 99% of U_t as predicted by Wang and Pruppacher (1977), which are 12, 14, and 13.5 m for 2.6, 3.7, and 5.1 mm diameter drops, respectively. The deviation of the measured and theoretically estimated fall distances for the drops to reach terminal velocity can be attributed to the simplifying assumptions used in the theoretical derivation.

Two of the notable assumptions in the derivation were: (i) absence of source-induced disturbances, and (ii) representation of drag forces for accelerating drops using the drag coefficients that are for drops falling at terminal velocities. Please note that Beard (1977) also noted shorter required fall distances than estimated by Wang and Pruppacher based upon theoretical considerations. The observed average terminal velocities of 2.6, 3.7, and 5.1 mm drops in Zone III were 7.8 m/s, 8.7 m/s and 9.3 m/s. These velocities are in good agreement with the U_t predictions of Eq. (3.1), which are 7.5 m/s, 8.6 m/s, and 9.2 m/s for 2.6, 3.7, and 5.1 mm drops, respectively.

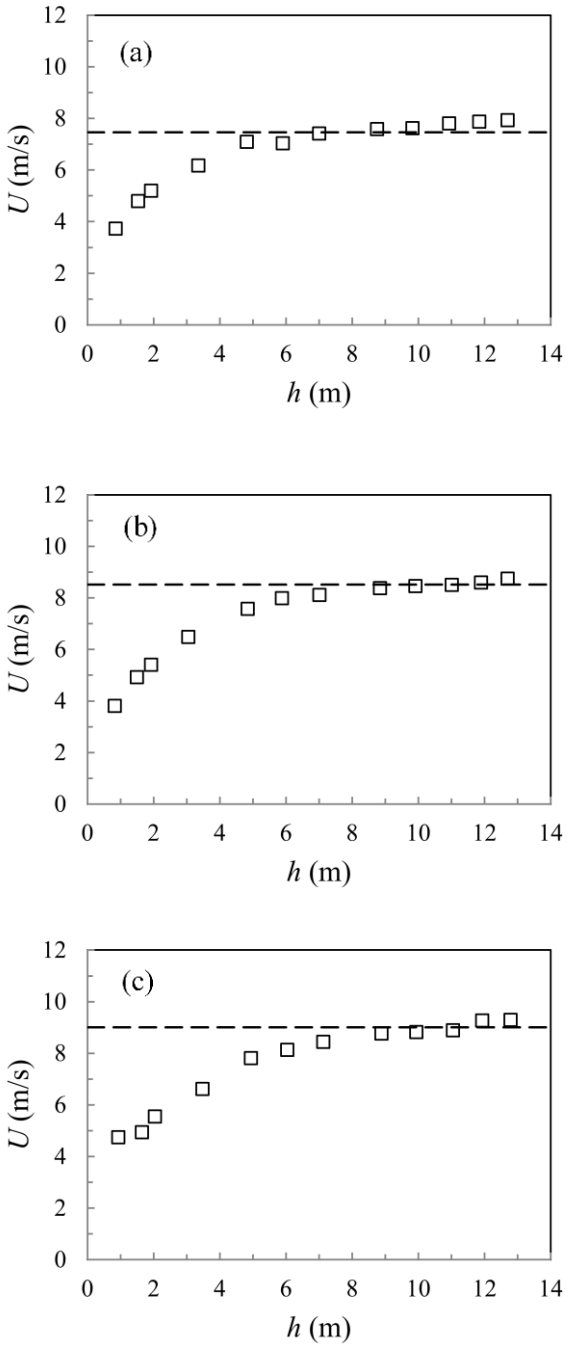

Fig. 3.14 Fall velocity (symbols) evolution of (a) 2.6 mm, (b) 3.7 mm, and (c) 5.1 mm drops with fall distance. Dashed lines indicate 99% of the predicted terminal velocity values by Eq.(3.1).

In Table 3-I, we summarize our findings on shape and fall velocity of free-falling water drops. Our experimental results reveal that terminal velocity is the stringent criterion for free-falling water drops to achieve both the equilibrium shape and the constant fall velocity, i.e. Zone III conditions. For a given application that requires laboratory rainfall simulations under Zone III conditions, rain towers of approximately 12 m would be sufficient to adequately simulate the entire raindrop size spectrum. Though only three raindrop sizes were studied, we can assume some overall conclusions for the entire raindrop size spectrum because Wang and Pruppacher (1977) showed in their theoretical calculations that drops ranging approximately from 2.5 mm to 5 mm in diameter requires the longest fall distances (drops with approximately 3.6 mm diameter requiring the longest fall distance) to achieve terminal velocity in the entire raindrop size spectrum. Please note that this was the reason for studying the selected drop sizes. For some applications (e.g. raindrop shape studies related to radar rainfall estimations), however, equilibrium shaped drops that fall at nonterminal velocities (i.e. Zone II) would be sufficient. In such cases, rain towers of approximately 6 m are adequate for studying the entire raindrop size spectrum. As our experimental observations for Zone II indicate, drops can attain equilibrium shapes before achieving terminal velocities although the velocity and pressure fields are not fully developed. There may be different plausible explanations for this observation. One explanation is that the changes in the velocity and pressure fields may have insignificant effect on the drop shape during this acceleration phase. Another explanation is that the hydrodynamic and the aerodynamic forces may vary in such a way

that the shape remains almost constant. An accurate explanation for this observation requires a comprehensive investigation, which is beyond the scope of this study.

Table 3-I Summary of findings. Zone II and Zone III columns indicate the respective stringent fall distance requirement for the onset of each zone for all raindrop sizes in the natural raindrop size spectrum.

Drop	2.6 mm	3.7 mm	5.1 mm	Zone II (m)	Zone III (m)
Parameter	Distance to achieve equilibrium values (m)				
Axis Ratio	3.4	4.8	6		
Chord Ratio	3.4	4.8	6		
Orientation	3.4	4.8	5		
Shape Comparison	Distance to achieve constant values for the correlation between the experimental and predicted (Beard and Chuang 1987) shapes (m)			6	12
	3.4	4.8	6		
Fall Velocity	Distance to achieve terminal velocity (m)				
	8.8	11	12		

3.5 Conclusion

This laboratory study was conducted to provide guidance in adequate laboratory simulations of natural rainfall and also to elucidate free-falling water drop morpho dynamics. Experiments were conducted for three different drop sizes (2.6, 3.7, and 5.1 mm diameter drops) for fall distances up to approximately 13 m. Digital image processing was implemented to analyze the collected high-speed drop images to determine their shape and fall velocity characteristics. Our observations were compared with and verified the widely-

used theoretical parameterizations for the raindrop shape (Beard and Chuang, 1987) and terminal velocity (Atlas et al., 1973).

Based upon experimental observations, three distinct fall zones were identified (Zone I, Zone II, and Zone III). In Zone I, continuous drop shape adjustment due to source-induced oscillations and gradual viscous damping were the prime features. Zone II is marked by the drops with constant shape, which is referred to as the equilibrium shape, in the absence of drop oscillations. These equilibrium-shaped drops continued accelerating to achieve terminal velocities by the end of this zone. In Zone III, equilibrium-shaped drops fell at terminal velocities. Based upon our experimental observations, the extents of Zone I and Zone II (hence the onset of Zone III) were identified (see Table 3-I). The required fall distances were found to be smaller than the distances discussed in the literature (e.g. Szakall et al., 2010).

3.6 References

Andsager, K., Beard, K. V., & Laird, N. F. (1999). Laboratory measurements of axis ratios for large raindrops. *Journal of the Atmospheric Sciences*, *56*(15), 2673-2683.

Atlas, D., Srivastava, R. C., & Sekhon, R. S. (1973). Doppler radar characteristics of precipitation at vertical incidence. *Reviews of Geophysics*, *11*(1), 1-35.

Beard, K. V., & Chuang, C. (1987). A new model for the equilibrium shape of raindrops. *Journal of the Atmospheric sciences*, *44*(11), 1509-1524.

Beard, K. V., Kubesh, R. J., & Ochs III, H. T. (1991). Laboratory measurements of small raindrop distortion. Part I: Axis ratios and fall behavior. *Journal of the atmospheric sciences*, *48*(5), 698-710.

Beard, K. V., & Kubesh, R. J. (1991). Laboratory measurements of small raindrop distortion. Part 2: Oscillation frequencies and modes. *Journal of the atmospheric sciences*, *48*(20), 2245-2264.

Beard, K. V., Bringi, V. N., & Thurai, M. (2010). A new understanding of raindrop shape. *Atmospheric Research*, *97*(4), 396-415.

Cifelli, R., & Chandrasekar, V. (2010). Dual-Polarization Radar Rainfall Estimation. *Rainfall: State of the Science*, 105-125.

Green, A. W. (1975). An approximation for the shapes of large raindrops. *Journal of Applied Meteorology*, *14*(8), 1578-1583.

Johnson, D. B., & Beard, K. V. (1984). Oscillation energies of colliding raindrops. *Journal of the atmospheric sciences*, *41*(7), 1235-1241.

Kinnell, P. I. A. (2005). Raindrop-impact-induced erosion processes and prediction: a review. *Hydrological processes*, *19*(14), 2815-2844.

Moriasi, D. N., Arnold, J. G., Van Liew, M. W., Bingner, R. L., Harmel, R. D., & Veith, T. L. (2007). Model evaluation guidelines for systematic quantification of accuracy in watershed simulations. *Trans. Asabe*, *50*(3), 885-900.

Müller, S., Szakáll, M., Mitra, S. K., Diehl, K., & Borrmann, S. (2013). Shapes and oscillations of raindrops with reduced surface tensions: Measurements at the Mainz vertical wind tunnel. *Atmospheric Research*, *119*, 38-45.

Pruppacher, H. R., & Beard, K. V. (1970). A wind tunnel investigation of the internal circulation and shape of water drops falling at terminal velocity in air. *Quarterly Journal of the Royal Meteorological Society*, *96*(408), 247-256.

Pruppacher, H. R., & Klett, J. D. (1997). *Microphysics of clouds and precipitation*. Kluwer Acadenic Publishers.

Pruppacher, H. R., & Pitter, R. L. (1971). A semi-empirical determination of the shape of cloud and rain drops. *Journal of the atmospheric sciences*, *28*(1), 86-94.

Rayleigh, L. (1879). On the capillary phenomena of jets. In *Proc. R. Soc. London* (Vol. 29, No. 196-199, pp. 71-97).

Szakáll, M., Mitra, S. K., Diehl, K., & Borrmann, S. (2010). Shapes and oscillations of falling raindrops—A review. *Atmospheric research*, *97*(4), 416-425.

Szakáll, M., Diehl, K., Mitra, S. K., & Borrmann, S. (2009). A wind tunnel study on the shape, oscillation, and internal circulation of large raindrops with sizes between 2.5 and 7.5 mm. *Journal of the Atmospheric Sciences*, *66*(3), 755-765.

Szakáll, M., Kessler, S., Diehl, K., Mitra, S. K., & Borrmann, S. (2014). A wind tunnel study of the effects of collision processes on the shape and oscillation for moderate-size raindrops. *Atmospheric Research*, *142*, 67-78.

Testik, F. Y. (2009). Outcome regimes of binary raindrop collisions. *Atmospheric Research*, *94*(3), 389-399.

Testik, F. Y., & Barros, A. P. (2007). Toward elucidating the microstructure of warm rainfall: A survey. *Reviews of Geophysics*, *45*(2).

Testik, F. Y., Barros, A. P., & Bliven, L. F. (2006). Field observations of multimode raindrop oscillations by high-speed imaging. *Journal of the atmospheric sciences*, *63*(10), 2663-2668.

Testik, F. Y., Barros, A. P., & Bliven, L. F. (2011). Toward a physical characterization of raindrop collision outcome regimes. *Journal of the Atmospheric Sciences*, *68*(5), 1097-1113.

Thurai, M., Huang, G. J., Bringi, V. N., Randeu, W. L., & Schönhuber, M. (2007). Drop shapes, model comparisons, and calculations of polarimetric radar parameters in rain. *Journal of Atmospheric and Oceanic Technology*, *24*(6), 1019-1032.

Tokay, A., & Beard, K. V. (1996). A field study of raindrop oscillations. Part I: Observation of size spectra and evaluation of oscillation causes. *Journal of Applied Meteorology*, *35*(10), 1671-1687.

Wang, P. K., & Pruppacher, H. R. (1977). Acceleration to terminal velocity of cloud and raindrops. *Journal of Applied Meteorology*, *16*(3), 275-280.

CHAPTER 4

A NUMERICAL APPROACH TO ANALYZING EXTREMELY SHALLOW TURBULENT FLOWS

4.1 Introduction

Extremely shallow (referred to as shallow herein) water flow develops when a thin layer of water flows over a rough surface. Shallow flows are generally considered to have depths in the range of 0.04 m to 0.1 m (Ferguson, 2007; Robert, 1990). Major difference between the shallow flow and the normal river flow is the close proximity of the free surface and the channel bottom to each other. As such, the surface roughness height becomes comparable to the flow depth, which influences the erosions and sediment transport processes. An important example of shallow flows is the overland flow in hill slope hydrology.

The prediction of hydraulic characteristics in shallow flows is important to understand flow behavior and sediment transport under such flows. In general, resistance to flow is exerted by the roughness elements present in the flow. Average velocity (V) in free surface flows is related to hydraulic radius (R) and energy gradient (S_f) through Chezy's coefficient (C), friction factor (f), or Manning's roughness coefficient (n) as shown in Eq. (4.1), respectively (Yen, 2002), where g is the gravitational acceleration. The bed shear stress (τ_o) and shear velocity (u_*) are defined by Eq. (4.2). For uniform

flows in a wide channel, energy slope and hydraulic radius are approximated by bed slope (S_o) and flow depth (h), respectively.

$$V = C\sqrt{RS_f} = \sqrt{\frac{8g}{f}}\sqrt{RS_f} = \frac{h^{1/6}}{n}\sqrt{RS_f} \tag{4.1}$$

$$u_* = \sqrt{\frac{\tau_o}{\rho}} = \sqrt{gRS_f} \tag{4.2}$$

The velocity profile in a shallow flow can be approximated by the turbulent boundary layer theory (Charbeneau et al. 2009). The schematic of the velocity distribution in a shallow flow over rough bed is shown in Fig. 4.1 (Charbeneau et al., 2009). The velocity profile over a smooth bed and rough bed can be approximated by Eq. (4.3), where κ (=0.4) is the von Kármán constant, y_o is the elevation measured from the bed plane where the velocity is zero. It can be expressed as $y_o = 0.033k_s$ for rough bed and $y_o = 0.11(\nu/u_*)$ for smooth bed (Ferguson, 2007), where k_s is roughness height and ν is the kinematic viscosity.

$$\frac{u(y)}{u_*} = \frac{1}{\kappa}\ln\left(\frac{y}{y_0}\right) \tag{4.3}$$

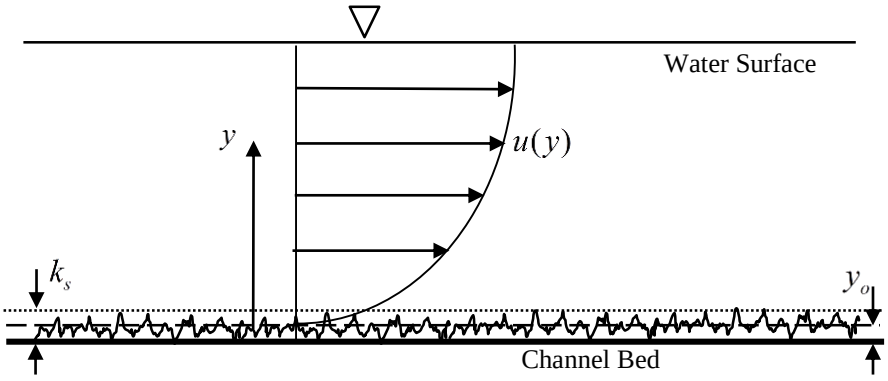

Fig. 4.1 Logarithmic velocity profile in a turbulent boundary layer

Ferguson (2007) reviewed various theoretical velocity profiles models suitable for shallow water flows, including the log-wake profile using both Dean's and Cole's wake components. The logarithmic velocity profile was found to work as well as the other alternatives. However, the assumption of the logarithmic profile for the velocity near the bed region may not be accurate for rough-bed flows, as suggested by Nikora et al. (2004). The study shows that the velocity profile in the interfacial layer (a zone near the bed roughness) may be constant, exponential, or linear, depending upon the flow conditions.

For shallow flows, friction factor can reflect the effects of grain resistance, form resistance, wave resistance, and rain resistance (Hu and Abrahams, 2006; Abrahams et al. 1992; Smith et al. 2007). Grain resistance develops when particles are within 10δ, where δ is the thickness of the viscous sublayer, and form resistance develops when the particles protrudes more than 10δ (Yen, 1965; Abrahams et al. 1992). The existing relationship between the friction factor and the Reynolds number (Re) is applicable where grain roughness dominates. However, a study performed by Abrahams et al. (1992) showed that

95% of the total resistance is due to form resistance for shallow flow in a gravel covered hillslopes. Gilley et al. (1992) presented several equations to estimate friction factor for various land types and land covers. This includes rills, gravel and cobble materials, surface residue, interill areas, plants on cropland areas, and rangeland areas. The study showed the variability of the friction factor to the change in type of surface cover.

Lawrence (1997) analyzed the hydraulics of overland flow using the inundation ratio as the governing parameter, instead of the Reynolds number. The study defined the inundation ratio (h/k_s) using the flow depth (h) and the surface roughness height (k_s). Three regimes were identified based on the inundation ratio: partially, marginally, and well inundated regimes. The study concluded that the Reynolds number is significant in well-inundated regimes, whereas the relative surface coverage, surface slope, and the inundation ratio are the potential influencing factors for partially and marginally inundated regimes. However, the significance of other parameters such as Reynolds number, Froude number, and discharge should also be considered in order to adequately characterize the flow resistance (Smart et al., 2002; Hu and Abrahams, 2006).

Ferro and Baiamonte (1994) presented an experimental study using gravel beds in a rectangular flume. Velocities were measured by a current meter. The study used four different grain shapes and various flow depths to find an accurate representation of the velocity profile. The analysis showed that the velocity profile can mostly be described using logarithmic function or for certain cases a S-shaped profile based on the depth to grain size ratio and bed type. In a similar study, Ferro (2003) measured velocity profiles in a gravel bed of five different arrangements and various flow depths in a horizontal

rectangular flume. An ADV system was used to measure the velocities across the depth. This study also investigated velocity profiles for two different hydraulic conditions (small-scale roughness and large-scale roughness based on the depth to grain size ratio). The results obtained were similar to those of Ferro and Baiamonte (1994).

Nichols (2015) investigated the free surface dynamics in shallow turbulent flows using a Particle Image Velocimetry (PIV) system. The primary objective of the study was to investigate the correlation between the free surface and the turbulent structure in the flow. The study also measured mean velocities across the flow depth for several cases of flow rates, bed slopes, and surface roughness (river gravels with $d_{50} = 4.4$ mm and uniform size polymer spheres of 25 mm diameter). The free surface pattern are correlated to the hydraulic properties of shallow flows.

Shallow free surface flows have been studied widely; however, there is still uncertainty involved in fully understanding the hydraulic behavior of such flows. The primary reason is that measuring flow depths and mean velocities accurately is complicated in such shallow flows (Govers, 1987). In addition, the surface velocity is not an appropriate indes for estimating mean velocity of the flow (Savat, 1980). Further, precision and applicability of Acoustic Doppler Velocimeters (ADV) and electromagnetic current meters are questionable in shallow flows (Smith et al. 2007, Lawless and Robert, 2001; Biron et al., 1998). Numerical simulations may be an effective way to investigate and understand the behavior of shallow flows.

Nicholas (2001) numerically investigated shallow open channel flows over gravel beds considering the water surface as a fixed lid. The non-uniform gravel size was

represented by a random elevation model based on Gaussian distribution, and surface roughness was added to the undular bed topography. The study discussed the advantages and disadvantages of the above approach with the flatbed simulations (where surface roughness (k_s) was used to represent the gravel on the bed) in modeling the turbulent characteristics of the flow. However, the performance of these two approaches in estimating the bed shear stresses and the near bed velocity profiles were not explored. Singh et al. (2007) simulated flow over gravel bed using Direct Numerical Simulation (DNS) and found good correlation between the simulated and the experimental results. Bomminayuni and Stoesser (2011) used Large Eddy Simulation (LES) for flow over closely packed hemisphere to analyze turbulence characteristics and coherent structures of shallow flow at Reynolds number of 13680 and Froude number of 0.17. The study found reasonable agreement with some of the experimental results. However, effect on the bed shear stress was not analyzed and systematically looked at. Furthermore, the model considered water surface as a rigid lid with zero shear stress. Kazemi et al. (2017) simulated shallow water flow with regular spheres using the smooth particle hydrodynamics method. The study conducted 12 sets of experiments of various flow depths and bed slopes on a rough bed ($d = 24$ mm) to investigate the effect of bed roughness under different flow conditions. The study found reasonable correlation between the experimental and numerical results.

Although, many researchers have explored shallow flows over rough surfaces, there is still a need for exploring velocity profiles in various zones across the depth in shallow flows. In addition, there is a need for exploring various bed surface representations and the

corresponding surface roughness estimations in accurately representing velocity and bed shear stresses in shallow flows. The principle objective of this work is to gain insight of the hydraulic characteristics of shallow flows using computational methods. The prediction of bed shear stresses and turbulent velocity profiles are investigated and compared with the available experimental data. The estimation of bed shear stress based on the logarithmic velocity profile and turbulent shear stress are investigated. The bed surface representation by different methods is investigated as well. The methods discussed in this manuscript will enhance the understanding of shallow flows and facilitate future researchers to explore numerically shallow depth water flows under different conditions.

4.2 Numerical Simulation Setup

Simulations were performed using ANSYS Fluent for two-dimensional (2D) shallow flows in a vertical plane solving the Reynolds-Averaged Navier-Stokes (RANS) equations along with a standard $k-\varepsilon$ turbulent closure scheme. For large roughness, the mesh size adjacent to the bed must be selected appropriately. As per Fluent Inc. (2012), the centroid of the cell adjacent to the bed must be higher than the roughness height. Nicholas (2001) found that in cases where the above condition was violated, the near-bed simulated velocities were over-predicted. Generally, the mesh near the bed should be fine enough to capture the large velocity gradient and to model the near-bed velocity accurately. However, larger roughness heights will necessitate relatively larger mesh size that may result in poor predictions of the near-bed velocities. This issue was investigated using a flatbed test case with a roughness height of 0.025 m. Two meshes were used; the first mesh met the above criterion for the first cell adjacent to the bed, while the second mesh was much finer and

the center of the first cell was lower than the roughness height. The results are shown in Fig. 4.2. It is clear that both approaches are valid for predicting velocity profile above the roughness height. Although the velocity profile is predicted below the roughness height, it may not be physically correct. In this study relatively finer meshes were used; however, only the velocity profiles above the roughness height were considered for analysis.

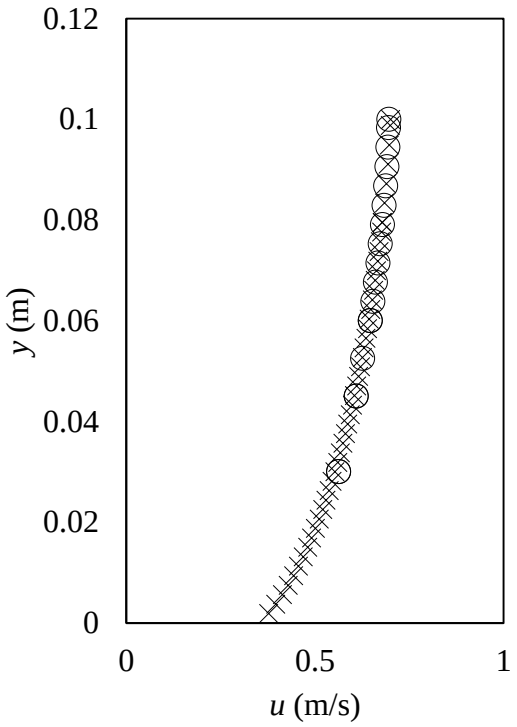

Fig. 4.2: Comparison of simulation results from the flat bed channel. Circular symbol (○) represents the mesh where the first cell centroid is greater than the roughness height. Cross symbol (×) represents results from the finer mesh.

Two different methods were considered to represent a rough bed. The first is a flat-bed layout, where the flow was modelled using conventional wall function with prescribed

roughness height (k_s). In the second option, an undular bed is used. There, the roughness was split into two parts. The grain size is defined as a part of the bed topography, as shown in Fig. 4.3, as semicircles of diameter d_g. The diameter d_g is equal to d_{90} for non-uniform grain sizes. The surface roughness of the undular bed is represented as k_{su} in the standard wall function. A typical near-bed mesh setup produced using an undular bed configuration is shown in Fig. 4.3.

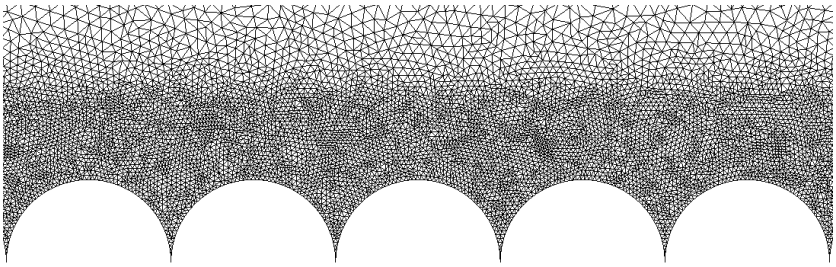

Fig. 4.3: Mesh near the wall for undulating bed configuration.

The free surface was simulated using two-phase model (air and water) using the Volume of Fluid (VOF) method. This approach does not require the knowledge of the uniform flow depth a priori. Thus, only discharge as the boundary condition is sufficient at the inlet, with an arbitrary initial flow depth, given that the flow is allowed to develop and water depths are therefore a result of the numerical simulation. Pressure-velocity field was solved using the SIMPLE scheme. The spatial derivatives were solved using second order upwinding schemes. The domain length was selected as 25 m to ensure that uniform flow conditions are achieved and there is no effect from the downstream boundary into the

domain. The channel bed was modelled as a non-slip wall with standard wall function. The upper boundary was modelled as a slip-boundary with zero shear. The downstream boundary was modelled as a pressure boundary. The results presented here are mesh independent. The maximum relative velocity differences between the grid for which results are presented herein and the finest grid (where the number of elements was increased by 400%) were within 3%.

4.3 Model Validation

In this section, the mean velocity profiles resulting from the simulations for flat and undular beds are compared with the experimental results of Ferro and Baiamonte (1994), Ferro (2003), and Nichols (2015). Mass flow rate, channel slope, and roughness height corresponding to each conditions were calculated from the experimental conditions and are summarized in Table 4-I.

Table 4-I: Various cases and corresponding conditions applied for numerical simulations.

Case	Roughness Height k_s or d_g (mm)	Submergence ratio, h/d_g	Bed Slope, S_o	Experimental Study
1	$d_{90} = 6$	7.50	0.004	Nichols (2015)
2	$d_{90} = 6$	10.83	0.004	Nichols (2015)
3	$d_{90} = 6$	14.33	0.004	Nichols (2015)
4	$d_{90} = 6$	17.67	0.004	Nichols (2015)
5	$d = 25$	2.00	0.004	Nichols (2015)
6	$d = 25$	2.72	0.004	Nichols (2015)
7	$d = 25$	3.52	0.004	Nichols (2015)
8	$d = 25$	4.32	0.004	Nichols (2015)
9	$d_{90} = 29$	6.33	0	Ferro (2003)
10	$d_{90} = 44$	4.89	0.0025	Ferro and Baiamonte (1994)

selection of roughness height (k_s) is important. For river flow over gravel bed, the roughness height is generally taken as 3.1 d_{90} (Bray, 1982); however for shallow flows this approximation may overestimate the effective roughness (Qin and Ng, 2012). One possible reason may be that the shielding effect of the larger particles is predominant in shallow flows. To select an appropriate roughness height, several simulations were conducted for different values of $k_s = \alpha d_{90}$. The results shown in Fig. 4.4 disclose that the velocity profiles shift from right to left as α increases. The optimum value for α was found to be 1.0 $(k_s = d_{90})$. For uniform grain size bed, the use of the grain diameter can adequately represent the experimental velocity profiles (cases 5 – 8).

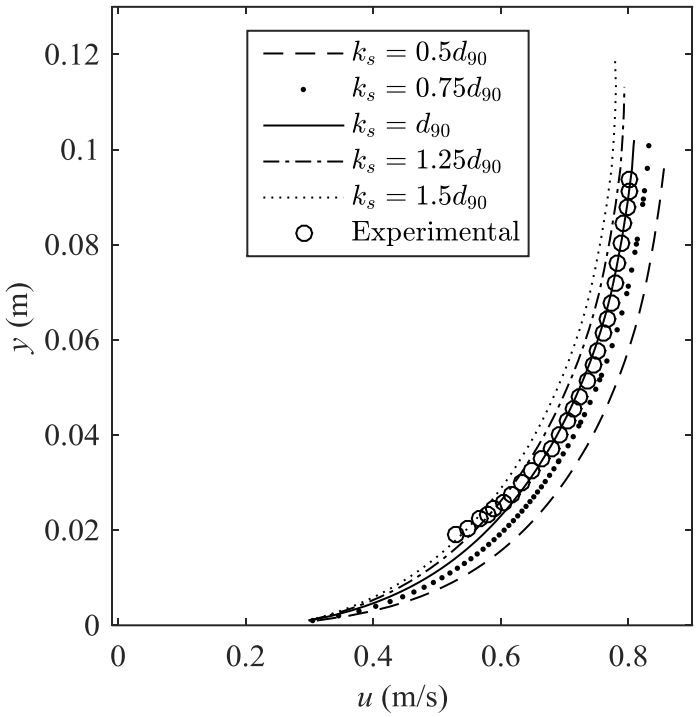

Fig. 4.4: Variation of velocity profiles with roughness height (k_s) over flatbed for case: 4.

In the case of numerical simulations over the undular bed, the diameter of the semicircle (d_g) was selected based on the roughness height used in the flat bed simulations $(d_{90}$ or $d)$. As discussed earlier, this represents the bed topography. The surface roughness (k_{su}) of the bed was determined to achieve the best fit between simulated and the measured velocity profiles. The variation of surface roughness will be discussed in detail later.

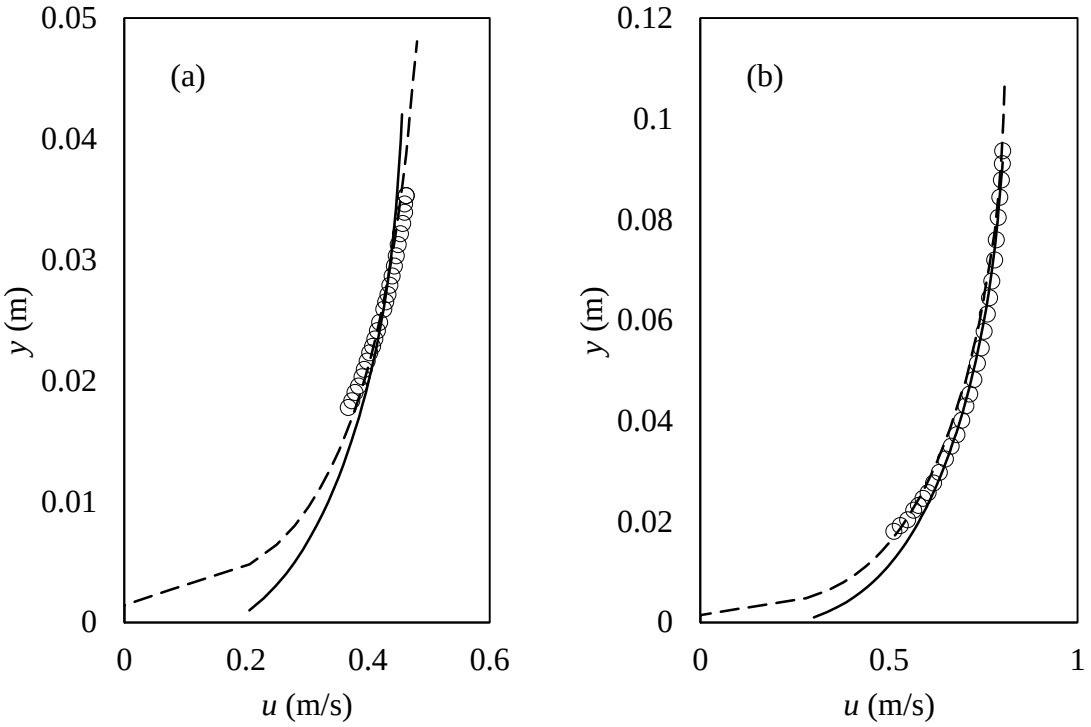

Fig. 4.5: Comparison of the numerical models for the flatbed (−) and undular bed (--) with the experimental (○) results of Nichols (2015) for (a) case 1 and (b) case 4.

Velocity profiles for flat and undular beds configurations are compared with the experimental results in Fig. 4.5–Fig 4.7. The vertical distance for all the velocity profiles was taken from the same datum based on the measured velocity profiles. Few significant observations can be made from the results presented here. The undular bed model performs better than the flat bed model in simulating the velocity profiles. The greatest difference is noted in the near-bed region, and the difference increases as the submergence ratio $\left(h/k_s \text{ or } h/d_g\right)$ decreases. Uniform flow depths resulting from the flatbed and undular bed models are slightly different. The flatbed model over-predicts the velocities in the near-bed region, and consequently under-predicts uniform flow depths. In addition, the velocity

profiles has two distinct regions; the near-bed region is affected by the bed topography and deviates from log-law, while the upper region still follows the log-law.

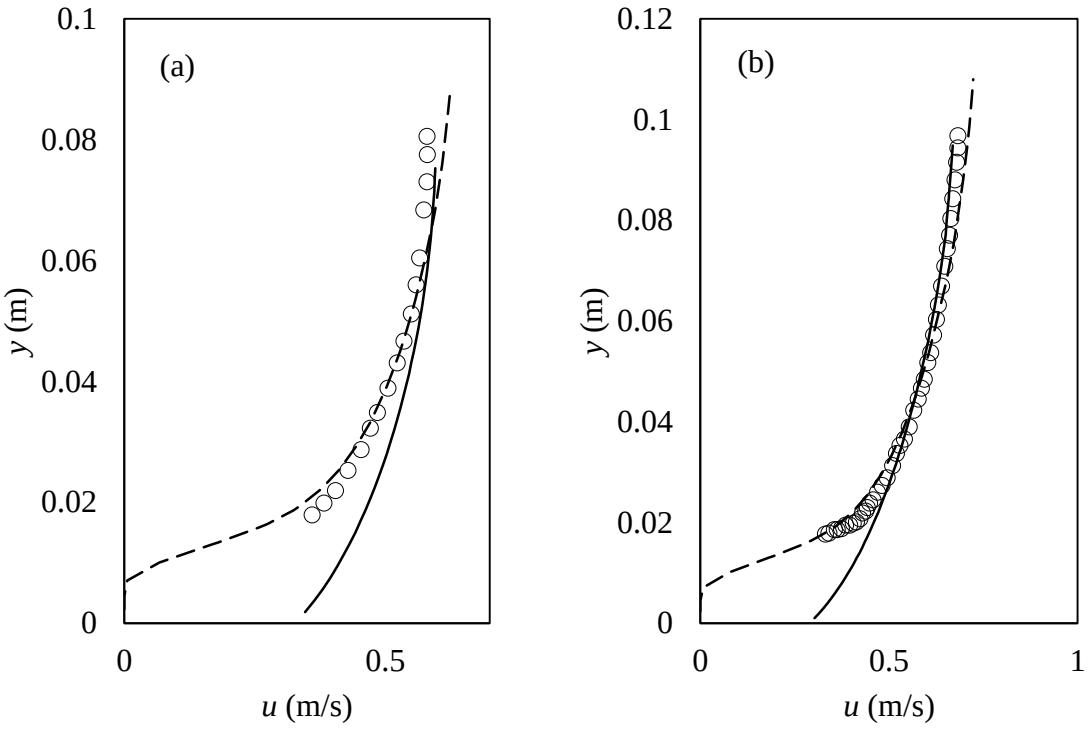

Fig. 4.6: Comparison of the numerical model for both flatbed (−) and undular bed (--) with the experimental (○) results of Nichols (2015) for (a) case 7 and (b) case 8.

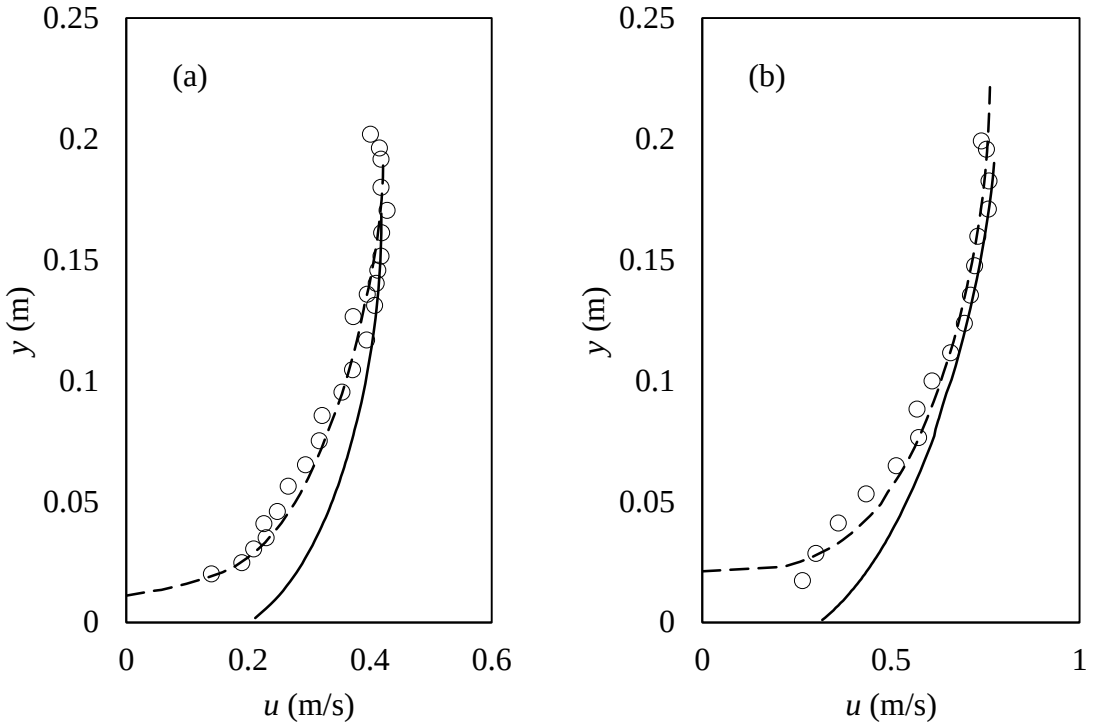

Fig 4.7: Comparison of the numerical model for both flatbed (−) and undular bed (--) with the experimental (○) results for (a) case 9 and (b) case 10.

In open channel flows, the velocity profile in the bottom 20% of the depth can be modeled with logarithmic profile (Nezu and Rodi, 1986). Charbeneau et al. (2009) suggested that the logarithmic region can be extended to the surface for shallow flows. This would imply that the wake component (White, 1991) of the velocity profile might be neglected. Nikora (2004) found experimentally that the velocity profile in the near-bed zone might be exponential, linear, or constant, depending upon the flow condition. The results from the flatbed and undular bed simulations are shown in Fig. 4.8and Fig. 4.9, respectively, along with the fitted log-law. The flatbed simulations show that the velocity profiles are logarithmic throughout the depth. However, as shown previously, the flatbed

model does not predict the measured velocity profiles accurately, especially in the near bed zone. The undular bed simulations show that the near bed zone does not follow log-law as suggested by Nikora (2004). This feature of shallow flows would make bed shear stress prediction difficult, which are generally based on the log-law profile fitted to the bottom 20% of the flow depth.

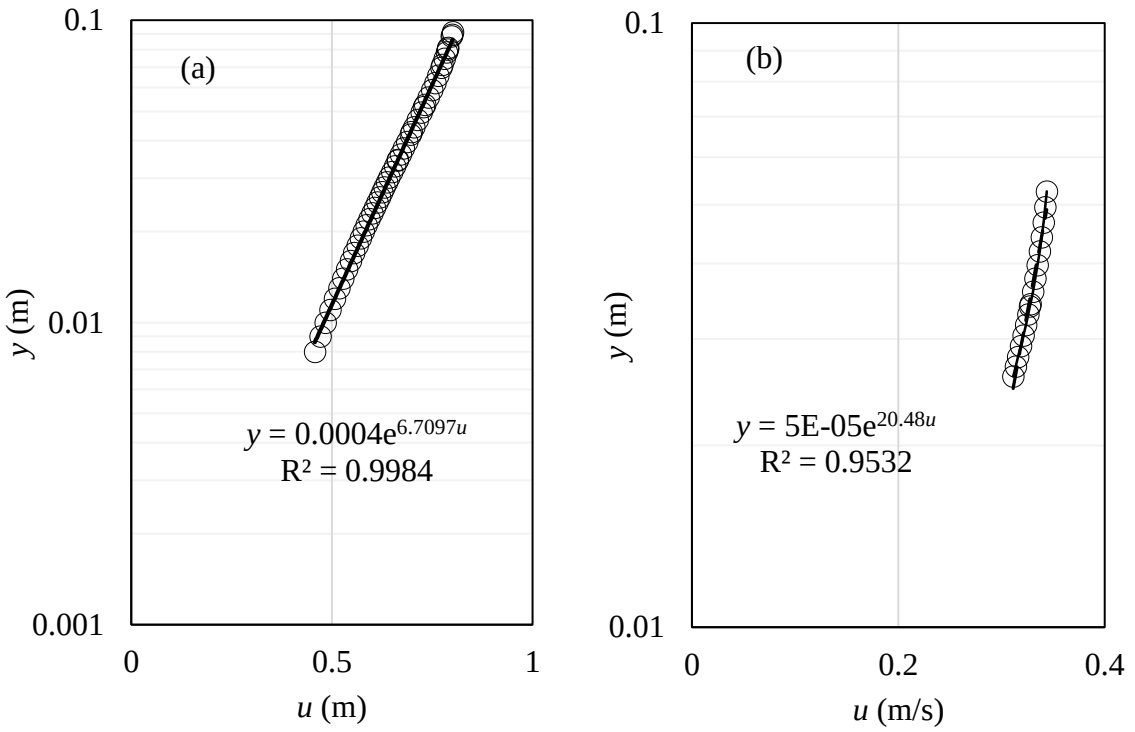

Fig. 4.8: Regions of velocity profile for flatbed simulation for (a) case 4 and (b) case 5. Symbols (○) represents numerical simulation. Solid line (–) represents the log-law fit.

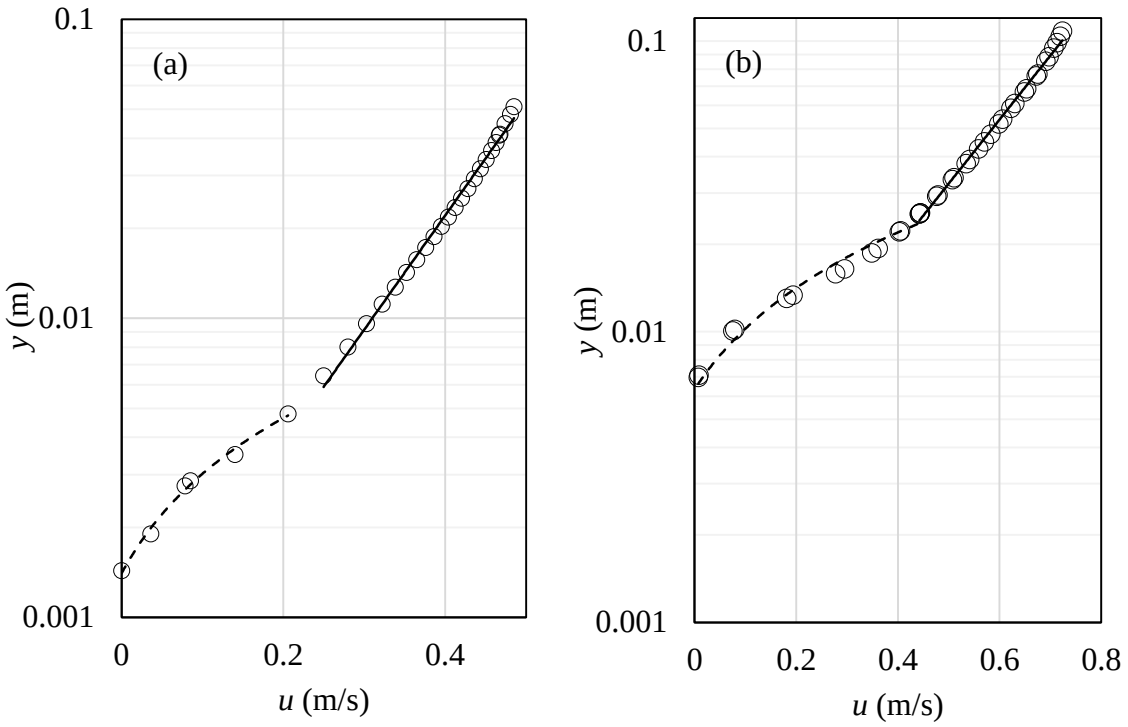

Fig. 4.9: Regions of velocity profile for undular bed simulation for (a) case 1 and (b) case 8. Symbol represents numerical simulation. Solid line (--) represents the log-law fit based on the upper region. Dashed line (--) represents the fit in the near-bed region.

4.4 Analysis of the bed shear stress.

Velocity profiles were analyzed to estimate and compare the bed shear stresses for the flatbed and undular bed configurations. Bed shear stress in an open channel flow can be estimated by either velocity profile, turbulent shear stress profile, or channel bed slope using uniform flow condition (Nezu and Rodi, 1986). In a typical open channel flow, Eq. (4.3) can be used to calculate the bed shear stress from the bottom 20% of the velocity profile. However, the velocity profile for shallow flows consists of two region as discussed earlier. As such, calculating bed shear stress based on the velocity profile may lead to incorrect results.

Non-dimensional turbulent shear stress profiles obtained for undular and flatbed simulations are shown in Fig. 4.10 and Fig. 4.11. Turbulent shear stress changes significantly near the bed (below 0.35*h* for the shallowest case) for undular bed configuration, which is due to the bed topography causing increase in turbulent shear stress. Bed shear stresses for undular beds calculated from the turbulent shear stress profiles (from 0.35*h* to *h*) are found to be the most accurate approach, and is within 5% of the measured bed shear stress values (see Table 4-II). Bed shear stresses for the simulated supercritical flow cases are also consistent with the findings. The flatbed simulations under predicts the bed shear stress based on the turbulent shear stress profiles. The velocity profiles for undular bed start to deviate from the log-law below 0.35*h*. For undular bed configuration, bed shear stresses calculated from the velocity profiles from 0.35*h* to *h* using Eq. (4.3) produce results within 5% of the measured values as shown in Table 4-II. The bed shear stresses calculated from the simulated depths and channel bed slop (for uniform flow conditions) are also listed in Table 4-II. For undular bed, the bed shear stresses based on the uniform flow depths are within 6% of the measured values, while the flatbed configuration under-predicts the bed shear stresses, given that the uniform flow depth is under-predicted.

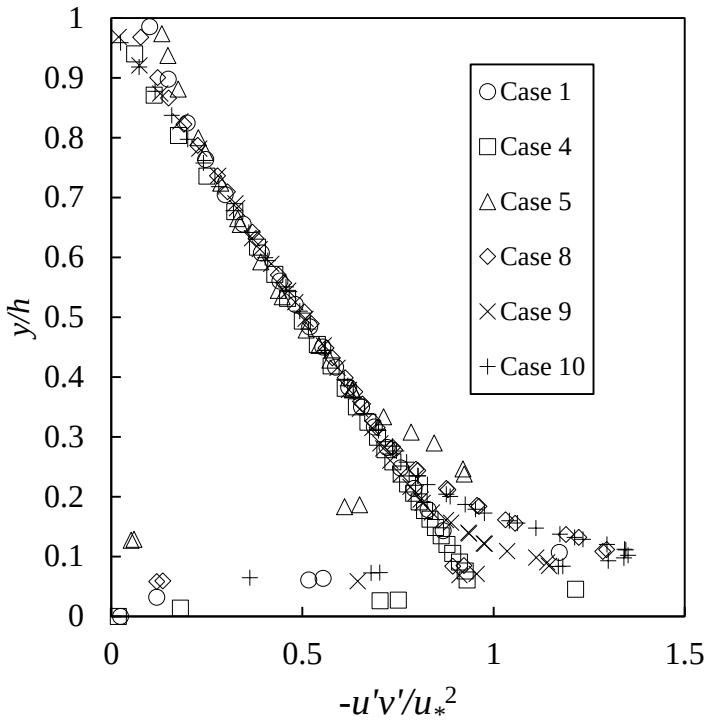

Fig. 4.10: Non-dimensional turbulent shear stress profile for undular bed configurations.

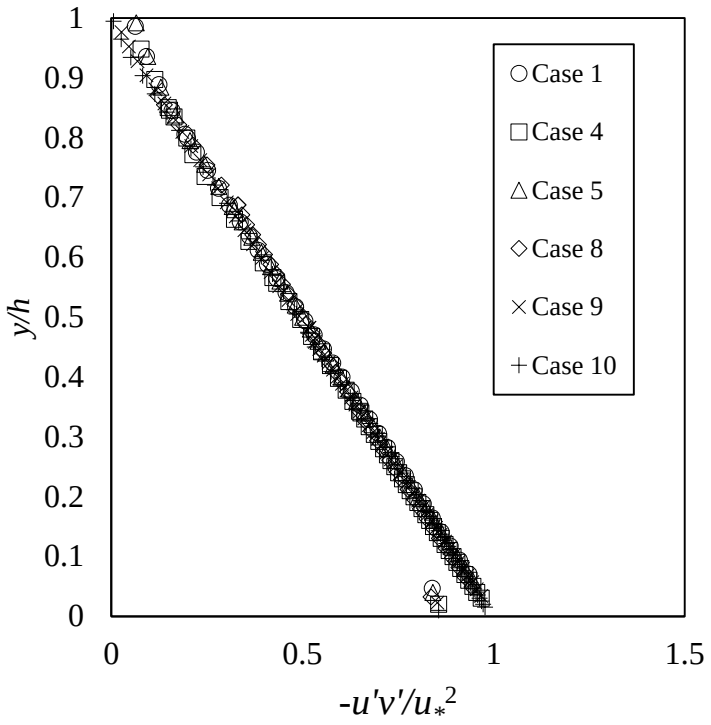

Fig. 4.11: Non-dimensional turbulent shear stress profile for flatbed configurations.

Table 4-II: Comparison of Bed Shear Stresses

Case	Undular bed (from turbulent shear stress), [N/m^2]	Flat Bed (from turbulent shear stress) , [N/m^2]	Undular bed (from velocity profile), [N/m^2]	Bed shear stress from bed slope $\tau_o = \gamma RS_o$, [N/m^2]		
				Undular Bed	Flat Bed	Experiment
1	1.7	1.5	1.53	1.77	1.22	1.77
2	2.4	1.9	2.34	2.55	1.90	2.55
3	3.2	2.4	3.17	3.38	2.02	3.34
4	4.09	3.59	4.24	4.16	3.53	3.92
5	1.85	1.68	1.97	1.96	1.49	1.88
6	2.5	1.99	2.59	2.68	2.16	2.55
7	3.3	2.99	3.32	3.45	2.94	3.34
8	4.24	3.74	4.53	4.24	3.85	4.16
9	1.45	1.21	1.46	-	-	-
10	5.78	3.64	5.53	5.40	4.66	5.47

Turbulent kinetic energy per unit mass (k) in a typical open channel flow increases monotonically below the water surface (Nezu, 1993). The standard $k-\varepsilon$ scheme in a flatbed configuration for shallow flows predicts a similar profile (Fig. 4.12). However, the peak of the turbulent kinetic energy for shallow flows occurs just above the surface of the grains (Nicholas, 2001). Fig. 4.12 also shows the turbulent kinetic profile for shallow flow for undular bed configuration. The monotonic increase below the surface ends around 0.35*h* (similar to velocity and turbulent shear stress profiles). In the near-bed region, the maximum turbulent kinetic energy occurs just above the undulations, similar to that found by Nicholas (2001).

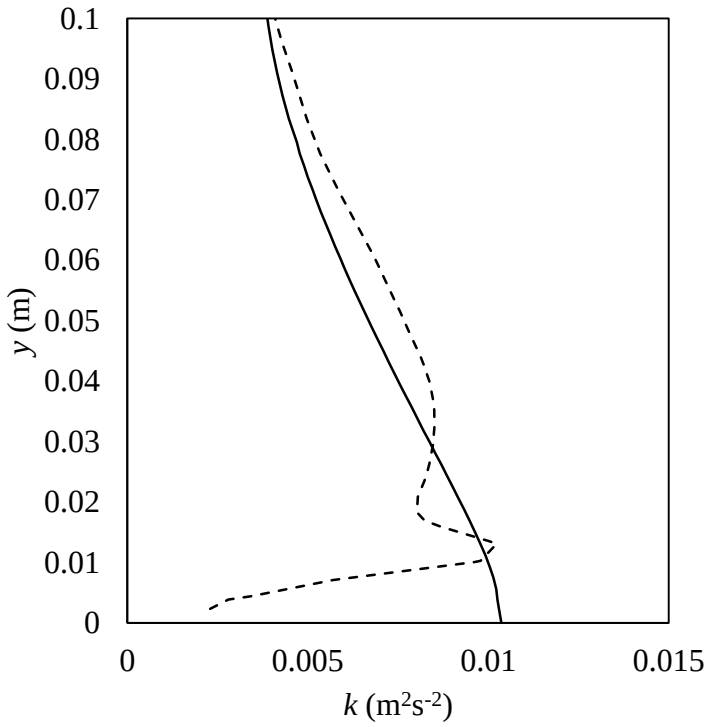

Fig. 4.12: Turbulent kinetic energy per unit mass, *k* profile from flatbed (-) and undular bed (--) simulations.

4.5 Representation of the resistance coefficients and relationship between surface velocities with average velocities.

The resistance coefficients, friction factor (f) and Manning's roughness (n), vary with the flow conditions. In general, the friction factor depends on Reynolds number (Re) of the flow and relative roughness (k_s/h). However, the submergence ratio (h/d_g) is more likely to be dominant (Lawrence, 1997) for shallow flows over a coarse grain bed. In addition to the submergence ratio, the friction factor is found to vary with Froude number (Smart et al., 2002; Hu and Abrahams, 2006). All the cases considered in this study are in the rough turbulent flow regime and friction factor and Manning's roughness coefficient are found to be independent of Reynolds number; however, *f* and *n* are found to vary with the submergence ratio and Froude number for the test cases considered in this study. Froude number and submergence ratio are combined to express the variation of friction factor and Manning's roughness coefficient, as shown in Fig. 4.13.

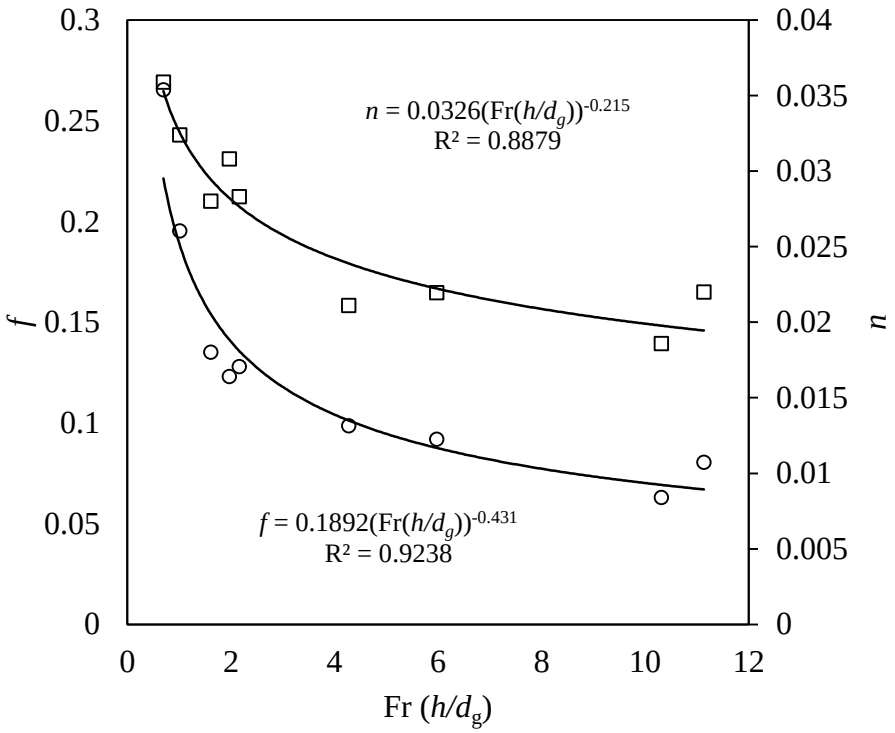

Fig. 4.13: Relation between the resistance coefficients with the submergence ratio and Froude number. Square symbol (□) represents the Manning's roughness, *n* and circular symbol (○) represents the friction factor, *f*. Solid lines represent fitted curve.

Velocity at the water surface is always higher than the mean velocity in an open channel flow. However, in shallow flows, surface velocity is often used as mean velocity due to difficulty in measuring velocity profile accurately. The surface velocity $\left(u_s\right)$ and the average velocity $\left(u_{avg}\right)$ are correlated linearly as shown in the Fig. 4.14 for the cases considered in this manuscript.

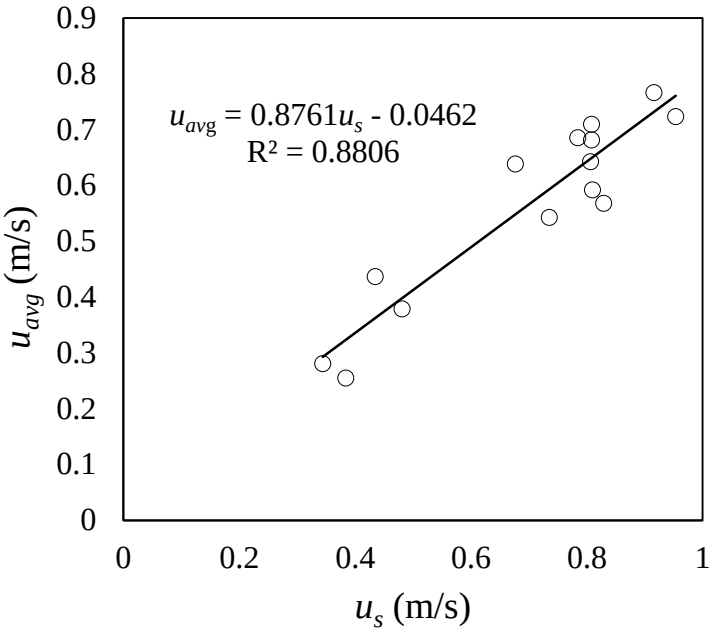

Fig. 4.14: Relationship between the surface velocities with the average velocities.

4.6 Variation of surface roughness for undular bed model

The surface roughness (k_{su}) of the bed topography for undular bed configurations were determined to obtain the best fit between the simulated and experimental velocity profiles for uniform flow depths ranging from 40 mm to 200 mm and grain sizes from 6 mm to 44.1 mm. Fig. 4.15 shows the variation of k_{su}/d_g with depth. The surface roughness of the bed topography varies from $0.03d_g - 0.3d_g$,and increases with the flow depth. Clifford et al. (1992), through theoretical analysis suggested that the surface roughness of the grains can be estimated as $0.4d_{50}$ for flows over gravel bed (equivalent to k_{su}). The surface roughness of the bed topography for undular bed configurations in this study varied from $0.05d_{50} - 0.5d_{50}$ (for shallow to deep flows, respectively), thereby

showing that k_{su} is a function of both grain size and flow depth. For very shallow flows, the form roughness due to bed topography contributes to the most of the total flow resistance (Abrahams et al., 1992). Therefore, the surface roughness of the bed topography for extreme shallow flows is low.

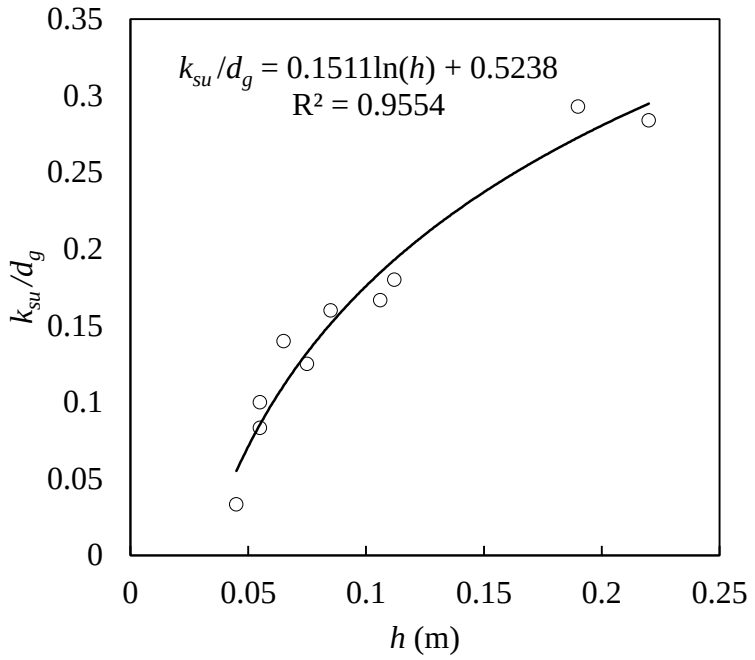

Fig. 4.15: Evolution of non-dimensional surface roughness with the depth. Square symbol (○) represents simulated cases and solid line represents fitted curve.

4.7 Summary and Conclusions

The hydraulics characteristics of the shallow turbulent flows were investigated using numerical simulations. Characteristics such as velocity profile, bed shear stress, resistance coefficients, and surface velocity were analyzed. Two different approaches for

the roughness of the bed (undular bed and flatbed configurations) were compared for simulating shallows flows over coarse grain bed. The grains sizes are represented as the bed topography for the undular bed model with surface roughness imposed on it. For the flatbed configuration, the roughness height represents the influence of both the grain size and the grain surface roughness. Numerical results for both appoaches were validated with the experimental data for various flow depth (40mm-200mm) and grain sizes. The results shows that representation of the grain size as bed topography is essential for simulating shallow flows accurately. The near bed zone that results from the bed topography influences the velocity profile, bed shear stress, and turbulent characteristics. The velocity profile in the near bed zone is linear, but it follows log-law above it. The velocity profiles from the flatbed configuration follow the log-law throughout the depth and significantly over-predicts the velocity in the near bed zone. Consequently, under predicts the uniform flow depth.

Two distinct flow regimes (near bed region and upper region) are identified based on the velocity, turbulent shear stress, and turbulent kinetic energy profiles from the undular bed configuration. The extent of the near bed region was found to be as high as $0.35h$ for the shallowest flow, and it decreases as the submergence ratio increases. Turbulent shear stress profiles provide more accurate technique to estimate the bed shear stresses as compare to log-law profile fitting and slope-based indirect estimations. Friction factor and Manning's roughness can be estimated for shallow flows based on the submergence ratio and Froude number. Analysis shows that the surface roughness of the bed topography for undular bed configuration depends on the grain size and the flow depth.

4.8 References

Abrahams, A. D., Parsons, A. J., & Hirsch, P. J. (1992). Field and laboratory studies of resistance to interrill overland flow on semi-arid hillslopes, southern Arizona. *Overland flow: Hydraulics and erosion mechanics*, 1-23.

Biron, P. M., Lane, S. N., Roy, A. G., Bradbrook, K. F., & Richards, K. S. (1998). Sensitivity of bed shear stress estimated from vertical velocity profiles: The problem of sampling resolution. *Earth Surface Processes and Landforms*, *23*(2), 133-139.

Bomminayuni, S., & Stoesser, T. (2011). Turbulence statistics in an open-channel flow over a rough bed. *Journal of Hydraulic Engineering*, *137*(11), 1347-1358.

Bray, D. I. (1982). Flow resistance in gravel-bed rivers. In *Grave-bed rivers, Fluvial Processes, Engineering and Management*, ed. R. D. Hey, J. C. Bathurst, and C.R. Thorne. New York: Wiley, 1982, pp. 109-37.

Charbeneau, R. J., Jeong, J., & Barrett, M. E. (2009). Physical modeling of sheet flow on rough impervious surfaces. *Journal of Hydraulic Engineering*, *135*(6), 487-494.

Clifford, N. J., Robert, A., & Richards, K. S. (1992). Estimation of flow resistance in gravel-bedded rivers: A physical explanation of the multiplier of roughness length. *Earth Surface Processes and Landforms*, *17*(2), 111-126.

Ferguson, R. (2007). Flow resistance equations for gravel-and boulder-bed streams. *Water Resources Research*, *43*(5).

Ferro, V., & Baiamonte, G. (1994). Flow velocity profiles in gravel-bed rivers. *Journal of Hydraulic Engineering*, *120*(1), 60-80.

Ferro, V. (2003). ADV measurements of velocity distributions in a gravel-bed flume. *Earth Surface Processes and Landforms*, *28*(7), 707-722.

Fluent, (2011). Ansys Fluent Theory Guide. *ANSYS Inc., USA*.

Gilley, J. E., Kottwitz, E. R., & Wieman, G. A. (1992). Darcy-Weisbach roughness coefficients for gravel and cobble surfaces. *Journal of irrigation and drainage engineering*, *118*(1), 104-112.

Govers, G. (1987). Initiation of motion in overland flow. *Sedimentology*, *34*(6), 1157-1164.

Hu, S., & Abrahams, A. D. (2006). Partitioning resistance to overland flow on rough mobile beds. *Earth Surface Processes and Landforms*, *31*(10), 1280-1291.

Kazemi, E., Nichols, A., Tait, S., & Shao, S. (2017). SPH modelling of depth-limited turbulent open channel flows over rough boundaries. *International Journal for Numerical Methods in Fluids*, 83(1), 3-27.

Lawless, M., & Robert, A. (2001). Scales of boundary resistance in coarse-grained channels: turbulent velocity profiles and implications. *Geomorphology*, *39*(3), 221-238.

Lawrence, D. S. L. (1997). Macroscale surface roughness and frictional resistance in overland flow. *Earth Surface Processes and Landforms*, *22*(4), 365-382.

Nezu, I., & Rodi, W. (1986). Open-channel flow measurements with a laser Doppler anemometer. *Journal of Hydraulic Engineering*, *112*(5), 335-355.

Nezu, I. (1993). Turbulence in open-channel flows. IAHR-Monograph, Balkema.

Nicholas, A. P. (2001). Computational fluid dynamics modelling of boundary roughness in gravel-bed rivers: an investigation of the effects of random variability in bed elevation. *Earth Surface Processes and Landforms*, *26*(4), 345-362.

Nichols, A. (2015). *Free surface dynamics in shallow turbulent flows* (Doctoral dissertation, University of Bradford).

Nikora, V., Koll, K., McEwan, I., McLean, S., & Dittrich, A. (2004). Velocity distribution in the roughness layer of rough-bed flows. *Journal of Hydraulic Engineering*, *130*(10), 1036-1042.

Qin, J., & Ng, S. L. (2012). Estimation of effective roughness for water-worked gravel surfaces. *Journal of Hydraulic Engineering*, *138*(11), 923-934.

Robert, A. (1990). Boundary roughness in coarse-grained channels. *Progress in physical geography*, *14*(1), 42-70.

Savat, J. (1980). Resistance to flow in rough supercritical sheet flow. *Earth surface processes*, *5*(2), 103-122.

Singh, K. M., Sandham, N. D., & Williams, J. J. R. (2007). Numerical simulation of flow over a rough bed. *Journal of Hydraulic Engineering*, *133*(4), 386-398.

Smart, G. M., Duncan, M. J., & Walsh, J. M. (2002). Relatively rough flow resistance equations. *Journal of Hydraulic Engineering*, *128*(6), 568-578.

Smith, M. W., Cox, N. J., & Bracken, L. J. (2007). Applying flow resistance equations to overland flows. *Progress in Physical Geography*, *31*(4), 363-387.

White, F.M. (1991). Viscous Fluid Flow. McGraw-Hill, New York.

Yen, B. C. (1965). Discussion of "Large-scale roughness in open channel flow". *Journal of the Hydraulics Division, Proceedings of the American Society of Civil Engineers 91*, 257-62.

Yen, B. C. (2002). Open channel flow resistance. *Journal of hydraulic engineering*, *128*(1), 20-39.

CHAPTER 5

CONCLUSIONS

5.1 Summary of the research

This research focuses on different flow phenomena related to the shallow depth water flow with three distinct objectives. The first objective is to investigate numerically the properties of circular turbulent jets in shallow water in three dimensional (3-D) domain, essential to the knowledge of mixing and dilution of industrial and municipal discharges. The second objective is to provide guidelines for natural rainfall simulations in laboratory using sequential images of falling water drops, essential to correlate raindrop impact induced sediment transport in shallow water flow. The final objective is to numerically investigate the shallow depth water flow using two bed configurations (flatbed and undular bed) in two dimensional (2-D) domain. Simulations were performed using the commercial computational fluid dynamics software ANSYS Fluent. Specific conclusion from each study are summarized below.

In the first phase of this research, effect of confinement on the dilution/entrainment and mixing properties of circular turbulent jets in shallow water flow were numerically investigated. The results reveal that the confinement has profound impact on the mixing and dilution characteristics of a jet in shallow water. Moreover, mixing/growth properties of a jet is greatly influenced by the confinement. Usually, mixing in the horizontal plane of a confined jet is less than that of a free jet. In the vertical plane, mixing characteristics in the upper portion differ significantly from the lower portion of the jet. Mixing is

enhanced (velocity profiles become more uniform) in the upper portion for symmetric and water surface confinement cases. However, for bed confinement cases the mixing is low in the upper portion of the jet. Mixing in the lower portion of the vertical plane is enhanced for all the cases of confinements. The results show that the pollutant may concentrate near the bed or surface depending on the submergence/offset ratio, which may have profound impact on the ecological system.

The second phase of the research experimentally investigated evolution of water drops generated for laboratory rainfall simulation. Based upon experimental observations, three distinct fall zones were identified (Zone I, Zone II, and Zone III). In Zone I, continuous drop shape adjustment due to source-induced oscillations and gradual viscous damping were the prime features. Zone II is marked by the drops with constant shape, which is referred to as the equilibrium shape, in the absence of drop oscillations. These equilibrium-shaped drops continued accelerating to achieve terminal velocities by the end of this zone. In Zone III, equilibrium-shaped drops fell at terminal velocities. Based upon the experimental observations, the extents of Zone I and Zone II (hence the onset of Zone III) were identified. The required fall distances were found to be smaller than the distances prescribed in the existing literatures.

The final phase of the research focuses on to characterize the shallow flows over coarse grain surfaces through numerical simulations. The results show that representation of the grain size as bed topography is essential for simulating shallow flows accurately. The near bed zone that results from the bed topography influences the velocity profile, bed shear stress, and turbulent characteristics. The velocity profile in the near bed zone is linear,

but it follows log-law above the near bed zone. The velocity profiles from the flatbed configuration follow the log-law throughout the depth and significantly over-predicts the velocity in the near bed zone. Consequently, under predicts the uniform flow depth. The resistance coefficients can be predicted based on the submergence ratio and Froude number.

5.2 Future Research Scopes

Results and finding from this study can lead to a number of scopes for future research. Surface roughness effects on the attachment characteristics of the turbulent jets in shallow flows can be explored. In addition, buoyancy effects on the mixing and dilution of turbulent jets in shallow water can be investigated. Sediment detachment from the soil surface due to rain drop impact can be investigated through the optimum laboratory experiment setup proposed here. Furthermore, the combined effect of raindrop and shallow flows on sediment transport during a rainfall event can be explored and characterized experimentally and numerically. Effect may include modified bed shear stress, velocity profile, and resistance characteristics.